Development of materials and device architectures aimed for high-performance continuous-wave organic semiconductor lasers

アディカリ，ムディヤンサラゲ，チャトゥランガニ，セネヴィラトゥネ

2021

Doctoral thesis

Development of materials and device architectures aimed for high-performance continuous-wave organic semiconductor lasers

Adikari Mudiyanselage Chathuranganie Senevirathne

Department of Applied Chemistry

Graduate School of Engineering

Kyushu University

Table of Contents

Chapter 1

Introduction

1.1 Laser

LASER is an acronym for *L*ight *A*mplification of *S*timulated *E*mission of *R*adiation. As the name implies, laser devices operate on the process called stimulated emission of light, which was first postulated in 1917 by Einstein[1]. Hence, laser light acquires special features like coherent, monochromatic emission, low divergence, high directionality, and power compared to normal light. Because of these promising features, lasers are used in ubiquitous applications in our daily life, such as in scanners, printers, sensors, and so on.

Basically, a laser is a light oscillator and it consists of three main components to continue the oscillation process[2]. First, it requires a pumping source to fill up the excited states continuously in the laser medium. This can be either optical pumping or electrical injection. Second, it needs a gain which facilitates population inversion. Third, it requires a resonator to provide the feedback for light amplification to continue the lasing process. Figure 1.1 shows the basic components of a laser device which are discussed in detail above.

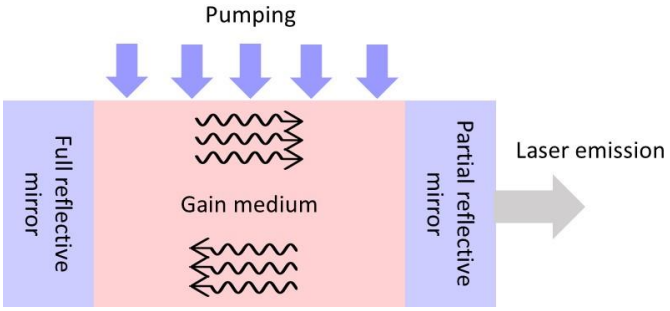

Figure 1.1. Basic components of a laser.

When looking back the history of lasers, in 1954, first maser (microwave amplification of stimulated emission of radiation) was invented by Townes[2,3]. In 1959, Gould gave the acronym LASER[4] and a year later in 1960, the first laser, which emits in the visible range of the electromagnetic spectrum, was realized by Maiman with a ruby crystal with silver-coated ends to make it as a Fabry-Perot resonator[5].

1.2 Basic methods for laser operation and their applications

Basically, there are two main methods to operate a laser.

1. Continuous-wave (CW) operation
2. Pulsed-wave operation

Output laser mechanisms and output powers are different in these two laser operation methods, which can be used specifically for particular applications according to the specific needs.

1.2.1 Continuous-wave (CW) operation

In these lasers, laser output is uninterrupted. That is, a continuous laser beam can be obtained. Output laser power is also stable with time, as shown in Figure 1.2. If a particular application requires a constant average power for a certain period of time, the ideal candidate is a CW laser[6, 7]. If the output power is stable for a time duration of μs or longer, the laser operation is called as the quasi-continuous-wave (qCW) lasers where the operation time is short enough to suppress heating but still long enough to acquire a real steady state. As a result, these lasers operate with high peak power and lower average power. CO_2 lasers, HeNe lasers, titanium sapphire (TiS) lasers, neodymium yttrium aluminum garnet (Nd:YAG) lasers are a few examples of CW lasers[2]. These lasers are used in optical tweezers, laser cutting and welding, biomedical imaging such as in stimulated emission depletion (STED) microscopy, semiconductor inspection for defects, cytometry, and velocimetry [8].

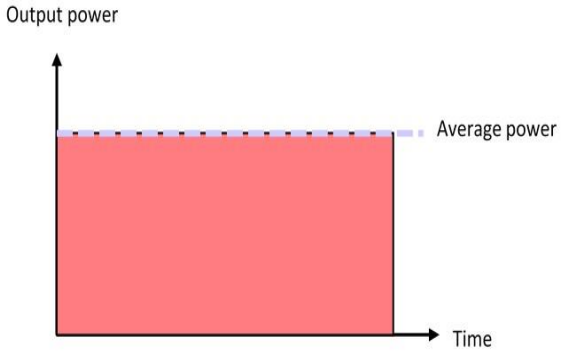

Figure 1.2. Output power vs. time graph of CW lasers.

1.2.2 Pulsed-wave operation.

As the name suggests, an output beam is a short burst of laser radiation emitted under constant time intervals. An emitted output laser beam acquires a high peak power, as shown in Figure 1.3 and the pulse duration lies in fs to ns scale. Pulsed lasers store energy and release it very rapidly. They are used in time-resolved scientific applications such as spectroscopy and manufacturing processes, which need non-thermal material modification such as laser ablation, fabrication of porous structures, light detection and ranging (LiDAR) applications, and medical surgeries. The pulsing is achieved in lasers using Q-switching, cavity dumping, and mode-locking techniques. Frequency-doubled and Q-switched Nd:YAG laser, nitrogen laser, and excimer laser are a few examples of pulsed lasers[6, 7].

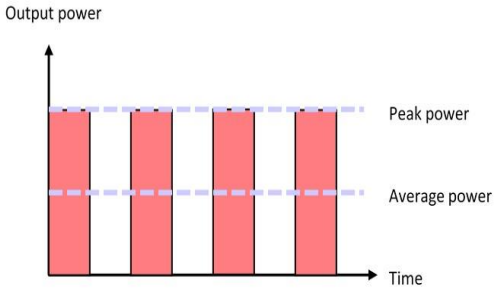

Figure 1.3. Output power vs. time graph of pulsed lasers.

1.3 Organic semiconductor lasers

1.3.1 Background

Organic semiconductors have drawn the attention as a promising laser material in the early stage of laser invention. In 1961, Brock et al. [9] and Rautian and Sobel'man[10] independently suggested using conjugated organic molecules for lasing. This led Sorokin and Lankard to realize the first organic solution-based dye lasers using chloro-aluminum phthalocyanine in ethanol, which was pumped by a giant pulse ruby laser in 1966[11]. In 1967, Sofer and McFarland invented the first solid-state dye laser using a dye-doped polymer matrix[12]. Years later, the quest to find efficient organic laser materials was accelerated after

realizing organic light-emitting diodes (OLEDs) with evaporated organic small molecular thin films by Tan and Slyke in 1987[13]. As a result, Hide et al. reported the first solid-state polymer laser in 1996[14]. In the same year, Tessler et al. reported a neat film of conjugated polymer laser incorporated in a microcavity resonator[15]. Today, a myriad of organic laser materials has been reported, with excellent laser properties[16]. Recently, the most awaited first organic semiconductor laser diodes (OSLDs) were realized by Sandanayaka et al. in Adachi lab of Kyushu University[17]. This work opened up a new direction toward organic laser research focusing on more stable electrical lasing from organic semiconductors for future applications. Figure 1.4 shows the evolution of organic semiconductor lasers reported to date.

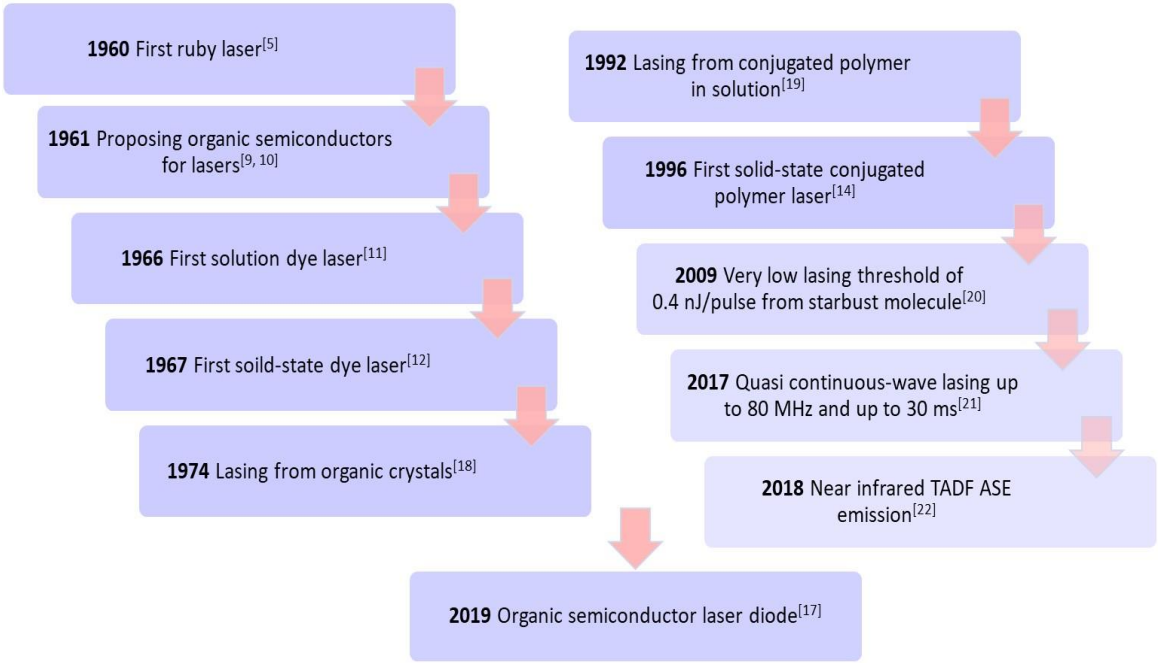

Figure 1.4. Milestones of organic semiconductor lasers.

1.3.2 Organic semiconductors

Out of many organic materials, conjugated organic molecules possess the semiconducting properties via their sp^2 hybridization which facilitates the delocalization of

π electrons along the chain. These electrons are loosely bounded and able to absorb near-UV to visible light enabling π-π* transitions[23].

In lasers, achieving population inversion is crucial for lasing. However, according to thermal equilibrium, levels of population in two energy systems acquire Boltzmann distribution, resulting in a much higher population in the ground state than the excited state. The excited-state molecules depopulate via both radiative (spontaneous emission) and non-radiative transitions and it is challenging to achieve a non-equilibrium state in two energy levels. To achieve population inversion in a laser, a three-level or four-level energy system should be introduced. In this regard, conjugated organic molecules are ideal as they introduce vibrational energy states in addition to their electronic energy states, enabling a four-level energy system for population inversion[24]. Figure 1.5 shows the Jablonski energy diagram of a typical organic semiconductor, facilitating the four-level energy system for the population inversion.

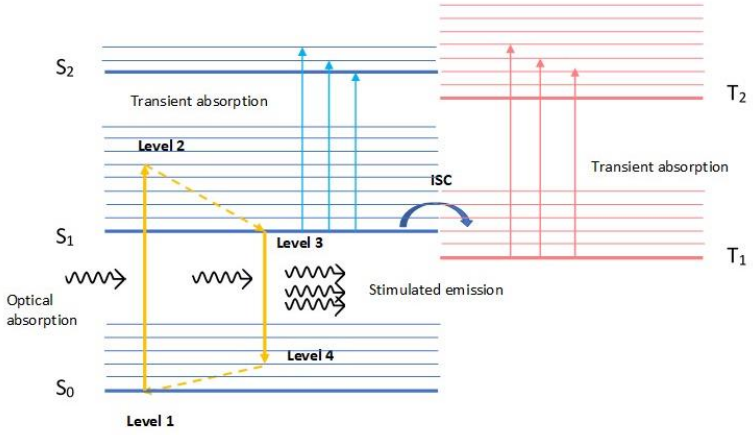

Figure 1.5. Jablonski diagram of a typical organic semiconductor material. The formation of a four-level energy system is required for lasing.

In an organic semiconductor material, first light can excite the molecules from the ground state to some singlet excited state (*level 2*) to form singlet excitons, and eventually, these excitons quickly relax back to the bottom of the singlet excited state (*level 3*), resulting in a population inversion between the singlet excited state (*level 3*) and the vibrationally excited ground state (*level 4*). Then, lasing takes place via the transition from level 3 to 4,

followed by a vibrational relaxation back to the ground state. Moreover, this introduces a Stokes' shift between absorption and emission spectra as energy loss due to vibrational relaxation, which is beneficial for lasing in organic semiconductors which prevents self-absorption in laser materials[16].

Most of the reported organic semiconductor materials fall into the classes of small molecules, conjugated polymers, conjugated dendrimers, and spiro-compounds[23]. However, small molecules (< 1000 Da) have well-defined structures with high purity, preventing their batch-to-batch variation of photophysical properties like in conjugated polymers. On the other hand, they can also be easily synthesized compared to conjugated dendrimers which proceed series of steps to the end product. Another advantage of using small molecules is that they can be vacuum-deposited and even solution-processed by introducing solubilizing side groups.

In addition, organic semiconductors possess strong absorption of light, high optical gain, and broad fluorescence, enabling fine-tuning the emission from the near-ultraviolet to visible and infrared regions[23-25]. However, in condensed states, these molecules tend to interact with their neighbors, resulting in the formation of the aggregates. This will eventually quench the emission from these materials. This behavior is more common in neat solid-state films and can be suppressed by increasing a distance between neighboring organic molecules by blending them in a host matrix. The facile processing of these materials also opens up a variety of optical resonator structures, which can inscribe directly into the organic gain mediums in laser studies[23].

1.3.3 Gain of organic semiconductors

The gain of a laser medium is a crucial factor for lasing. It gives an idea about both amplification and the depopulation routes of the excited states to figure out if a particular laser material has a window for laser amplification. This can be experimentally determined by investigating amplified spontaneous emission (ASE) or transient absorption (TA) of a given material[23, 25]. Out of these two methods, ASE measurement is the simplest way of

determining the gain of a laser material, although TA provides more clearer picture about the excited states with singlet and triplet absorptions.

Gain coefficient of a laser material (g) is given by the product of stimulated emission cross-section (σ_{em}) and population inversion density N as given in equation 1.1[26]

$$g = \sigma_{em} N \qquad (1.1)$$

The stimulated emission cross-section, σ_{em} is expressed as [27, 28],

$$\sigma_{em} = \frac{h\nu n(\nu) B E_f(\nu)}{c\phi_f} = \frac{\lambda^4 E_f(\lambda)}{8\pi n^2(\lambda) c \tau_f} \qquad (1.2)$$

where h is the Plank's constant, ν is the frequency of light, $n(\nu)$ is the refractive index of the active gain medium, B is Einstein B coefficient, $E_f(\lambda)$ is the distribution of fluorescence quantum yield given by $n_f = \int E_f(\lambda) d\lambda$, c is the velocity of light, ϕ_f is the "fluorescence" quantum yield, λ is the emission wavelength, and τ_f is the transient lifetime. If a laser material has a positive gain at a particular wavelength, absorption cross-section (σ_{ABS}), excited-state absorption of singlets (σ_S) and triplets (σ_T) should be smaller than the $\sigma_{em.}$ That means effective stimulated emission cross-section $\sigma_{effem} > 0$.

$$\sigma_{effem} = \sigma_{em} - (\sigma_{ABS} + \sigma_S + \sigma_T) \qquad (1.3)$$

1.3.3.1 Amplified spontaneous emission (ASE)

The ASE is obtained in a slab waveguide structure in which an organic layer is sandwiched between two low-refractive-index layers for efficient confinement of light. Normally, organic materials have a higher refractive index ~2.0. Therefore, cladding materials would be low-refractive-index materials such as glass (n=1.46) and air (n=1.0), resulting in an asymmetric slab waveguide. Moreover, high-quality organic films should be implemented in ASE measurement to eliminate undesirable scattering from the roughness of organic films. Confining a single mode in the waveguide via optimized film thickness is also crucial in ASE measurement, if else, the low film thickness will result in less confinement of the guided mode and higher film thickness will result in mode competition which both will eventually lead to higher ASE threshold[26].

In ASE measurement, pulse photoexcitation in a rectangular stripe is used to excite the gain medium. Light emitted by the material is waveguided along the length of the excitation stripe. This waveguided spontaneous emission can result in stimulated emission, which is a result of amplification before being emitted from the edge of the film sample and leads to a spectrally narrow emission. Wavelength-dependent output intensity $I(\lambda)$ of the ASE is given by

$$I(\lambda) = \frac{A(\lambda)Ip}{g\prime(\lambda)}[\exp(g(\lambda)l) - 1], \qquad (1.4)$$

where $A(\lambda)$ is a constant related to emission cross-section, I_p is pumping intensity, l is the length of the stripe, and g is the net gain coefficient [23, 26]. The net gain is the difference between the gain and the loss. Because the optical gain is reduced by several loss channels quantified by loss coefficient (α). Then net gain is[26]

$$g' = g - \alpha = \sigma_{em}N - \alpha, \qquad (1.5)$$

Threshold condition is reached when the loss is compensated by gain where g' = 0 (i.e., g = α). Therefore, the ASE threshold (E_{th}) is given by[29],

$$E_{th} = \frac{\alpha h\nu d}{\Gamma L\, \sigma_{em}\, \phi_f} \qquad (1.6)$$

where d is the thickness, Γ is the confinement factor, and L is the stripe length. However, Einstein B coefficient is proportional to radiative decay constant (k_r) as equation 1.7 and it also inversely proportional to ASE E_{th} as in equation 1.8[27]

$$B \propto \left(\frac{c^3}{8\pi h\nu^3}\right) k_r \qquad (1.7)$$

$$E_{th} \propto {}^{1}/_{B} \qquad (1.8)$$

Hence, to obtain lower ASE E_{th}, higher k_r is needed. That also implies that a particular laser material should have a higher ϕ_{PL} and very short fluorescence lifetime (τ_F) as given in equation 1.9.

$$k_r = \frac{\phi_{PL}}{\tau_F} \qquad (1.9)$$

When such materials inscribe in a resonator structure, a narrower beam of laser can be obtained with resonating modes. A complete description of laser resonators and their characteristic emission will be discussed in section 1.4.

1.3.4 Triplet state

Triplet excitons formed in organics are very important when it comes to organic lasers, as it is one of the crucial factors to influence lasing behavior. Generally, the triplet state is a non-emissive state unless the spin-orbit coupling is high enough to make it emissive via an n-π*, π-π*, or metal-to-ligand charge transfer state as in heavy-atom-containing organo-metallic compounds[24]. The emission coming from the triplet state is known as phosphorescence. Moreover, phosphorescent OLEDs have been a real breakthrough in OLEDs as They have the internal quantum efficiency being higher by four-fold compared to traditional fluorescence OLEDs[30]. However, I here focus on the role played by triplet excitons on organic laser action.

1.3.4.1 Intersystem crossing (ISC)

Unlike in electrical injection (which directly makes ~25% of singlets and ~75% triplets [31]), in optical excitation, first, the singlet excited state is populated upon absorption of photons according to the spin conservation rule governed in optical transitions. Then these excited singlet excitons intersystem cross between spin forbidden isoenergetic states (S_1 (v = 0) T_1 ($v = n$)) of different multiplicity, because of the spin-orbit coupling to generate triplet excitons. This is an indirect formation of triplets. Because spin-orbit coupling is never zero, this gets much stronger presence of a heavy atom in a molecular structure[32]. Further, the lifetime of the triplet state lies in the µs-to-ms timescale range, which is quite long compared to short-lived singlet excitons (~ns) as the triplet excited state-to-singlet ground state relaxation is spin forbidden transition. As discussed in section 1.3.3.1, for ASE/laser performances, forming triplets via intersystem crossing is not very favorable as it reduces the singlet excitons in the laser system.

1.3.4.2 Triplet absorption (TA)

When triplet excitons absorb light of frequency *v*, they will be excited to the higher-lying triplet state of T_n, as shown in Figure 1.5. As the T_1-to-T_n transition is a spin allowed transition, TA is often a strong and broad spectrum in organic molecules. As a result, TA spectra usually stretch from wavelengths of fluorescence emission to further longer wavelengths, as shown in Figure 1.6[33]. Moreover, when these excited triplet excitons relax back to the T_1 state via radiationless transitions, excessive energy again will be converted into heat. However, the overlap of the triplet absorption spectrum over the fluorescence spectrum is not favorable for laser action since it will introduce extra quenching paths for singlet excitons in organic lasers.

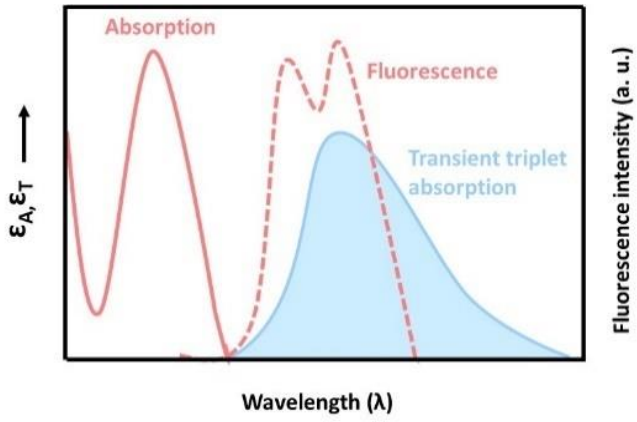

Figure 1.6. Triplet absorption spectrum overlaps with the fluorescence spectrum. ε_A and ε_T are absorption coefficients of singlet and triplet absorption, respectively.

1.3.5 Annihilation processes in organic semiconductors

There are several annihilation processes that take place in organic semiconductor lasers [34]. They are as follows:

1. Singlet-polaron annihilation (SPA)
2. Triplet-polaron annihilation (TPA)
3. Singlet-singlet annihilation (SSA)
4. Singlet-triplet annihilation (STA)
5. Triplet-triplet annihilation (TTA)

Some of these annihilation processes are more pronounced under electrical excitation than under optical excitation because many triplet excitons are formed in an organic semiconductor under electrical excitation.

In addition, there are two energy transfer mechanisms for the above annihilation processes. One is the long-range Förster Energy transfer process, which occurs via non-radiative dipole-dipole interactions. In this process, dipole-allowed transitions are favored. The second is a Dexter energy transfer, which is a short-range energy transfer process that enables energy transfer via close contact. This process does not require a transition to be dipole allowed [35]. Two of these processes are shown in Figure 1.7.

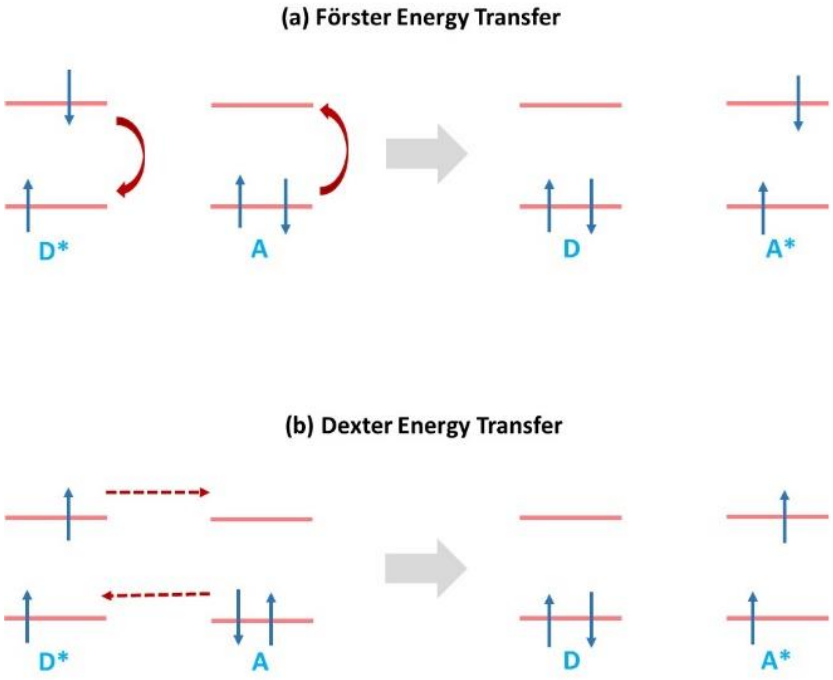

Figure 1.7. Energy transfer mechanisms. (a) Förster energy transfer with singlet excitons. (b) Dexter energy transfer enables diffusion of triplet excitons. The horizontal lines are the highest occupied molecular orbital (HOMO) and the lowest unoccupied molecular orbital (LUMO) energy levels of donor (D) and acceptor (A) molecules. The asterisk denotes the excited state. The arrows represent simultaneous rearrangement of the electronic configuration.

1.3.5.1 Singlet-polaron and triplet-polaron annihilation (SPA and TPA)

In this process, excited-state singlet excitons or triplet excitons will transfer the energy to positive/negative polarons and then relax back to the lower-energy state. Meantime this energy-absorbed positive/negative polaron will move to the higher-energy states as shown in Figure 1.8 via Förster energy transfer.

SPA and TPA are much more prominent in electrical excitation as polaron formation is abundant in electrically driven devices. The polaron absorption is one major loss mechanism of excitons in OSLDs.

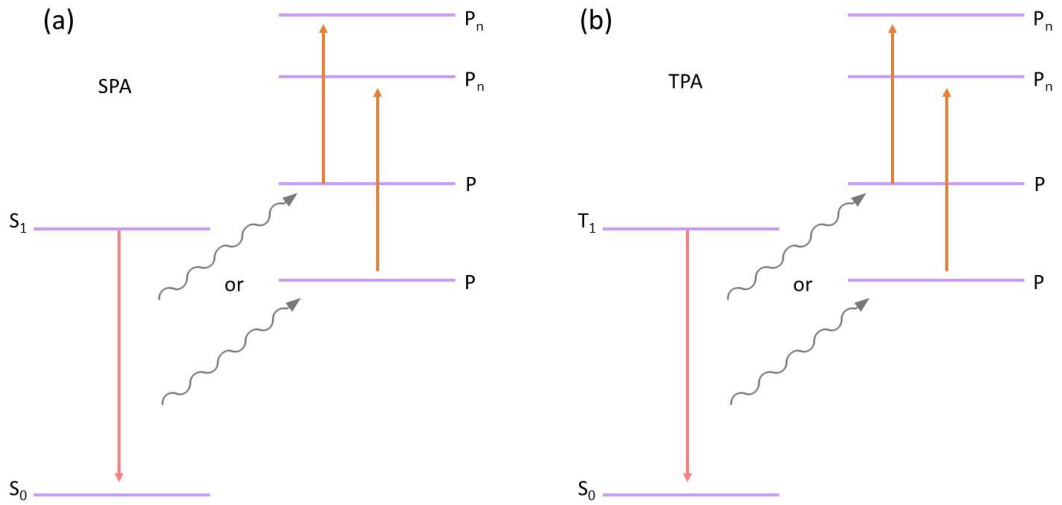

Figure 1.8. The mechanism of SPA and TPA. P denotes a polaron state and P_n denotes a higher-energy polaron state.

1.3.5.2 Singlet-singlet annihilation (SSA)

SSA is a loss mechanism of excited singlet states. In this process, one singlet exciton can be quenched by another excited-state singlet exciton. The energy of one singlet exciton is transferred to the other excited singlet state, generating the ground state and the even higher excited singlet state S_n as shown in equation 1.10. The latter higher-energy state eventually relaxes back to either the first excited singlet state (as shown in equation 1.11) or the triplet state (as shown in equation 1.12). This energy transfer process happens via Förster energy

transfer and concentration quenching of organic solid films can be explained from this annihilation process.

$$S_1 + S_1 \rightarrow S_0 + S_n \qquad (1.10)$$

$$S_n \rightarrow S_1 + heat \rightarrow S_0 \qquad (1.11)$$

$$S_n \rightarrow T_1 + heat \rightarrow S_0 \qquad (1.12)$$

1.3.5.3 Singlet-triplet annihilation (STA)

The STA process is a singlet exciton loss mechanism. When long lived triplet, excitons are accumulated in the laser system, the accumulated triplets will start to annihilate singlet excitons in the S_1 state.

In this process, the first excited singlet will be quenched by another triplet in the excited triplet state T_1 in its vicinity. As a result, the latter is getting excited to a higher triplet state while the former relaxes to its ground state as shown in equation 1.13. The molecule that is raised to an upper excited triplet state will then go down to the first excited triplet state as shown in equation 1.14, which eventually relaxes to the ground state.

$$S_1 + T_1 \rightarrow S_0 + T_n \qquad (1.13)$$

$$T_n \rightarrow T_1 + heat \rightarrow S_0 \qquad (1.14)$$

In this process, $S_1 \rightarrow S_0$ and $T_1 \rightarrow T_n$ are both spin-allowed, meaning that STA can happen through a Förster-type reaction. Further, Förster energy transfer takes place via non-radiative dipole-dipole interactions. This is efficient if the overlap between the singlet emission spectrum and the triplet absorption spectrum is large. The Förster energy radius can be determined from the overlap of the singlet emission and triplet absorption spectra as follows [36],

$$R_0^6 = \frac{9\ c^2\ f^2 \Phi_f}{128\pi^3 n^4} \int_0^\infty \sigma_{TT}(\nu) f_s(\nu) \frac{d\nu}{\nu^4}, \qquad (1.15)$$

where c is 2.993×10^8 ms^{-1}, f^2 is the orientation factor, which is 2/3 for random molecular orientation, σ_{TT} is the triplet-triplet absorption cross section, Φ_f is the emission quantum yield, n_s is the refractive index, and $f_s(\nu)$ is the normalized fluorescence spectrum, and ν is the frequency. When the triplet absorption spectrum is shifted as far as possible from the

fluorescence spectrum, the T_1 excitons will not be within the Förster radius to quench the singlet excitons. From this technique, STA can be suppressed in organics.

1.3.5.4 Triplet-triplet annihilation (TTA)

The TTA process is considered as a positive quenching process as it depletes long-lived triplet excitons and forms emissive singlet excitons out of triplets. To induce the process, energy of two triplet excitons which collide together should acquire an energy slightly above the energy of the first excited singlet state ($2E(T_1) > E(S_1)$) as shown in Figure 1.9 below[37]. During the triplet-triplet collision, the energy transfer mechanism happens via a Dexter energy transfer.

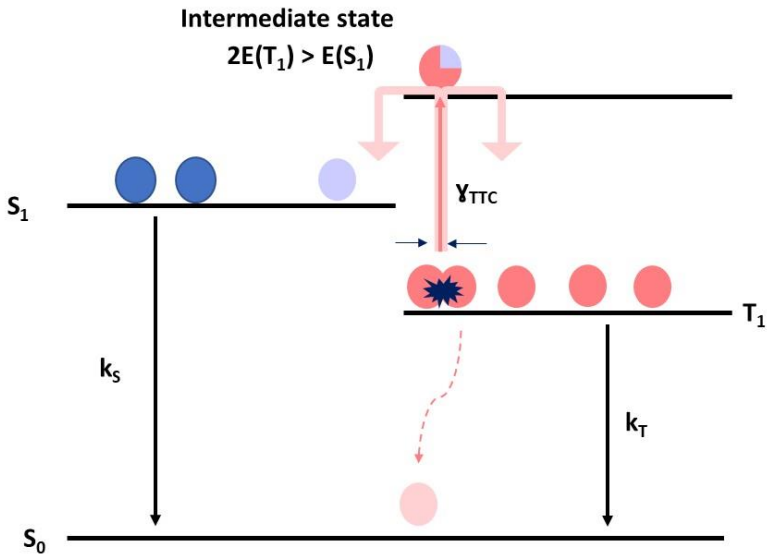

Figure 1.9. Schematics of the generation and decay paths of the TTA process. S_0, S_1, and T_1 denote the ground state, singlet excited state, and triplet excited state, respectively. k_S and k_T are monomolecular decay rates from singlet and triplet states, respectively. During triplet-triplet collision (TTC) with the rate constant γ_{TTC}, one of the triplets undergoes a nonradiative transition to the ground state (S_0, light pink circle). At the same time, the other one forms a higher-lying intermediate state with 1⁄4 singlet and 3⁄4 triplet character (quarter blue-filled, pink circle), which will eventually end up in the singlet state (light blue filled circle) or triplet state (pink circles)[38].

In the TTA process, there are three possible ways that the spins of two triplets can combine each other when they collide as shown above. The total spin (S) of the two triplets is given by equation 1.16

$$S = \Sigma m_s \qquad (1.16)$$

where m_s is the spin quantum number and the spin multiplicity is given by $(2S+1)$.

1. $[T_+(\uparrow\uparrow) + T\text{-}(\downarrow\downarrow)]$ = When the total spin of two triplets is zero (S = 0), it will result in a singlet state as spin multiplicity is 1. The probability of the singlet exciton formation is 1/9.
2. $[T_+(\uparrow\uparrow) + T_0(\uparrow\downarrow)]$ = When the total spin of two triplets is one (S = 1), it will result in a triplet state as spin multiplicity is 3. The probability of the triplet exciton formation is 3/9.
3. $[T_+(\uparrow\uparrow) + T_+(\uparrow\uparrow)]$ = When the total spin of two triplets is two (S = 2), it will result a quintet state as spin multiplicity is 5. The probability of the quintet formation is 5/9.

Then the intermediate state, which has a singlet character, will create a S_1 state and a S_0, as shown in equation 1.17. The intermediate state which has a triplet character will result in a T_1 state and a S_0 state as shown in equation 1.18. The intermediate state which has a quintet character will return back to the T_1 state following equation 1.19 as shown below.

$$\tfrac{1}{9}(T_1 + T_1) \rightarrow S_1 + S_0 \qquad (1.17)$$

$$\tfrac{3}{9}(T_1 + T_1) \rightarrow T_1 + S_0 \qquad (1.18)$$

$$\tfrac{5}{9}(T_1 + T_1) \rightarrow Q_1 \rightarrow T_1 + S_0 \qquad (1.19)$$

As a result, overall $1/4$ of probability will result in a singlet and $3/4$ of probability will result in a triplet in the system as shown in Figure 1.9 above. When these processes repeat for a certain period of time, the number of singlet excitons formed via the TTA process will eventually be increased.

1.3.6 Organic lasers under short-pulse photoexcitation

As discussed earlier, one of the determining factors in lasing is the triplet state, because the triplets eventually diminish the emissive singlet excitons via ISC, TA, and STA. However, as mentioned in section 1.3.3.1, materials with high photoluminescence quantum yield (PLQY) (ϕ_{PL}), high radiative decay rates ($k_r \sim 10^9$ s^{-1}), and very short fluorescence lifetime ($\tau_F \sim$ ns) make it possible to lase in short-pulse photoexcitation (ns pulses with a low repetition rate (10−20 Hz) are enough to relax the triplet excitons to the ground state) with the aid of a proper resonator structure[23]. Because long-lived triplets cannot influence immensely in this short-pulse photoexcitation as there is no chance for triplets to accumulate within this excitation. Under stimulated emission condition, excited singlet state lifetimes get much shorter than spontaneous emission lifetime. As a result, forming triplets via ISC can also be suppressed to a certain extent resulting in fewer triplets in the system. Therefore, even with moderate triplet absorption cross-section at a lasing wavelength, laser action might be observed [33]. Further, many organic laser materials with very low lasing thresholds ranging from μJ cm^{-2} to nJ cm^{-2} have been reported[39].

In addition, photons of a single-mode laser can be created by spontaneous emission and stimulated emission. There are two other loss mechanisms involved in the photon density of a laser. One is material loss happening via reabsorption from singlet ground state, singlet excited state, and triplet excited state. These are due to the material's intrinsic photophysical properties. Second is the losses caused by the cavity. This can be outcoupling losses or losses embedded in a laser resonator. Considering these factors, photon density q of a laser at time t can be written as in equation 1.20 as follows,

$$\frac{dq}{dt} = \left(\frac{dq}{dt}\right)_{stim} + \left(\frac{dq}{dt}\right)_{spont} + \left(\frac{dq}{dt}\right)_{material\ losses} - \frac{q}{\tau_{cav}} \qquad (1.20)$$

where τ_{cav} is the photon lifetime in the cavity. This is the dwelling time of a photon injected into an optical cavity before it couples out. By treating each term separately in equation 1.20, the final formula for photon density can be written as,

$$\frac{dq}{dt} = \left[\Gamma\sigma_{em}S_1 - \alpha_{reabs} - \frac{n_{eff}}{c\tau_{cav}}\right]\frac{c}{n_{eff}}q + \Gamma\sigma_{em}\frac{c}{V_{mode}}S_1 \qquad (1.21)$$

where S_1 is the population inversion for photon density q, n_{eff} is the effective refractive index, c is the velocity of light, V_{mode} is the mode volume, and α_{reabs} is the respective absorption cross-sections [σ_{ABS} ($S_0 \rightarrow S_1$), σ_{SS} ($S_1 \rightarrow S_n$), σ_{TT} ($T_1 \rightarrow T_n$)] at the laser wavelength and corresponding exciton densities in S_0, S_1, and T_1 states [24].

1.3.7 Organic lasers under CW photoexcitation

Lasing under CW is very difficult. Because triplets can influence the lasing activity severely under continuous photoexcitation. The three factors affecting the most for CW lasing are as follow:

1. Optical losses caused by triplet absorption
2. Singlet losses caused by STA
3. Thermal degradation

Under CW photoexcitation, the singlet state is continuously filled and eventually, these singlet excitons ISC to form triplets indirectly which will accumulate in the laser medium because of their longer lifetime as relaxing from the triplet state to the singlet ground state is a spin forbidden process. But as mentioned in the earlier section (section 1.3.4.2), the triplet absorption takes place to the higher-lying triplet state as it is a spin-allowed process rather than relaxing it down. However, a triplet absorption spectrum is a broad stretched spectrum which cannot be dismissed in organics. When this triplet absorption spectrum overlaps with the lasing wavelength, both optical losses and STA occur. As a result, laser action will shut down immediately. Therefore, both triplet absorption and STA are detrimental processes for CW lasing compared to short-pulse photoexcitation. The effect of STA and triplet absorption on CW lasing was theoretically studied by M. Lehnhardt et al.[40] and proved as the main cause of death of lasing in the CW regime.

Moreover, the higher-lying triplet excitons will eventually relax back to the first triplet excited state, releasing heat in the laser medium. In addition, continuous intense

photoexcitation will tend to degrade the organic molecules because of thermal degradation which also prevents CW lasing[41].

1.3.7.1 Condition for CW lasing

CW lasing is explained using two models. One is the constant rate model and the other is the constant yield model[24]. The constant rate model assumes all triplets being formed via ISC from the first singlet excited state with a rate of k_{ISC}. The constant yield model assumes that triplets are formed not only through ISC but also by fission happening by recombination of photogenerated polarons at high photoexcitation. Out of these two models, the constant rate model is simple and more popular to explain laser action in the CW regime. According to this model, the condition for CW lasing can be obtained as below.

The 4-level approximation

To make the laser work in the 4-level energy system as shown in Figure 1.5, several assumptions will be made as follows.

1. Bimolecular quenching processes like STA, SSA, and TTA are neglected.
2. Triplet state is neglected. As a result, triplet accumulation and subsequent phenomena can also be neglected.
3. The emission reabsorption from the S_1 to the higher excited singlet (S_n) is neglected.

Then, the rate equations for S_1 and S_0 can be written as follows:

$$\frac{dS_1}{dt} = \sigma_{abs} I_p S_0 - \left(\frac{1}{\tau_F} + \sigma_{em} I\right) S_1 \qquad (1.22)$$

$$\frac{dS_0}{dt} = -\sigma_{abs} I_p S_0 + \left(\frac{1}{\tau_F} + \sigma_{em} I\right) S_1 \qquad (1.23)$$

where I_p is the pump intensity (photons/m^2 s^{-1}), I is the intracavity laser intensity (photons/m^{2}s^{-1}), σ_{abs} is the absorption cross section (m^2), σ_{em} is the emission cross-section

(m^2), τ_F fluorescence lifetime (s), S_0 is the ground state population density, and S_1 is the singlet state population density.

$\sigma_{abs} I_p S_0$ = this term denotes the absorption of ground state singlets to excited state.

$\left(\frac{1}{\tau_F} + \sigma_{em} I\right) S_1$ = this term denoted the emission from spontaneous and stimulated emission.

Taking triplet state into account: 'Constant Rate' model

The 4-level model provides the platform to understand the mechanism of the organic lasers. But at the same time, it fails to capture the most of the interesting physics in the presence of a triplet state or bimolecular interactions. Triplet filling is also a well-known effect which generally hinders lasers from operating in the CW regime.

Constant rate model

An assumption is made that the triplets are formed only intersystem crossing (ISC) via S_1 state with an intersystem crossing rate k_{ISC} (s^{-1}). The rate equations in a 'constant triplets formation rate' can be written as follows:

$$\frac{dS_1}{dt} = \sigma_{abs} I_p S_0 - \left(\frac{1}{\tau_F} + \sigma_{em} I + k_{ISC}\right) S_1 \qquad (1.24)$$

$$\frac{dS_0}{dt} = -\sigma_{abs} I_p S_0 + \left(\frac{1}{\tau_F} + \sigma_{em} I\right) S_1 + \frac{T_1}{\tau_T} \qquad (1.25)$$

$$\frac{dT_1}{dt} = k_{ISC} S_1 - \frac{T_1}{\tau_T} \qquad (1.26)$$

where, T_1 is the triplet state population density and τ_T is the triplet lifetime (s).

In 'constant rate' approach, ISC is one of the channels which can be activated to deplete the singlet state with fluorescence, internal conversion, and stimulated emission. That is, if

stimulated emission is strong enough, then the feeding rate of the triplet level vanishes and as a result T_1 decreases when the laser intensity I increases.

CW lasing condition

To get the CW laser condition, the equation 1.26 is solved at steady state (d/dt = 0). The equation for the triplet state reads,

$$T_1^S = k_{ISC}\tau_T S_1^S \qquad (1.27)$$

where, T_1^S and S_1^S are the steady state population of the T_1 and S_1 state, respectively. In order to have a rough estimate, the following assumptions are made as follows.

1. TA is considered as the only cause of loss in the system.
2. Losses due to STA are neglected.
3. Losses due to cavity are neglected.

Then, CW lasing will be possible, whenever triplet absorption probability will be lower than stimulated emission probability as shown below,

$$\sigma_{TT}\, T_1^S < \sigma_{em}\, S_1^S \qquad (1.28)$$

where, σ_{TT} is the triplet-triplet absorption cross section. When T_1^S is substitute by equation 1.27, simplified condition for CW lasing is as follows,

$$\boldsymbol{\sigma_{TT}\, k_{ISC}\tau_T < \sigma_{em}} \qquad (1.29)$$

In general, most organic materials have similar value of ~ 10^{-16} cm^2 for σ_{TT} and σ_{em} . k_{ISC} is ~ 10^7 s^{-1} and τ_T is ~ 10^{-5} s. This indicates that the triplet state is filling much faster than it depletes. As a result, CW operation is difficult in organics [24].

In material point of view, good material should possess low triplet absorption cross-section, slow ISC rate, and small triplet lifetime to diminish the triplet population quickly from the laser medium. Moreover, triplet absorption spectrum should be shifted as much as possible away from the emission spectrum to satisfy the condition given in equation 1.29 at

a given wavelength within the emission spectrum because, relaxing the condition of ISC rate and triplet lifetime is very difficult.

1.3.7.2 Strategies to obtain CW lasing

As CW lasing is hard to get with organic materials under normal circumstances, several strategies can be implemented to suppress TA, STA, and thermal degradation problems. Generally, there are four main strategies to get CW lasing in this regime. With the studies explained in chapter 3 and 4, two more strategies could be introduced to get CW lasing. Then, overall CW laser strategies can be interpreted as six as shown below in Figure 1.10. In literature, two or more of these strategies were implemented simultaneously to obtain CW lasing.

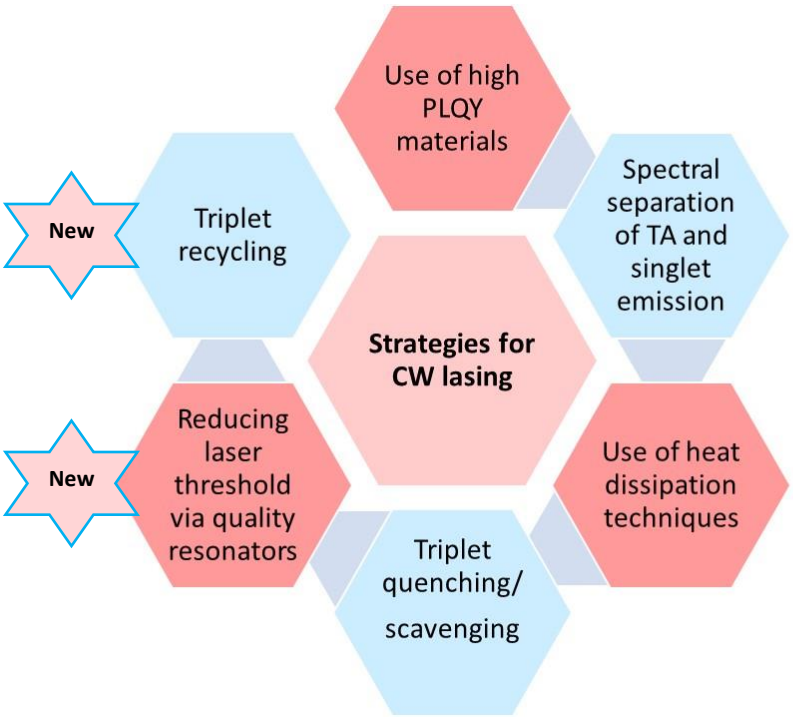

Figure 1.10. Strategies for obtaining CW lasing from organic semiconductors.

As shown in Figure 1.10, one method is to use organic materials with high PLQYs since it reduces the formation of triplets *via* ISC from singlets. That will eventually lead to a

lesser number of accumulated triplets in the laser system. Few examples for high PLQY materials are pyrene-cored dendrimers[42], styrylbenzene-based molecules such as (2Z,2'Z)-3,3'-(1,4-phenylene)bis(2-(4-butoxyphenyl)acrylonitrile) (β-DBDCS)[43], and trimer (dimer) oligo(9,9-diarylfluorene) derivatives[44]. However, all high PLQY materials will not work under CW regime unless these materials' lasing windows are free of excited state absorptions.

The other possible method is to use organic materials which have a spectral separation of singlet emission from triplet absorption, as shown in Figure 1.11. As the spectral overlap of singlet emission and triplet absorption is negligible, Förster energy transfer is not favorable to occur STA[33]. However, finding such materials is practically limited. 4-4′-bis[(*N*-carbazole)styryl]biphenyl (BSBCz) and poly 9,9-dioctylfluorene (PFO) derivative containing 12% of statistical intrachain of 6,6-2,2-octyloxy-1,1-binaphthalene binaphthyl (BN-PFO) are some examples for such materials without the spectral overlap [27, 45, 46].

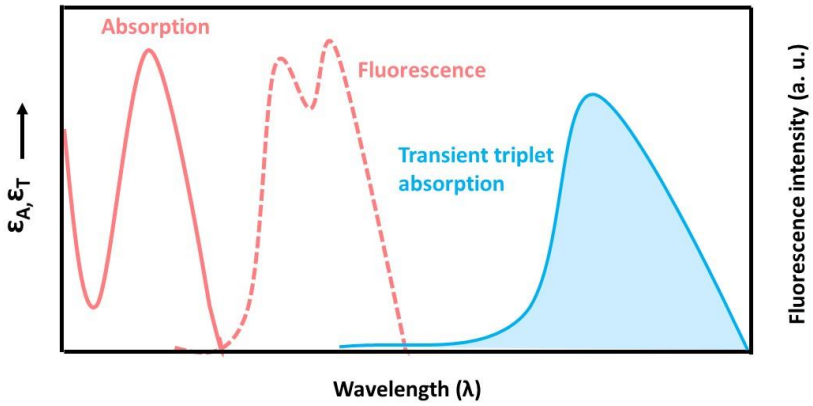

Figure 1.11. Spectral shift of triplet absorption and fluorescence is ideal for CW lasing.

Another well-known method is to use triplet quenching molecules such as molecular oxygen having a triplet ground state. However, the use of molecular oxygen enhances the ISC rate and sometimes oxidizes the organic molecules, which is not ideal for use in lasing systems [47]. The use of triplet-scavenging molecules, such as 1,3,5,7-cyclooctatetraene[47, 48] and anthracene[49, 50] molecules, has also been reported as an efficient method to eliminate the accumulated triplets from laser systems. Additionally, these triplet-scavenging molecules

should satisfy several conditions to eliminate the triplets efficiently from laser systems, as shown in Figure 1.12.

- First, these molecules should possess a deep triplet energy state (T_1) than the laser dye molecules to scavenge the accumulated triplets on organic laser dye.
- On the other hand, these molecules should have a high-lying singlet energy level (S_1) to prevent the quenching of the singlet excitons of the organic laser dye molecules. Thus, triplet scavenging molecules should possess a large S_1–T_1 energy gap.
- Moreover, a short triplet lifetime of these molecules is also essential for the triplets to decay non-radiatively from laser systems.
- A spectral separation of triplet absorption of triplet scavenging molecules from the lasing region of organic laser dye molecules is also essential for efficient laser performance without inducing STA in the laser systems.
- Moreover, these triplet scavenging molecules should not induce ISC of the radiative singlets of laser dye molecules for efficient laser performances.

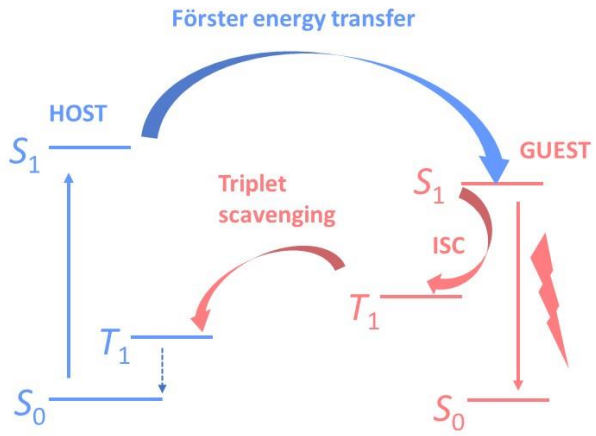

Figure 1.12. Triplet scavenging mechanism of a host-guest system. Straight arrows represent the absorption and emission of host and guest, respectively. Blue curved arrow represents the Förster energy transfer. Pink curved arrows represent the ISC and triplet scavenging mechanisms. Dashed arrow represents the non-radiative relaxation from the host triplet state to the ground state.

One other method is to implement heat dissipation techniques to reduce the thermal degradation of laser materials under prolong intense photoexcitation[21, 41]. This can be

suppressed by designing new device architectures to dissipate heat efficiently from the laser system.

Reducing the laser oscillation threshold via higher feedback resonators is one other method to get CW lasing. In the case of a low lasing threshold, the laser will reach the threshold condition with the aid of lower excitation power which will eventually suppress the degradation of the laser medium. At the same time, very short stimulated emission lifetime will reduce the formation of triplets in the laser medium via ISC. This will be discussed in more detail in chapter 3.

Finally, triplet excitons can be recycled via TTA or else using thermally activated delayed fluorescence (TADF) materials with a high ISC rate[22, 27]. According to the literature, there have been no studies reported using these two methods so far for CW lasing. However, this thesis mainly focuses on the former method and will be discussed elaborately in chapter 4.

1.3.7.3 CW/quasi continuous-wave (qCW) lasing from organic semiconductors

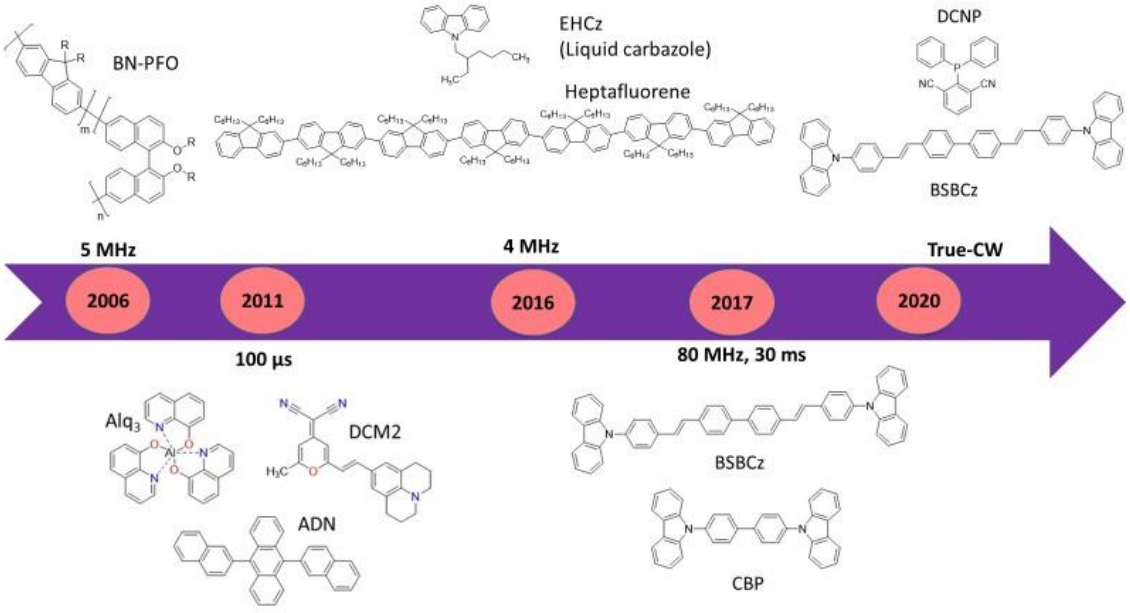

Figure 1.13. Milestones of organic qCW/CW lasing[46, 49, 51, 21, 52].

qCW lasing can be obtained via two approaches. One method is to operate the laser at a high repetition rate (~kHz or above). The other method is to operate it under longer pulses (~μs above). Considering these approaches, Figure 1.13 summarizes the most significant works which have been reported in qCW/CW regime. All these works were reported by implementing two or more strategies to get CW lasing. The history of CW lasing and the detail explanation of the significant works shown in Figure 1.13 are given as follows.

The first CW organic laser was reported in 1970 by O. G. Peterson et al. used a dye solution of rhodamine 6G in water[53]. In this laser, dye circulation was used to remove the accumulation of triplets. Later in 1971, F. C. Strome Jr et al. reported CW lasing using fluorescein in ethanol solution[54]. In this work, anthracene and cyclooctatetraene were used as triplet scavengers. These works were done in a solution state and they were not favorable for future laser applications. After thirty years later, in 2006, R. Bornemann reported the first solid-state dye laser using rhodamine 6G dissolved in a tailored photopolymer[55]. The device was a disk and it was rotated to get CW lasing. In all these works, mechanical circulation or rotation of samples was used to avoid triplet accumulation.

In 2006, T. Rabe et al. showed qCW lasing up to 5 MHz using poly PFO derivative containing 12% of statistical intrachain spacer groups BN-PFO in a second-order DFB structure as shown in Figure 1.13 [46]. In BN-PFO molecules, triplet formation via ISC was very weak and the triplet absorption spectrum also red-shifted from the lasing wavelength which makes the molecules lase even under a high repetition rate without STA. However, when BN-PFO was incorporated in a host matrix of 1,4-bis(2-(4-(N,N-di(p-tolyl)amino)phenyl)vinylbenzene (DPAVB), using the host-guest system ceased the lasing quickly at a high repetition rate because of the spectral overlap of the triplet absorption of DPAVB with the fluorescence of BN-PFO claiming the importance of separation of triplet absorption from the lasing wavelength[56]. Figure 1.14 shows the molecular structure of the BN-PFO, threshold variation with repetition rate, and streak camera image at 1 MHz which looks exactly CW laser emission. Hence the strategy used in this work is high PLQY and spectral separation of triplet absorption from lasing wavelength.

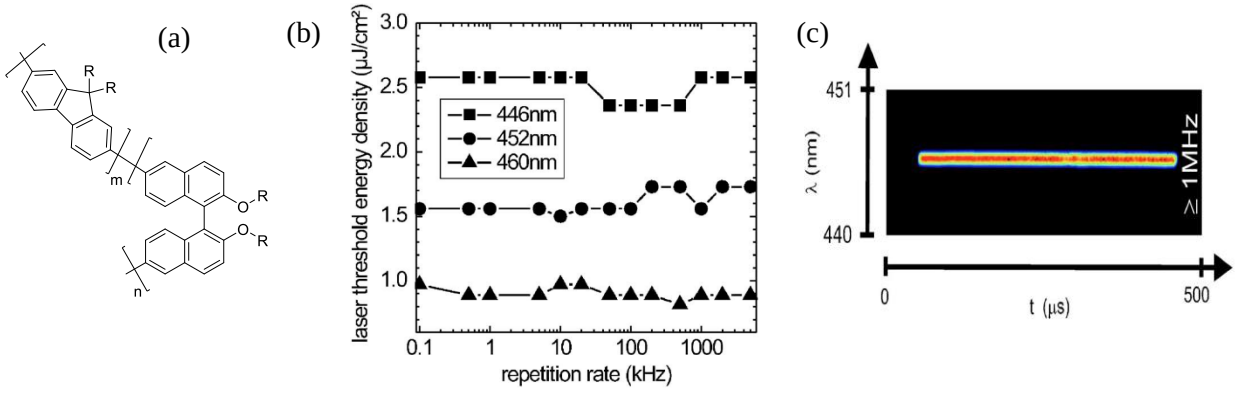

Figure 1.14. (a)Molecular structure of BN-PFO, (b) laser threshold variation with repetition rate, and (c) streak camera image of the laser emission up to 1 MHz[46].

Triplet management in the laser medium with the aid of a triplet scavenger with their deep-lying triplet state is also a promising method for CW lasers. This method was efficiently used by Zhang et al. in 2011, with a red-emitting laser dye 4-(dicyanomethylene)-2-methyl-6-julolidyl-9-enyl-4H-pyran (DCM2) in tris(8-hydroxyquinoline) Al (Alq_3)[49]. To manage the triplets formed via ISC from the singlet state on both DCM2 and Alq_3, a triplet manager 9,10-di(naphtha-2-yl)anthracene (ADN) was used as shown in Figure 1.15. In this system, host blend (Alq_3 and ADN) energy transfers to the guest S_1 state via Förster energy transfer and the triplets formed on both molecules (Alq_3 and DCM2) via intersystem crossing will end up in the deep T_1 state of the triplet manager ADN (T_1 = 1.69 eV, S1 = 2.83 eV) via Dexter energy transfer. When increasing ADN concentration in the system, STA was significantly decreased. Moreover, triplet absorption of the manager was shifted from the guest emission. Therefore, optical losses and singlet quenching in the Alq_3:DCM2 were significantly reduced. Laser was consisted with second-order DFB with a pitch size of 430 nm and a height of 50 nm. This system worked up to 100 μs and reported that the operation time could have extended even to CW if the molecule degradation was not taken place.

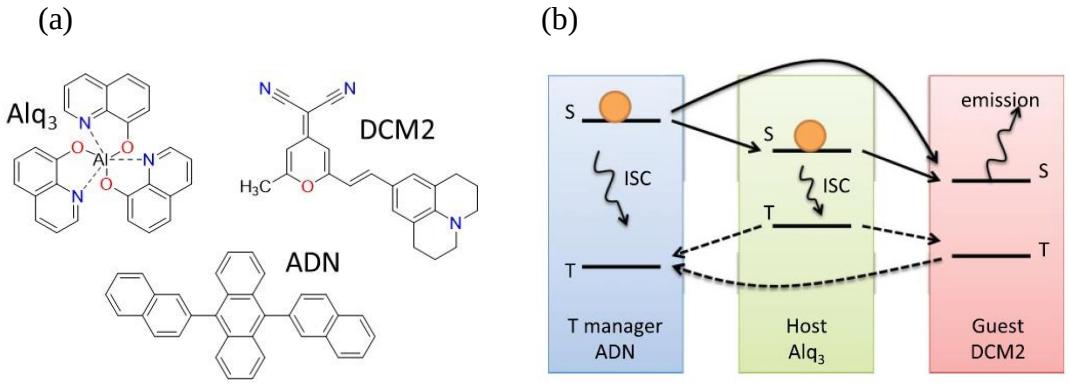

Figure 1.15. (a) Molecular structures of Alq_3, DCM2, and ADN and (b) energy diagram of the Alq_3:DCM2:AND system [49].

qCW lasing with a repetition rate of up to 4 MHz in a liquid system of heptafluorene dissolved in liquid 9-(2-ethylhexyl)carbazole (EHCz) was realized by Sandanayaka et al. by bubbling the system with oxygen to remove the detrimental triplets from the laser medium. This is a solvent free liquid-based system[51]. First, EHCz and heptafluorene were mixed with chloroform solution (EHCz:heptafluorene = 90:10) and two samples were bubbled with O_2 and N_2 for 20 min, separately. Then it was kept to evaporate the solvent. This host:guest system showed a PLQY of 85% and found to have a very low ISC rate. On the other hand, triplet absorption spectrum of heptafluorene was well separated from the lasing medium reducing optical and S_1 exciton losses. The DFB was a polymeric DFB structure prepared with an ultraviolet (UV) curable polyurethaneacrylate (PUA) mixture. Laser emission was obtained from the edge of the device by inscribing a first-order DFB structure. Figure 1.16 (a) and (b) shows the molecular structures, streak camera images obtained at different repetition rate with two devices which bubbled N_2 and O_2 respectively. O_2 bubbled device laser emission was more intense compared to N_2 bubbled devices. This claims that triplets were quenched efficiently in the presence of O_2 in the laser device. To reduce 10% of the initial intensity of the laser emission of this device took around 5 min as shown in Figure 1.16 (c). Further, apart from using O_2 to quench detrimental triplets in the medium, use of a high PLQY material with negligible overlap of triplet absorption at lasing wavelength made

the work much more efficient. This work was limited up to 4 MHz because of the photobleaching of heptafluorene molecule.

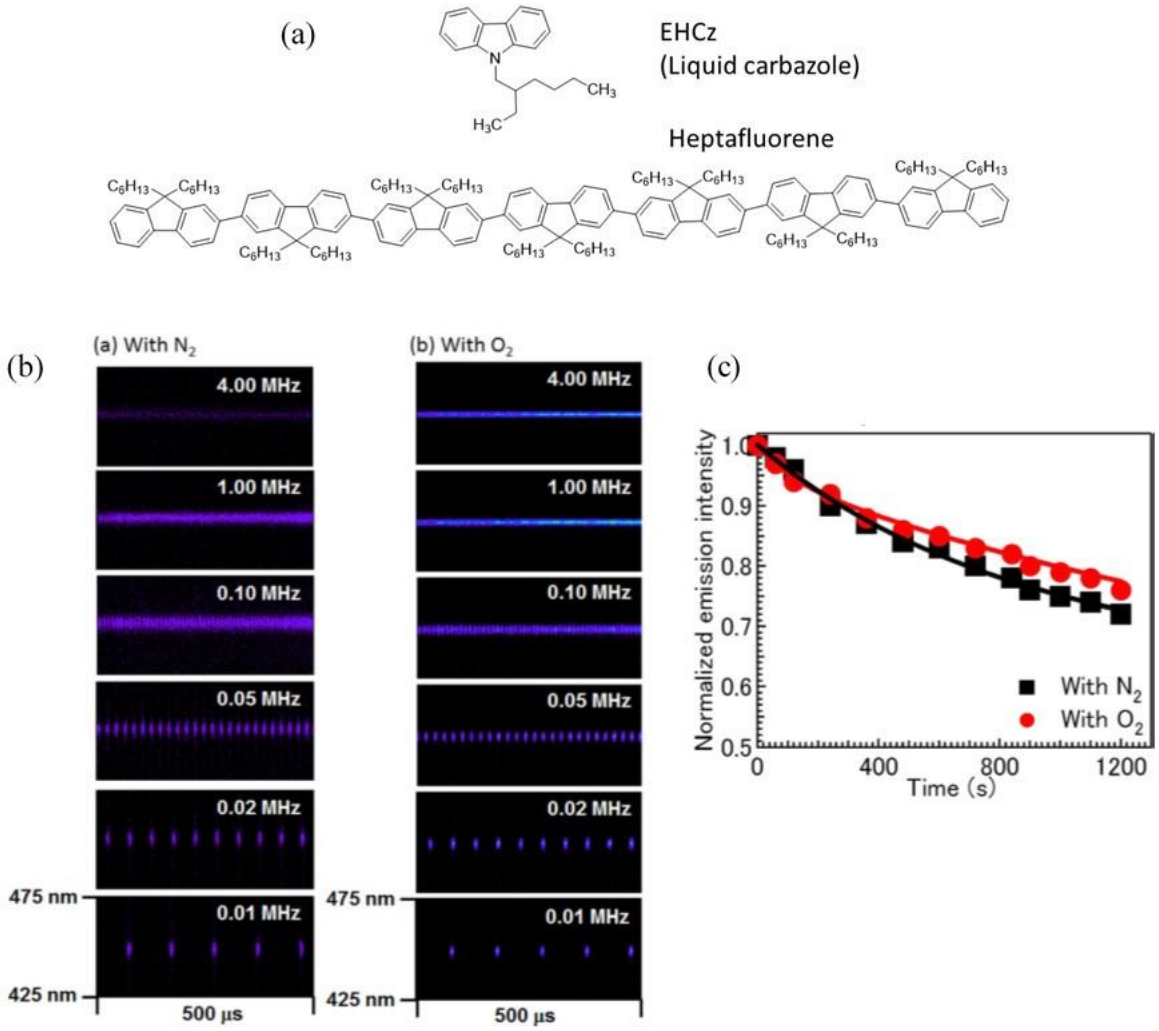

Figure 1.16. (a) Molecular structures of EHCz and heptafluorene, (b) Streak camera images of the laser emission of the laser devices which bubbled N_2 and O_2 separately and (c) stability of the laser devices under 1 MHz repetition rate with an excitation power of 2.5 µJ cm^{-2} [49].

BSBCz is also a very promising molecule, which shows ~100% PLQY when blended with 4,4′-bis(*N*-carbazolyl)-1,1′-biphenyl (CBP), with a very low ASE threshold of 0.3 µJ cm^{-2} [45]. The molecular structures are shown in Figure 1.17 (a). This shows a well-separated

triplet absorption spectrum from the lasing wavelength, as shown in Figure 1.17 (b)[57]. Moreover, BSBCz has a large stimulated emission cross-section than the triplet absorption cross-section at a lasing wavelength of 480 nm, which is promising for CW lasing.

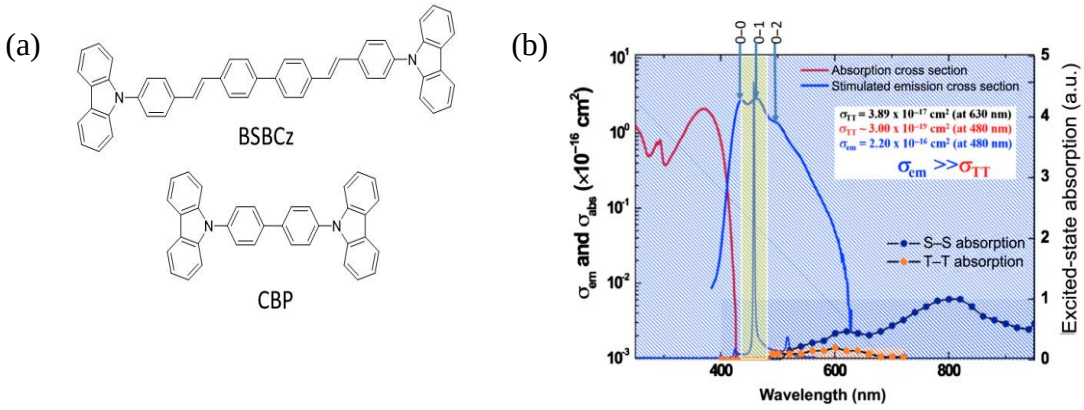

Figure 1.17. (a) Molecular structures of BSBCz and CBP and (b) excited state absorption of triplets and singlets of BSBCz which are well separated from the ASE emission wavelength of BSBCz [28, 57].

In 2007, Nakanotani et al. showed threshold less CW ASE from BSBCz:CBP blend films [57]. Later in 2016, Sandanayaka et al. incorporated BSBCz:CBP in a second-order DFB structure and achieved qCW lasing, with a repetition of up to 8 MHz[58]. This work was further improved by reducing the laser threshold by introducing a mixed-order DFB structure and encapsulating the device with high-thermal-conductive sapphire substrates and fluoropolymer CYTOP to stand the heat under prolong CW photoexcitation. This new device architecture led the performance to increase the repetition rate from 8 MHz to 80 MHz as shown in Figure 1.18 and even up to 30 ms in qCW operation[21]. The importance of heat management under CW operation was also pointed out by Zhao et al. in 2014[41].

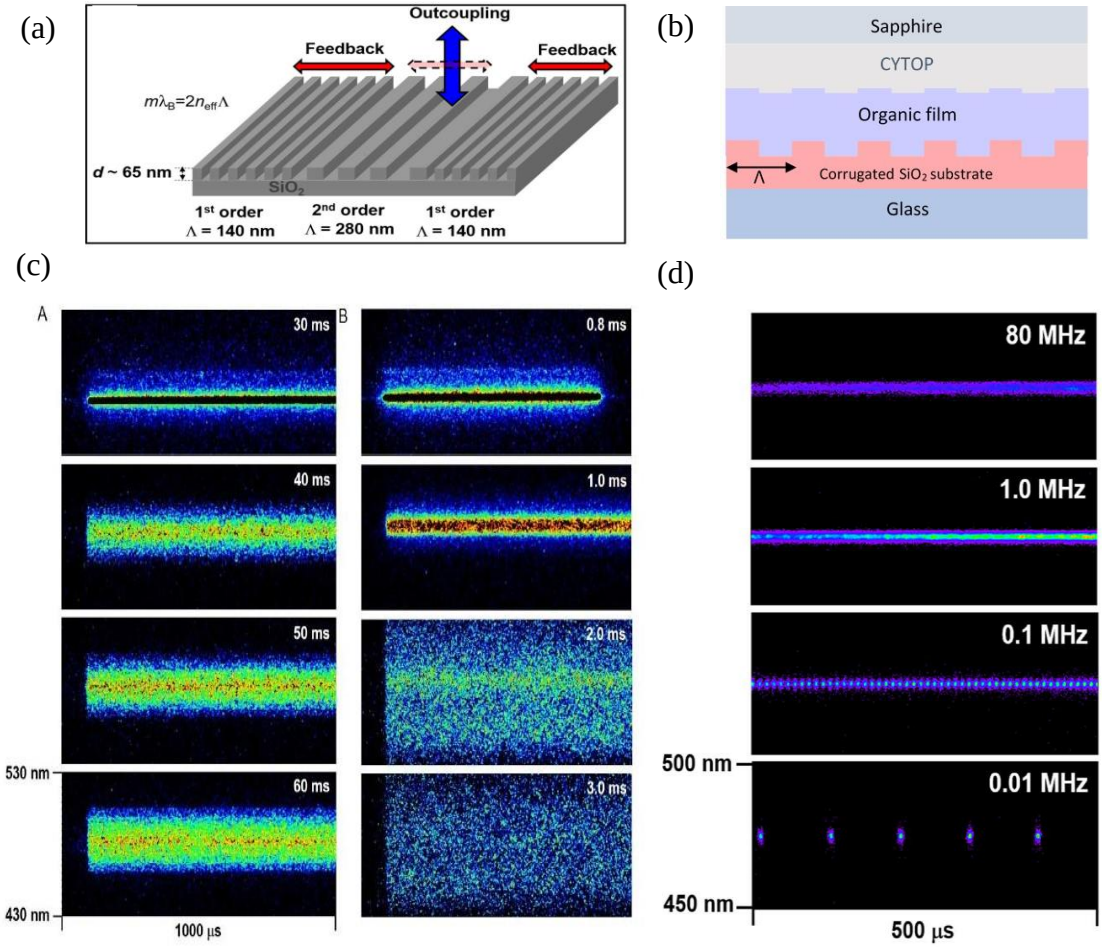

Figure 1.18. (a) Schematic diagram of the mixed-order DFB structures used, (b) the schematic diagram of the encapsulated device architecture, (c) streak camera images of the laser emission of the laser devices with encapsulating CYTOP and sapphire which works up to 30 ms (A) and the devices encapsulated with CYTOP and glass which works up to 0.8 ms (B), and (d) streak camera images of the laser emission up to 80 MHz with in the 500 μs time window [21].

Later, Karunathilaka et al. showed that BSBCz could be used directly as a triplet scavenger host due to its deep triplet state and short triplet lifetime with green-emitting small-molecular organic laser dye 2,6-dicyano-1,1-diphenyl-$\lambda^5\sigma^4$-phosphinine (DCNP)[52]. In this system, BSBCz acts as a scavenger/manager via its deep T_1 state to the triplets formed on DCNP molecule via ISC from its own S_1 state. As a result, triplets will not get accumulated

on the DCNP molecule and the system could work up to true-CW lasing. This works is different than the Alq_3:DCM2:ADN system. In Alq_3:DCM2:ADN system, Alq_3 acts as the host and ADN acts as the triplet manager. On the other hand, ADN cannot be used as a host due to aggregation occurring at high concentration. But in this DCNP:BSBCz system, BSBCz solely plays the both roles as a host and the triplet scavenger at the same time. Laser devices were fabricated inscribing first-order, second-order, and mixed-order DFBs and the true-CW lasing threshold was achieved at a threshold of 120 W cm^{-2} using mixed-order DFB structure. 1 wt % DCNP:BSBCz showed a PLQY of 83%. All these devices were encapsulated with CYTOP and sapphire to dissipate heat efficiently under prolong photoexcitation. In addition, triplet absorption spectrum of BSBCz has a very small overlap with the emission spectrum of the DCNP and the authors noted that BSBCz's triplet lifetime is very short (~224 ns) which is again helpful to overcome the optical losses and singlet excitons losses in the laser device. Finally, main strategy used to get CW lasing with this system is triplet scavenging. Further, use of high PLQY material and implementing good heat dissipation techniques in the laser device makes it work more efficiently in the true CW regime. Figure 1.18 shows the energy transfer diagram of BSBCz and DCNP.

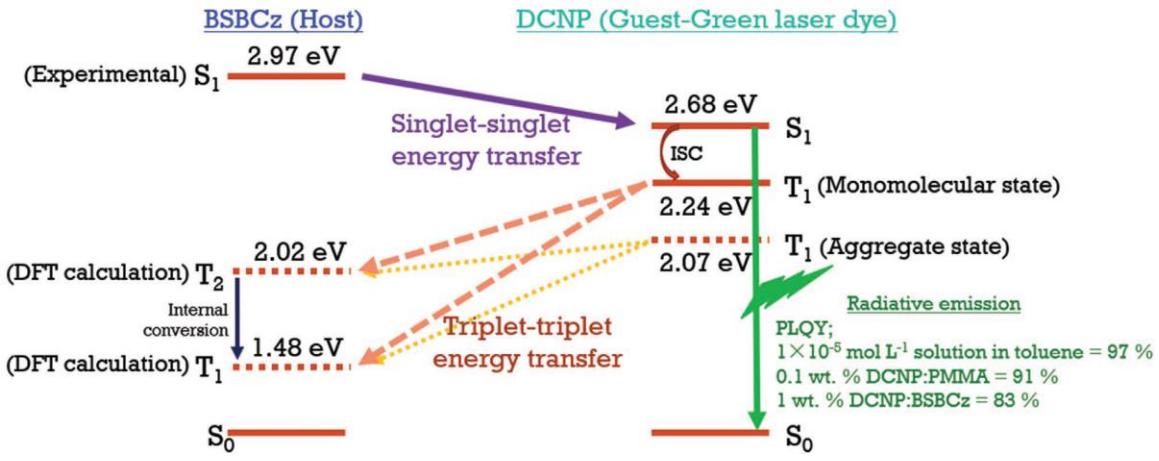

Figure 1.19. Energy transfer diagram of the BSBCz and DCNP.

1.4 Optical resonators

An optical resonator/optical cavity is an essential component in a laser device, which facilitates feedback of light through the gain medium to establish an intense, coherent field of light. Basically, the resonator imposes two basic properties on the laser output. First, the resonator defines the allowed resonant frequencies within the gain spectrum. That is the emission wavelength of the laser field. Second, the resonator defines the spatial characteristics of the emitted laser beam. These properties arise from the fundamental boundary conditions of the laser field in a cavity [59]. That is, the phase and amplitude of laser light traveling in a cavity should be conserved following a round trip resulting in a discrete set of frequencies. These specific frequencies are known as longitudinal or axial modes of a laser resonator. On the other hand, the resonator facilitates transverse modes that are self-replicating following a round trip in the resonator, and it determines the transverse light pattern of the output laser beam [23, 59].

Different types of resonators have been reported in organic semiconductors. The simplest resonator is a Fabry-Perot resonator, which comprises two mirrors (full and partially reflective mirrors) supporting a standing wave. There are other resonators such as planar microcavity, microring, microdisk, and distributed feedback resonators [60]. Figure 1.20 shows some of the resonator structures discussed above. Planar microcavities are a sandwich of the gain medium between reflective distributed Bragg reflective mirrors (DBR). One of the DBR mirrors is partially transparent in the spectral range where the gain medium can emit the light extraction. Micro-ring and disk resonators provide longer interaction length with the gain medium with many longitudinal modes. These resonators show a low threshold but with no directionality.

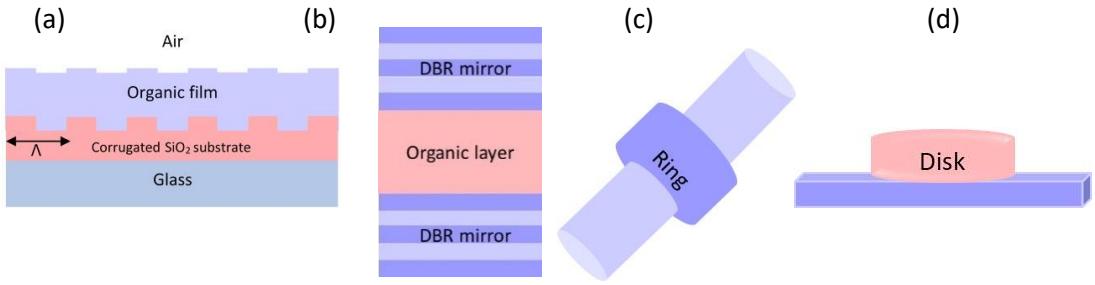

Figure 1.20. Schematics of the resonators used in organic semiconductor lasers. (a) Distributed feedback resonator, (b) planar microcavity, (c) microring resonator coated around an optical fiber, and (d) microdisk resonator.

1.4.1 Distributed feedback resonators

Distributed feedback (DFB) gratings are optical resonators which facilitate lasing with low thresholds, precise mode selection with a well-defined narrow laser beam. This was first introduced by Kogelnik and Shank in 1970[61]. As shown in Figure 1.15(a) SiO_2-organic gain medium-air structure forms an asymmetric slab waveguide. The feedback happens in the waveguide of a wavelength-scale periodic corrugated structure. Each corrugation gives rise to Bragg scattering of the waveguide mode. By carefully determining the grating period (Λ) using Bragg equation,

$$2n_{eff}\Lambda = m\lambda_{\boldsymbol{B}} \qquad (1.30)$$

where, n_{eff} is the effective refractive index, m is the order of diffraction, $\lambda_{\boldsymbol{B}}$ is the Bragg wavelength, one can arrange that optical wavelength close to the peak of the organic gain to Bragg scatter when propagating and counter-propagating the wave by providing a distributed resonant feedback for the laser operation.

In most cases, second-order (*m* = 2) DFB gratings are used over first-order (m = 1) grating structures as surface emission is favored in many applications. In second-order DFBs, second-order diffraction facilitates feedback and surface light outcouples occur via the first-order diffraction. However, threshold is a bit higher in these second-order DFBs compared to first-order DFB structures because of energy loss. First-order DFBs are edge emitters and result in a very low lasing threshold because of less energy loss. However, practical difficulties arise in these first-order laser devices in terms of fabrication and measurements. To overcome this problem, mixed-order DFBs were introduced by combining first-order and second-order periods[62]. In mixed-order DFB structures, feedback occurs via first-order regions and light outcouples via second-order regions giving rise to a low lasing threshold compared to second-order DFBs. First-order, second-order, and mixed-order DFB structures are shown in Figure 1.21 below.

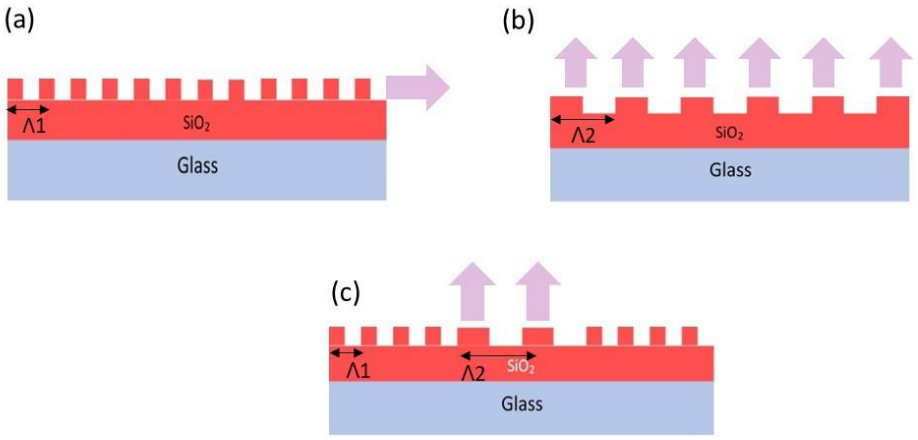

Figure 1.21. Schematics of first-order, second-order, and mixed-order DFB structures.

In addition to conventional 1-D DFB structures, there are 2-D and 3-D DFB structures that can facilitate more feedback in the 2D and 3D plane and result in a very low lasing threshold by confining the light in the laser device. However, fabricating 3-D DFBs is more difficult than fabricating 1-D or 2-D DFB structures. Therefore, more interest on 2-D DFBs

has attracted over the years to introduce high feedback in laser devices and this will be discussed in detail in chapter 3.

1.5 Aim and outline of the thesis

1.5.1 Organic semiconductor laser diode (OSLD)

The most awaited study in organic laser research was to realize OSLD. This dream came true in 2019, realizing electrically injected lasing from BSBCz using an inverted OLED device as shown in Figure 1.22[17]. OSLDs are applicable in retina displays, sensors, photodynamic therapy, and screens with high spectral purity.

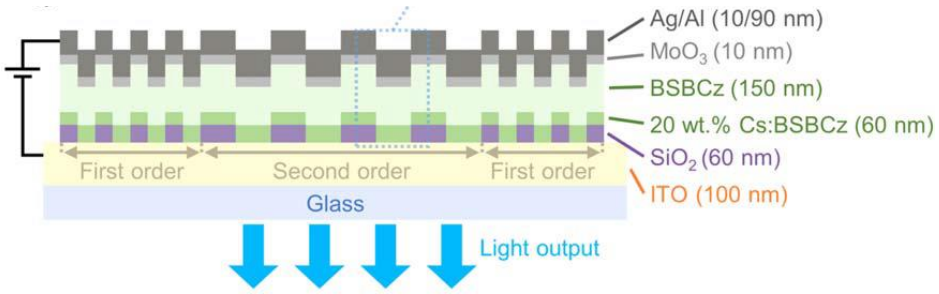

Figure 1.22. Schematic of the device architecture of the OSLD.

However, realizing OSLD was a long being problem due to optical losses arise from electrical contacts and electroluminescence losses induced from triplets and polarons. Having a well separated triplet absorption spectrum from a lasing window of BSBCz facilitated less STA and low external quantum efficiency (EQE) roll-off in BSBCz-based OSLDs for electrical pump laser action. However, the electrical pump lasing threshold was found to be very high ~ 600 A cm^{-2} which then brings about stability issues. Therefore, still many works have to be carried out to obtain efficient, stable, low threshold electrical lasing from organics for future commercialization.

1.5.2 Aim of my work

Realizing stable true-CW lasing makes one step closer towards realizing stable OSLDs as true-CW lasers can suppress STA losses arising under electrical excitation and alleviate EQE roll-off in OLED devices. This triggered the work reported in this thesis to find out much more efficient laser materials and strategies for true-CW lasing for the future realization of high-performance OSLDs.

Up to date, many techniques have been studied to suppress the STA and thermal degradation of organic laser devices being operating under qCW photoexcitation. However, only one study was reported to exhibit true-CW lasing with green emission[52]. There has been no report on true-CW lasing in the blue region. Therefore, in Chapter 2 of this thesis, I focus my attention on solution-processable blue-emitting organic semiconductor materials for qCW laser emission. Because solution-processable lasers provide the chance to make large-area laser devices. On the other hand, blue laser material will help to enhance the high spectral purity in blue emission region in future OSLDs.

In Chapter 3, I study how lowering laser emission threshold affects CW lasing and laser stability using 2-D DFB structures.

In Chapter 4, I investigate the use of detrimental triplet exciton for CW lasing via triplet recycling with TTA, which will also be very useful for future OSLDs.

In Chapter 5, I summarized this thesis and proposed prospects.

References

[1] A. Einstein, *Phys. Z.*, **1917**, *18*, 121.

[2] K. F. Renk, *Basic of laser physics for students of science and engineering*; Springer, 2017; pp. 4-18.

[3] A. L. Schawlow, C. H. Townes, *Phys. Rev*., **1958**, *112*, 1940.

[4] The laser at about 40, Available at: https://www.scientificamerican.com/article/the-laser-at-about-40/

[5] T. Maiman, *Nature*, **1960**, *187*, 493.

[6] Lasers: Understanding the basics, Available at: https://www.photonics.com/Articles/Lasers_Understanding_the_Basics/a25161

[7] O. Svelto, *Principles of Lasers*, Springer, 1998; pp. 255-313.

[8] Continuous-wave lasers, Available at: https://www.laserquantum.com/products/continuous-wave.cfm

[9] E. G. Brock, P. Czavinsky, E. Hormats, H. C. Nedderman, D. Stirpe, F. Unterleitner, *J. Chem. Phys*., **1961**, *35*, 759.

[10] S. G. Rautian, I. I. Sobel'man, *Opt. i Spekt*., **1961**, *10*, 134.

[11] P. P. Sorokin, J. R. Lankard, *IBM J. Res. Dev.*, **1966**, *10*, 162

[12] B. H. Soffer, B. B. McFarland, *Appl. Phys. Lett*., **1967**, *10*, 266.

[13] C. W. Tang, S. A. Vanslyke, *Appl. Phys. Lett.*, **1987**, *51*, 913.

[14] F. Hide, M. A. DiazGarcia, B. J. Schwartz, M. R. Andersson, Q. B. Pei, A. J. Heeger, *Science*, **1996**, *273*, 1833N.

[15] Tessler, G. J. Denton, R. H. Friend, *Nature*, **1996**, *382*, 695.

[16] A. J. C. Kuehne, M. C. Gather, *Chem. Rev.*, **2016**, *116*, 12823.

[17] A. S. D. Sandanayaka, T. Matsushima, F. Bencheikh, S. Terakawa, W. J. Potscavage, C. Qin, T. Fujihara, K. Goushi, J. C. Ribierre, C. Adachi, *Appl. Phys. Express.*, **2019**, *12*, 061010.

[18] O. S. Avanesjan, V. A. Benderskii, V. K. Brikenstein, V. L. Broude, L. I. Korshunov, A. G. Lavrushko, I. I. Tartakovskii, *Mol. Cryst. Liq. Cryst*.,**1974**, *29*, 165.

[19] D. Moses, *Appl. Phys. Lett*., **1992**, *60*, 3215.

[20] W.-Y. Lai, R. D. Xia, Q. Y. He, P. A. Levermore, W. Huang, D. D. C. Bradley, *Adv. Mater*., **2009**, *21*, 355.

[21] A. S. D. Sandanayaka, T. Matsushima, F. Bencheikh, K. Yoshida, M. Inoue, T. Fujihara, K. Goushi, J-C. Ribierre, C. Adachi, *Sci. Adv.* **2017**, 3, e1602570.

[22] D.-H. Kim, A. D'Ale´o, X.-K. Chen, A. D. S. Sandanayaka, D. Yao, L. Zhao, T. Komino, E. Zaborova, G. Canard,Y. Tsuchiya, E. Choi, J. W. Wu, F. Fages, J.-L. Bre´das, J.-C. Ribierre, C. Adachi, *Nat. Photonics*, **2018**, *12*, 98.

[23] I. D. W. Samuel, G. A. Turnbull, *Chem. Rev.*, **2007**, *107*, 1272.

[24] S. Forget, S. Chénais, *Oraganic Solid State Lasers*, Springer, 2013; pp. 13-62.

[25] M. D. McGehee, A. J. Heeger, *Adv. Mater.*, **2000**, *12*, 1655.

[26] M. Anni, S. Lattante, *Organic Lasers Fundamentals, Developments and Application*, Pan Stanford Publishing Pte. Ltd., 2018; pp. 23-72.

[27] H. Nakanotani, T. Furukawa, T. Hosokai, T. Hatakeyama, C. Adachi, *Adv. Optical Mater.*, **2017**, *5*, 1700051.

[28] C. Adachi, A. S. D. Sandanayaka, *CCS Chem*., **2020**, *2*, 1203.

[29] T. Komino, H. Nomura, M. Yahiro, K. Endo, C. Adachi, *J. Phys. Chem. C*, **2011**, *115*, 19890.

[30] C. Adachi, M. A. Baldo, M. E. Thompson, S. R. Forrest, *J. Appl. Phys*., **2001**, *10*, 15.

[31] M. A. Baldo, D. F. O'Brien, M. E. Thompson, S. R. Forrest, *Phys. Rev. B - Condens. Matter Mater. Phys.*, **1999**, *60*, 14422.

[32] A. Köhler, H. Bässler, *Mater. Sci. Eng. R*, **2009**, *66*, 71.

[33] T. G. Pavlopoulos, *Prog. Quantum Electron.* **2002**, *26*, 193.

[34] C. Gärtner, C. Karnutsch, U. Lemmer, C. Pflumm, *J. Appl. Phys*., **2007**, *101*, 023107.

[35] O. V. Mikhnenko, P. W. M. Blom, T.-Q. Nguyen, *Energy Environ. Sci.*, **2015**, *8*, 1867.

[36] E. J. W. List, U. Scherf, K. Mullen, W. Graupner, C.-H. Kim, J. Shinar, *Phys. Rev. B*, **2002**, *66*, 235203.

[37] J. N. Turro, V. Ramamurthy, J. C. Scaiano, *Modern Molecular Photochemistry of Organic Molecules*, University Science Books, 2010; pp.414-416.

[38] B. H. Wallikewitz, D. Kabra, S. G´elinas, R. H. Friend, *Phys. Rev. B*, **2012**, *85*, 045209.

[39] Y. Jiang, Y-Y. Liu, X. Liu, H. Lin, K. Gao, W-Y. Lai, W. Huang, *Chem. Soc. Rev.*, **2020**, *49*, 5885.

[40] M. Lehnhardt, T. Riedl, T. Weimann, W. Kowalsky, *Phys. Rev. B*, **2010**, *81*, 165206.

[41] Z. Zhao, O. Mhibik, T. Leang, S. Forget, S. Chénais, *Optics Express*, **2014**, *22*, 30092.

[42] M. Uchimura, Y. Watanabe, F. Araoka, J. Watanabe, H. Takezoe, G.-I. Konishi, *Adv. Mater*., **2010**, *22*, 4473.

[43] S. Varghese, S.-J. Yoon, S. Casado, R. C. Fischer, R. Wannemacher, S. Y. Park, J.Gierschner, *Adv. Opt. Mater*., **2014**, *2*, 542.

[44] T. Oyamada, C.-H. Chang, T.-C. Chao, F.-C. Fang, C.-C. Wu, K.-T. Wong, H. Sasabe, C. Adachi, *J. Phys. Chem. C*, **2007**, *111*, 108.

[45] T. Aimono, Y. Kawamura, K. Goushi, H. Yamamoto, H. Sasabe, C. Adachi, *Appl. Phys. Lett.*, **2005**, *86*, 071110.

[46] T. Rabe, K. Gerlach, T. Riedl, H. H. Johannes, W. Kowalsky, J. Niederhofer, W. Gries, J. Wang, T. Weimann, P. Hinze, F. Galbrecht, U. Scherf, *Appl. Phys. Lett.*, **2006**, *89*, 87.

[47] S. Schols, A. Kadashchuk, P. Heremans, A. Helfer, U. Scherf, *Chem. Phys. Chem.*, **2009**, *10*, 1071.

[48] V. T. N. Mai, V. Ahmad, M. Mamada, T. Fukunaga, A. Shukla, J. Sobus, G. Krishnan, E. G. Moore, G. G. Andersson, C. Adachi, E. B. Namdas, S. C. Lo, *Nat. Commun.*, **2020**, *11*, 5623.

[49] Y. Zhang, S. R. Forrest, *Phys. Rev. B - Condens. Matter Mater. Phys.*, **2011**, *84*, 241301.

[50] T. Matsushima, S. Yoshida, K. Inada, Y. Esaki, T. Fukunaga, H. Mieno, N. Nakamura, F. Bencheikh, M. R. Leyden, R. Komatsu, C. Qin, A. S. D. Sandanayaka, C. Adachi, *Adv. Funct. Mater.*, **2019**, *29*, 1807148.

[51] A. S. D. Sandanayaka, L. Zhao, D. Pitrat, J. C. Mulatier, T. Matsushima, C. Andraud, J. H. Kim, J.-C. Ribierre, C. Adachi, *Appl. Phys. Lett.*, **2016**, *108*, 223301.

[52] B. S. B. Karunathilaka, U. Balijapalli, C. A. M. Senevirathne, Y. Esaki, K. Goushi, T. Matsushima, A. S. D. Sandanayaka, C. Adachi, *Adv. Funct. Mater.*, **2020**, *30*, 2001078.

[53] O. G. Peterson, S. A. Tuccio, B. B. Snavely, *Appl. Phys. Lett.*, **1970**, *17*, 245.

[54] C. Strome Jr., S. A. Tuccio, *Opt. Commun*., **1971**, *4*, 58.

[55] R. Bornemann, U. Lemmer, E. Thiel, *Opt. Lett.* **2006**, *31*, 1669.

[56] M. Lehnhardt, T. Riedl, U. Scherf, T. Rabe, W. Kowalsky, *Org. Electron*., **2011**, *12*, 1346.

[57] H. Nakanotani, C. Adachi, S. Watanabe, R. Katoh, *Appl. Phys. Lett.*, **2007**, *90*, 4.

[58] A. S. D. Sandanayaka, K. Yoshida, M. Inoue, C. Qin, K. Goushi, J.-C. Ribierre, T. Matsushima, C. Adachi, *Adv. Opt. Mater.*, **2016**, *4*, 834.

[59] S. Chénais, S. Forget, *Polym. Int.*, **2012**, *61*, 390.

[60] Y. Fu, T. Zhai, *Front. Optoelectron.*, **2020**, *13*, 18.

[61] H. Kogelnik, C. V. Shank, *Appl. Phys. Lett*., **1971**, *18*, 152.

[62] C. Karnutsch, C. Pflumm, G. Heliotis, J. C. deMello, D. D. C. Bradley, J. Wang, T. Weimann, V. Haug, C. Gärtner, U. Lemmer, *Appl. Phys. Lett*., **2007**, *90*, 131104.

Chapter 2

Laser operation under long-pulse excitation in solution-processed organic gain medium: toward CW lasing in organic semiconductors

V. T. N. Mai, A. Shukla, **A. M. C. Senevirathne**, I. Allison, H. Lim, R. J. Lepage, S. K. M. McGregor, M. Wood, T. Matsushima, E. G. Moore, E. H. Krenske, A. S. D. Sandanayaka, C. Adachi, E. B. Namdas, S. C. Lo, *Adv. Opt. Mater*., **2020**, *8*, 2001234.

(Equally contributed with V. T. N. Mai and A. Shukla).

2.1 Introduction

CW photoexcitation has been difficult to use for most organic materials as the laser emission is ceased by the accumulation of triplets and thermal degradation[1–5]. This singlet exciton losses from triplet exciton absorption at a lasing wavelength can be circumvented by the proper design of the organic semiconductor laser dye molecules with negligible overlap between the lasing spectrum and the triplet absorption spectrum[6,7,8] followed by efficient device architectures to dissipate heat.

In contrast to thermally deposited organic semiconductor laser dyes, solution-processable organic semiconductors can be fabricated by using simple, fast, low-cost, and room-temperature processing techniques such as spin-coating, dip-coating, ink-jet printing, and blade-coating. These techniques are ideal for large-area laser manufacture and the commercialization of low-cost disposable lasers[9]. However, most of the reported solution-processable organic semiconductor materials are conjugated polymers[10-14] which sometimes introduce batch-to-batch variation in film thicknesses and morphologies and photophysical properties. Moreover, no works have been reported in qCW operation with conjugated polymers other than BN-PFO[2]. Therefore, it is important to study solution-processable small molecular organic semiconductor laser materials operating in qCW regime which offer high purity and easy synthesis routes.

In this regard, we found that fluorene-based molecules are a promising choice as fluorene is a relatively inexpensive molecule, which can easily be functionalized with solubilizing units. These molecules are usually solids even attached with alkyl chains in the 9, 9'-position. There have been an increasing number of reports with promising organic laser dyes, containing fluorene building blocks such as oligofluorenes[15], spirobifluorenes[16], ladder-type oligo(*p*-phenylene)s[17], starburst or star-shaped macromolecules[18], fluorene-based dendrimers[19], and polymers[20]. Among these, oligomer octafluorene was found to exhibit an extremely low amplified spontaneous emission (ASE) threshold[21]. These works have inspired us to develop this solution-processable fluorene based laser dye bis(*N*-carbazolylstyryl)-9,9-dihexylfluorene (BSFCz).

Moreover, with this laser dye, I succeeded in demonstrating a room temperature organic laser in the qCW regime with pulse widths of up to 10 ms with a simple and straightforward synthesis route. This was achieved by exact strategy that discussed in section 1.3.7.1 in chapter 1 under CW laser condition, which is by separating the emission spectrum from the triplet absorption spectrum at lasing wavelength as change of ISC rate and triplet lifetime is hard. That is, probability of triplet absorption will be lower than the probability of stimulated emission at BSFCz lasing wave length.

2.2 Experimental

All commercial reagents and chemicals were used as received unless otherwise noted. Tetrahydrofuran (THF), toluene, and *N*,*N*-dimethylformamide (DMF) were dried using a solvent purification system over molecular sieves before use. Dichloromethane (DCM) was dried with calcium hydride overnight and freshly distilled prior to use. Detail synthesis route is explained in section 2.3.1 and it was carried out by *V. T. N. Mai, Centre for Organic Photonics & Electronics, The University of Queensland, Australia.*

Material Synthesis

The synthetic route to the new BSFCz chromophore is outlined in Scheme 2.1. First, vinylphenylcarbazole building block **2** was prepared in two steps, commencing from a commercially available 4-fluorobenzaldehyde via a nucleophilic aromatic substitution reaction (89%), followed by Wittig reaction (62%). The *n*-hexyl solubilizing groups were attached to fluorene under basic conditions to give precursor **4** in an excellent yield of 95%. The inclusion of these solubilizing groups aimed to ensure high solubility of the target BSFCz in organic solvents to enable the formation of good-quality thin films via a solution-processing method. Bromination of **4** using bromine (in the presence of iodine catalyst) gave **5** in a 93% yield. Finally, BSFCz was accomplished in a moderate yield (43%) by treating **5** with **2** under a microwave-assisted palladium-catalyzed Heck cross-coupling condition. **BSFCz** was found to have high solubility in common organic solvents.

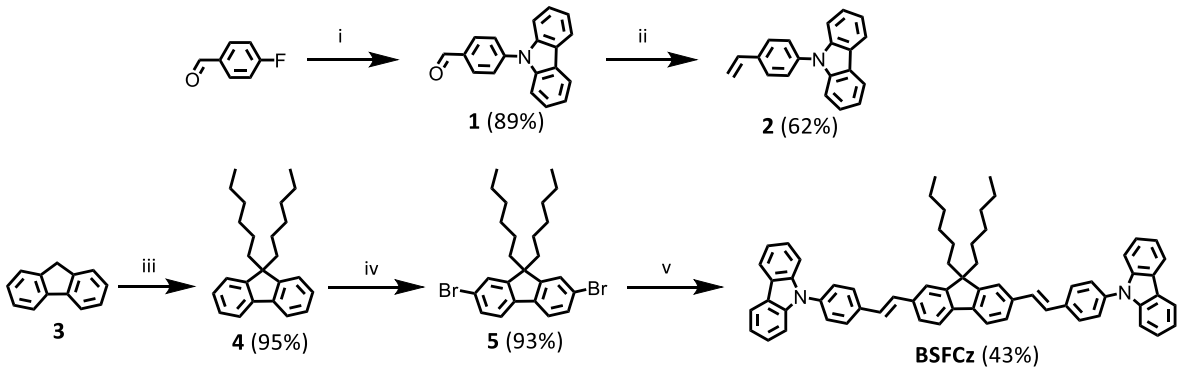

Scheme 2.1. Synthetic route to **BSFCz**: i) 9*H*-carbazole, K_2CO_3, DMF, $Ar_{(g)}$, 120 °C, 19 h; iia) Ph_3PCH_3I, *n*-BuLi, THF, $Ar_{(g)}$, 0 °C, 1 h. iib) **1**, THF, $Ar_{(g)}$, r.t., 19 h; iiia) *n*-BuLi, THF, $Ar_{(g)}$, −78 °C, 1 h. iiib) 1-Bromohexane, $Ar_{(g)}$, r.t., 16 h; iv) I_2(cat.), Br_2, DCM, $Ar_{(g)}$, r.t., 16 h; v) **2**, P(*o*-tol)$_3$, $Pd(OAc)_2$, NEt_3, THF, $Ar_{(g)}$, MW (200 W), 96 °C, 2 h.

Film Fabrication for ASE and Photophysical Measurements

Films were spin-coated from 25 mg mL^{-1} chloroform solutions at 2,500 rpm for 60 s onto fused silica substrates. Chloroform was freshly distilled prior to use. All substrates were cleaned by sonication in acetone and isopropanol, followed by UV-ozone treatment.

ASE Measurements

A randomly polarised nitrogen laser (Stanford Instruments) with an operating frequency of 20 Hz and 3.5 ns pulse width at 337 nm was used to excite the samples. Cylindrical lens and slit were used in order to obtain uniform spot size of 0.5 × 0.01 cm^2. A set of calibrated neutral density filters was used to control the excitation intensity. Samples were kept under vacuum (10^{-6} torr) to prevent air-induced degradation. Edge emission from the sample was collected using an optical fibre and the spectrometer (Hamamatsu, Mini-spectrometer TM series, C10083CA). Measurements were performed on at least three samples to confirm the reproducibility. This was carried out by *Atul Shukla, Centre for Organic Photonics & Electronics, The University of Queensland, Australia.*

Transient Absorption Spectroscopy (TAS) Measurements

Nanosecond TAS measurements were performed in toluene solution (optical density of approximately 0.2 at 370 nm) using EOS transient absorption spectrometer (Ultrafast Systems, LLC). An amplified laser system (Spitfire ACE, Spectra Physics) with an operating frequency of 1 kHz delivering ≈100 fs laser pulses at 800 nm was used to seed an optical parametric amplifier (TOPAS, Light Conversion) to generate an excitation 'pump' wavelength of 370 nm. A white light continuum from ≈380 to 900 nm was generated as the 'probe' pulse using a pulsed Nd:YAG based Leukos-STM super continuum light source, the timing of which was controlled electronically using the sync out of the amplified laser system. The instrument response function (IRF) for this setup dictated by the electronic timing resolution was ≈100 ps. This was carried out by *Atul Shukla, Centre for Organic Photonics & Electronics, The University of Queensland, Australia.*

DFB Laser Device Fabrications

Glass substrates (Atsugi Micro Co.) were cleaned by ultrasonication using neutral detergent, pure water, acetone, and isopropanol followed by UV-ozone treatment. A 100 nm thick layer of SiO_2, which would become the DFB grating, was sputtered onto the glass substrates heated at 100 °C. The argon pressure during the sputtering was 0.66 Pa. The RF power was set at 100 W.

The SiO_2 surfaces were treated with hexamethyldisilazane (HMDS) by spin coating at 4,000 rpm for 15 s and annealed at 120 °C for 120 s. A resist layer with a thickness of around 70 nm was spin-coated on the substrates at 4,000 rpm for 30 s from a ZEP520A-7 solution (ZEON Co.) and baked at 180 °C for 240 s.

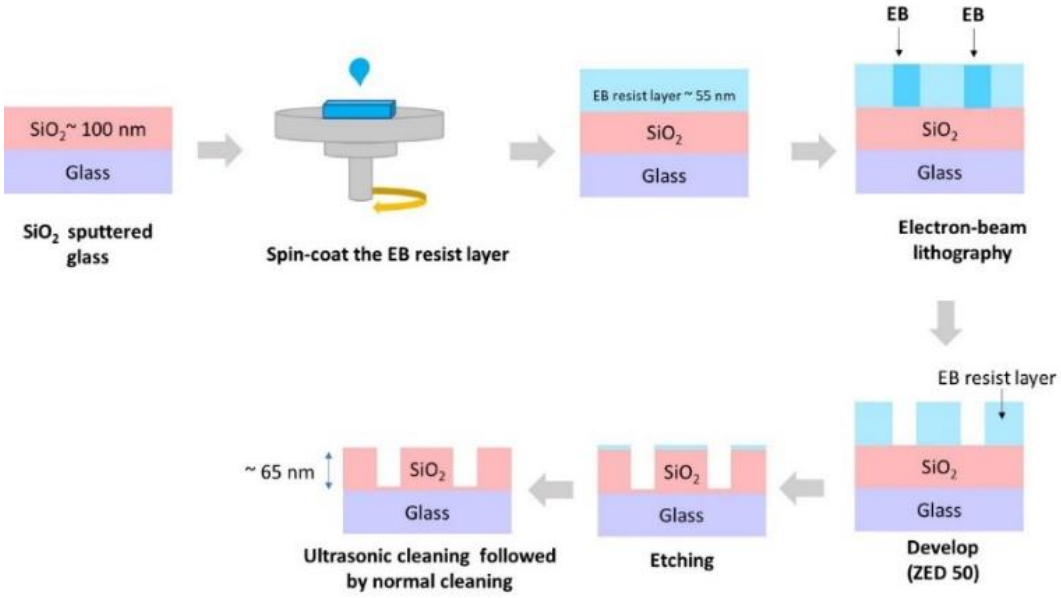

Figure 2.1. Fabrication flow of a DFB structure on substrates.

Then, electron beam lithography was performed to draw grating patterns on the resist layer using a JBX-5500SC system (JEOL) with an optimized dose of 0.1 nC cm^{-2}. After the electron beam irradiation, the patterns were developed in a developer solution (ZED-N50, ZEON Co.) at room temperature. The patterned resist layer was used as an etching mask. The substrate was plasma etched with CHF_3 using an EIS-200ERT etching system (ELIONIX). To completely remove the resist layer from the substrate, the substrate was plasma-etched with O_2 using a FA-1EA etching system (SAMCO). The gratings formed on the SiO_2 surfaces were observed with a scanning electron microscope (SEM) (SU8000, Hitachi). The grating fabrication flow is shown below in Figure 2.1.

To complete the laser devices, BSFCz was blended with 4,4',4"-Tris(carbazol-9-yl)-triphenylamine (TCTA) and 6 wt % BSFCZ:TCTA blend film (200 nm) was prepared on the gratings by spin-coating at 2,500 rpm for 60 s. To seal the organic laser devices, the substrates were encapsulated (in a nitrogen-filled glove box) with optically transparent fluoropolymer

CYTOP (refractive index = 1.35, Asahi Glass Co. LTD.) and thermally conductive sapphire lids (approximately 25 W mK^{-1} at 300 K). The devices were dried under vacuum for 12 hours. These CYTOP and sapphire lids demonstrate good transparency at the lasing wavelengths. The schematic diagram of the organic DFB laser device structure is shown in Figure 2.2.

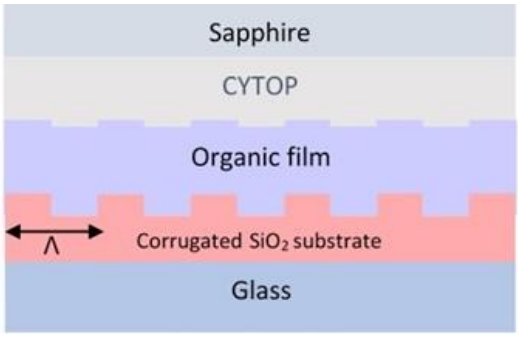

Figure 2.2. Schematic of the DFB laser device structure.

Laser Characterization under Short-Pulse Photoexcitation

For the characterization of the organic lasers, pulsed excitation light from a nitrogen laser (SRS, NL-100) was focused on a 6.5×10^{-3} cm^2 area of the devices through a lens and slit. The excitation wavelength was 337 nm, pulse width was 3.5 ns, and repetition rate was 20 Hz. The excitation light was incident upon the devices at around 20° with respect to the normal to the device plane. The emitted light was collected normal to the device surface with an optical fiber connected to a multichannel spectrometer (PMA-50, Hamamatsu Photonics) and placed 3 cm away from the device. Excitation intensities were controlled using a set of neutral density filters (motorised filter wheel FW102C). The size of the excitation area was carefully checked by using a beam profiler (WimCamD-LCM, DataRay).

Laser Characterization under qCW-Photoexcitation

For the qCW operation, a CW laser diode (NICHIYA, NDV7375E, maximum power of 1,400 mW) was used to generate excitation light with an excitation wavelength of 405 nm. In these measurements, pulses were delivered using an acousto-optic modulator (AOM, Gooch & Housego), which was triggered with a pulse generator (WF 1974, NF Co.). The excitation light was focused on a 8.76×10^{-6} cm^2 area of the devices through a lens and a slit, and the emitted light was collected using a multichannel spectrometer (PMA-50, Hamamatsu Photonics) or streak scope (C7700, Hamamatsu Photonics) with a time resolution of 100 ps that was connected with a digital camera (C9300, Hamamatsu Photonics). The emission intensity was recorded using a photomultiplier tube (PMT) (C9525-02, Hamamatsu Photonics). Both the PMT response and the driving square wave signal were monitored on a multi-channel oscilloscope (Agilent Technologies, MSO6104A). The same irradiation and detection angles were used for this measurement as described earlier. All the measurements were performed in nitrogen atmosphere to prevent any degradation resulting from moisture and oxygen. The size of the excitation area was carefully checked by using a dual scanning slit beam profiler (BP209-VIS). For the far-field emission profile measurement, a C9664-01G02 Hamamatsu photonics charged couple device (CCD) camera was used, with a distance between the sample and the camera being kept at 1 cm.

2.3 Results and discussion

2.3.1 Material characterization

Thermal properties of the chromophore were studied by using thermogravimetric analysis (TGA) and differential scanning calorimetry (DSC) under a nitrogen atmosphere and exhibited excellent thermal stability with a decomposition temperature, corresponding to 5% weight loss at 436 °C as shown in Figure 2.3 (a) and glass transition temperature (T_g) at 105 ^oC as shown in Figure 2.3 (b).

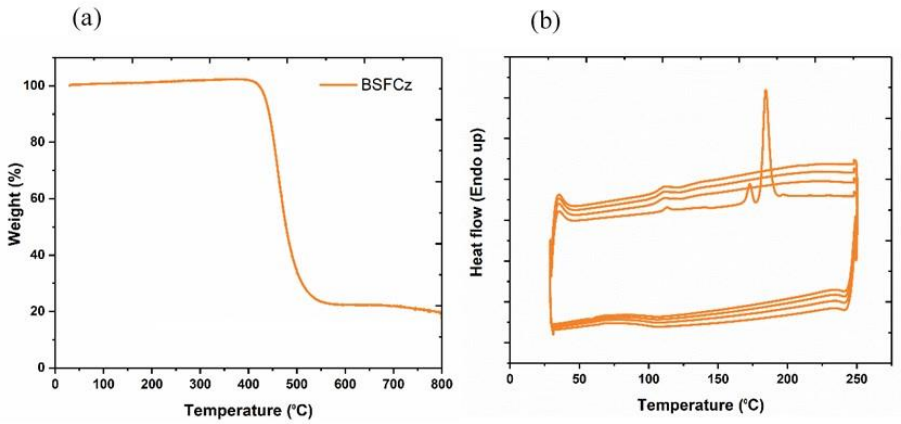

Figure 2.3. (a) TGA thermogram of BSFCz with a heating rate of 10 °C min^{-1} under nitrogen, showing a decomposition temperature of 436 °C, corresponding to a 5% weight loss. (b) DSC traces of BSFCz. Scan rate = 100 °C min^{-1}. All four heating/cooling cycles showed that it has a glass transition temperatures (T_g) at ~105 °C.

2.3.2 Photophysical properties

Photophysical properties of BSFCz were studied in solution (toluene), blend [6 wt % in TCTA], and neat films. The film samples were spin-coated from chloroform solution. Figure 2.4 (a) depicts the steady-state absorption and PL spectra of solution and films. The corresponding data are summarized in Table 2.1. A high molar extinction coefficient (ε) of 1.06×10^5 dm^3 mol^{-1} cm^{-1} (at 387 nm) was found for BSFCz as shown in Figure 2.4 (b), which is attributed to its extended π-conjugation.

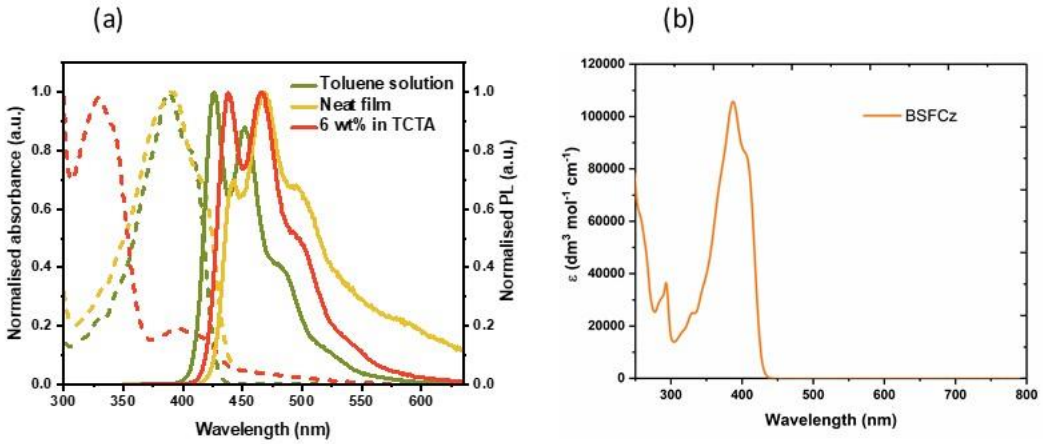

Figure 2.4. (a) Normalised UV-Vis absorption (dash lines) and PL (photoluminescence) spectra (solid lines) of solution (in toluene, green line), blend films (6 wt % in TCTA, red line), and neat films (brown line) of BSFCz. Excitation wavelengths were 350 nm for solution and 325 nm for films. All films were spin-coated from chloroform solution. (b) Solution absorption spectrum of BSFCz in dichloromethane, showing the high molar extinction coefficient.

Table 2.1. Photophysical properties of BSFCz in toluene solution and blend (6 wt % in TCTA) and neat films spin-coated from chloroform solution. *Average PL lifetime.

BSFCz	λ_{abs} (nm) [ε, dm^3 mol^{-1} cm^{-1}]	λ_{PL} (nm)	PLQY (%)	PL lifetime (ns)	k_r (× 10^8 s^{-1})
Solution	387 [1.06 × 10^5]	426	85±4	0.86	9.9
Blend film	330	465	76±4	0.81*	9.4
Neat film	390	468	31±9	0.61	5.1

The PL of BSFCz solution exhibited the distinctive vibronic emission structures, suggesting minimal rotational freedom of the molecule, with the 0-0 vibronic transition peak at 426 nm (Figure 2.4 (a)). A high PLQY of 85 ± 4% was found for BSFCz solution in toluene. Moving from solution to neat solid-state films, a redshift in both the absorption and PL was observed (Figure 2.4 (a)). Coupled with the broadened spectra, this indicates stronger intermolecular interactions in a solid state. Therefore, it is not unexpected that the PLQY decreased to 31 ±

9% for neat films because of the concentration quenching of PL. This was further supported by time-correlated single-photon counting (TCSPC) measurements to show the reduced PL lifetime in the neat film (0.61 ns) compared to that (0.86 ns) in solution (Table 2.1). Photophysical studies of blended films (6 wt % in TCTA) also showed the redshifted PL spectrum, compared to solution measurements (Figure 2.1 (a)). The redshifted PL is an indication of minor aggregation emission, which should be circumvented by further reducing the doping percentage. Interestingly, our concentration-dependent studies of BSFCz blend films (at 4, 6, 8, and 10 wt % in TCTA) did not show any considerable changes in the PL spectra, as shown in Figure 2.5. However, the PLQY of blended films was comparable to that of a dilute solution (Table 2.1), suggesting the aggregates have the minimal contribution of the concentration quenching effect. The radiative decay rates (k_r) were calculated based on the PLQY and PL lifetime data. This gave a high k_r value of 9.9×10^8 s^{-1} for BSFCz in toluene. Moving from solution to neat films, the k_r value reduced by about 50%. However, by blending the BSFCz in a TCTA host film, the k_r value was significantly reinstated, approaching its solution value (Table 2.1).

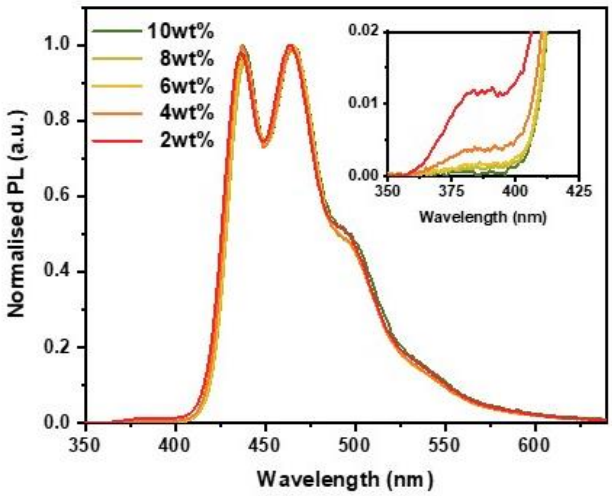

Figure 2.5: Normalised blend-film PL spectra of BSFCz at different doping concentrations (2 wt %, 4 wt %, 6 wt %, 8 wt %, and 10 wt %) in TCTA. Inset showing a reduction in PL from TCTA with an increase in doping concentration of BSFCz. The excitation wavelength was 325 nm.

2.3.3 ASE properties

Solid-state ASE studies of neat and blended films were conducted to evaluate the laser performance as a gain material. All films were spin-coated from chloroform solution. The ASE thresholds were estimated from an abrupt change in slope of input-output intensity and the estimated ASE threshold (E_{th}) values are summarised in Table 2.2. The ASE threshold of BSFCz neat films was 4.4 μJ cm^{-2}. Blend films of BSFCz with various blend ratios in TCTA were further studied to optimize ASE performance, and 6 wt % BSFCz-doped TCTA films had the lowest ASE E_{th} values of 1.1 μJ cm^{-2} (Table 2.2), which is comparable to those of current state-of-the-art organic laser dyes[16, 21-24]. The observed ASE occurred at the 0-1 vibration for both neat and blend films (Figure 2.6 and Figure 2.7), which is common for organic laser dyes, and this can be explained by the presence of an efficient quasi-four energy level system for the transition.

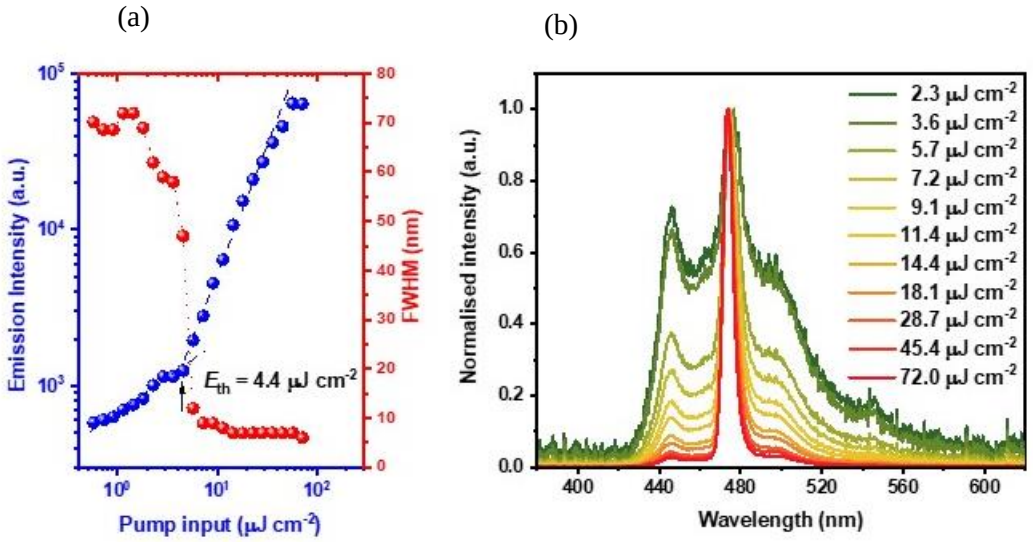

Figure 2.6: ASE behaviors of BSFCz neat films. (a) ASE thresholds graph and (b) PL spectra measured at excitation intensities bellow and above the ASE threshold. PL spectral narrowing occurred with increasing pump inputs.

Table 2.2: Solid-state ASE E_{th} (μJ cm^{-2}) of BSFCz neat and blend (in TCTA with various blend ratio) films.

	Neat film	Blend film (in TCTA)				
		2 wt%	4 wt%	6 wt%	8 wt%	10 wt%
ASE E_{th} (μJ cm^{-2})	4.4	1.7	1.6	1.1	1.2	1.1

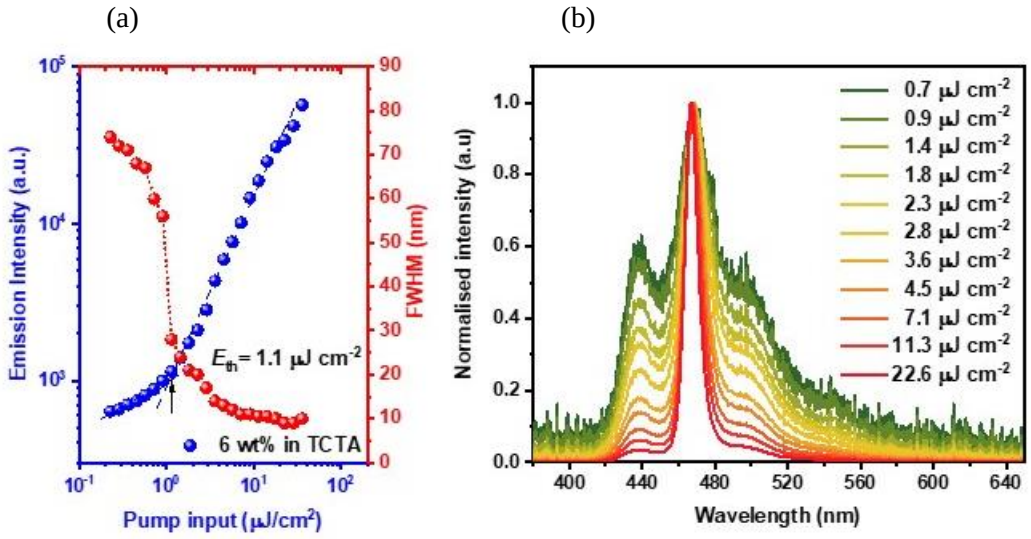

Figure 2.7: ASE behaviors of BSFCz blend films using TCTA as the host. (a) ASE threshold graph and (b) PL spectra measured at excitation intensities bellow and above the ASE threshold. PL spectral narrowing occurred with increasing pump inputs.

2.3.4 Lasing under short-pulse photoexcitation

Laser studies of BSFCz were carried out by incorporating a second-order DFB resonator structure, which gives a vertically out coupled beam via first-order diffraction and feedback via second-order diffraction[25, 26]. The calculated period value for the second-order (m = 2) grating was 276 nm at the Bragg wavelength of 470 nm, using refractive index (n) of the film as 1.7. The SEM image of the fabricated second-order DFB is shown in Figure 2.8 and it is in accordance with calculated period values.

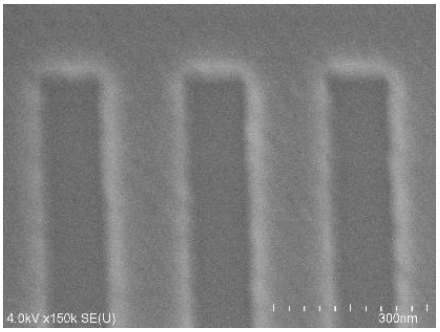

Figure 2.8. SEM image of the fabricated second-order DFB structure.

Then the laser device was assembled by spin coating 6 wt % BSFCz in TCTA using chloroform solution (thickness ~200 nm) on top of the DFB structure, followed by encapsulating with CYTOP and a sapphire substrate as explained in the experimental section. Then lasing properties were examined *via* optical pulse excitation using a nitrogen laser (pulse width 3.5 ns, repetition rate 20 Hz). The surface-emission lasing profile with the second-order DFB resonator structure is shown in Figures 2.9 (a), along with full width at half maximum (FWHM) reducing to 0.5 nm above the lasing threshold in the inset. However, there was a ~ 10 nm wavelength shift of the emitted laser beam from the Bragg wavelength of 470 nm. That is, emission was appeared around 461 nm as shown in the inset of Figure 2.9 (a). After treating n numerically to find n_{eff} as shown in literature[27], n_{eff} value was found to be 1.67. According to Bragg's law, the laser emission wavelength is given by $\Lambda \times n_{eff}$. Then the calculated laser emission wavelength was found to be ~ 461 nm (i.e 276 nm × 1.67 = 461 nm). Hence it was confirmed, that the spectral shift of 10 nm was due to the difference of n and n_{eff} values. The lasing threshold of the spin-coated BSFCz (6 wt % in TCTA) with the second-order DFB resonator structure was estimated to be 0.9 μJ cm^{-2} (≈260 W cm^{-2}) as depicted in Figure 2.9 (b), which is slightly lower than its ASE threshold of 1.1 μJ cm^{-2}.

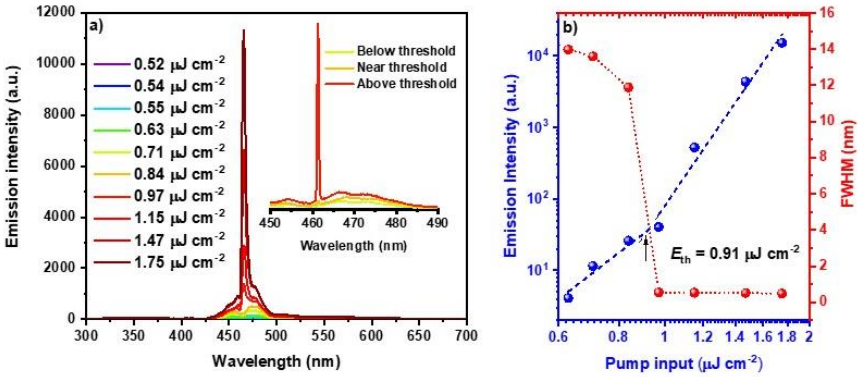

Figure 2.9: a) Laser emission profiles of second-order DFB laser devices based on a BSFCz:TCTA (6:94 wt %) film under pulsed excitation. The inset shows the high-resolution spectra below, near, and above the lasing threshold. b) Laser output intensity and FWHM as a function of pumping input in second-order DFB lasers.

2.3.5 Transient absorption spectroscopy (TAS) measurements

A laser material should have a positive gain in the lasing window without any losses arising from the excited state absorptions from singlets or triplets as discussed in chapter 1 in section1.3.3.1. Moreover, singlet excited state lifetime lies in nano seconds. Triplet lifetime lies in micro-second to milli-second range. That is, singlet lifetime is very short compared to triplet lifetime. When a laser device is excited under CW photoexcitation, singlet state is continuously filling. Meantime, triplet state is accumulating. That is, there is a chance to deplete these pumped singlet excitons via excited state singlet absorption and excited state triplet absorption. As a result, the laser will not achieve stimulated emission condition and it will quickly shut down the laser action. Therefore, it is crucial to investigate both singlet and triplet excited state absorption spectra in CW lasing. Further, these spectra happen to be broad due to many absorptions occur to higher lying excited states from first excited state of both singlets and triplets.

In addition, most of the laser materials show moderate to high PLQY. That is, generated singlet state exciton density is much higher than triplet state exciton density in photoexcitation. Because triplets are formed via ISC from the singlet state. As a result,

measured excited state singlet absorption is comparatively stronger than excited state triplet absorption.

To understand this optical loss mechanism and dynamics of singlet and triplet excited-states, nanosecond TAS measurements were performed in BSFCz solution (toluene). Long and short-lived absorption features were observed in the log-log plot as shown in Figure 2.10 (a). The short-lived excited-state absorption and emission features (with negative differential absorption) were found to have a decay lifetime (0.83 ns), which is similar to the emission lifetime (0.86 ns) obtained from the TCSPC measurements. Hence, these short-lived absorption features are attributed to singlet excited-state absorption, while the long-lived features (0.13 µs, see Figure 2.10 (a)) are attributed to triplet excited-state absorption. These singlet and triplet excited-state absorption features, along with ASE and DFB laser emission for 6 wt % BSFCz doped in TCTA are depicted in Figure 2.10 (b), showing negligible triplet absorption in the gain region, which provides an excellent platform for long-pulse operation study.

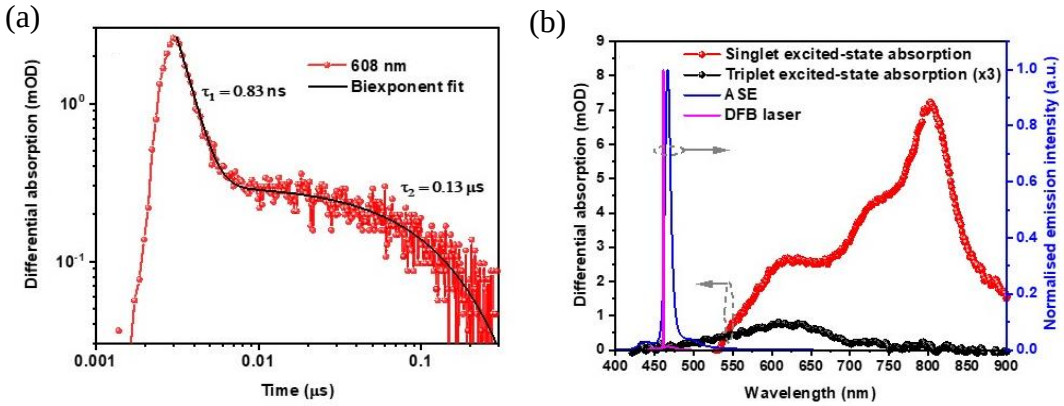

Figure 2.10. a) Transient absorption kinetics measured at triplet absorption peak (608 nm) and bi-exponential fit corresponding to singlet and triplet lifetimes for BSFCz in toluene. b) ASE (blue), DFB laser (pink), singlet excited-state absorption (3.1 ns delay, red line), and triplet excited-sate absorption (10.2 ns delay, magnified by 3 times, black line) spectra of BSFCz in toluene solution, showing essentially no excited-state absorption at the ASE wavelength.

2.3.6 Lasing under qCW photoexcitation

Laser characteristics of second-order DFB devices using a blend film of BSFCz (6 wt % in TCTA) were investigated with qCW photoexcitation as explained in the experimental section using a CW excitation source of an inorganic laser diode operating at 405 nm with a maximum power of 1,400 mW. This excitation pulse width is much longer compared to the previous short pulse (3.5 ns) photoexcitation. Under qCW photoexcitation, the pulse width was varied from 10 μs to 10 ms.

Figure 2.11 shows the laser behaviour obtained for the DFB BSFCz blend films at 10 ms of photoexcitation. Lasing thresholds were estimated from the abrupt change in the slope of the emission intensity *versus* excitation intensity graph, which was further supported by the reduction of FWHM to below 2 nm at excitation intensities above the lasing E_{th}. The lasing threshold at 10 ms qCW photoexcitation was estimated to be 420 W cm^{-2}.

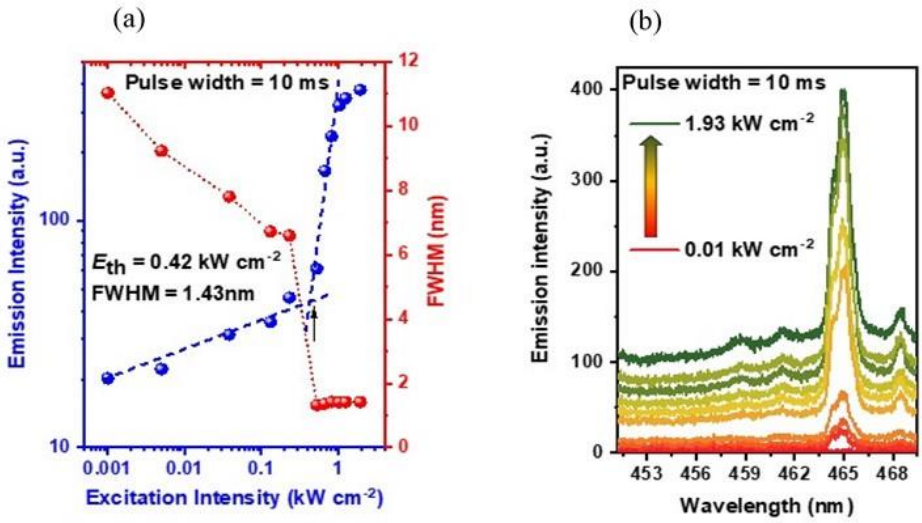

Figure 2.11: a) Laser output intensity and FWHM as a function of excitation intensity in case of using 10 ms CW photoexcitation pulses and b) laser emission profiles measured under 10-ms-width pulse photoexcitation.

Table 2.3 shows the summary of the lasing thresholds under qCW photoexcitation from 10 µs to 10 ms. A slight increment of the lasing threshold can be observed when increasing the pulse width. This is probably due to the molecular degradation of the laser device because of the prolonged exposure to the intense photoexcitation. Moreover, the lasing thresholds under qCW photoexcitation were higher than that shown in Section 2.3.4 for the nanosecond pulsed operation as expected.

Table 2.3. Lasing thresholds in DFB laser devices of BSFCz blend films (6 wt % in TCTA) as a function of pulse width under qCW operation.

Pulse width (µs)	Lasing threshold (W cm^{-2})
10	300
100	330
1,000	400
10,000	420

To confirm the lasing action, I carried out temporal emission profiles of DFB lasers using a streak camera system with a maximum temporal limit of up to 1 ms. Figure 2.12 (a) and (b) show streak camera images taken above and below the lasing threshold at different excitation pulse widths claiming the laser emission under qCW photoexcitation. At 100 µs pulse width [Figure 2.12 (i)], it can be clearly seen a weak laser emission appeared below the lasing threshold, and a more intense narrowed laser emission appeared above the lasing threshold inside the 1 ms time frame. In Figure 2.12 (ii), the laser emission above the lasing threshold is appeared more longer, indicating 500 µs long laser emission from our laser device. In Figure 2.12 (iii), part of the very long laser emission of 10 ms is captured within 1 ms time frame claiming the laser emission in 10 ms qCW photoexcitation

.

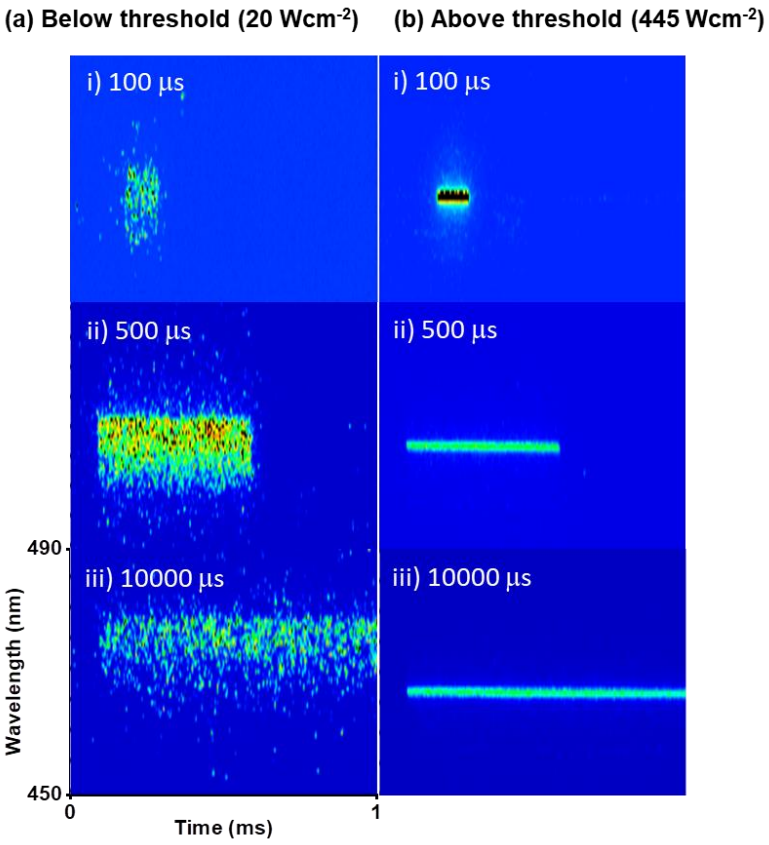

Figure 2.12: Streak camera images showing temporal emission profiles integrated over 100 pulses from the encapsulated DFB devices operating at intensities (**a**) below and (**b**) above lasing E_{th} for different photoexcitation pulse widths.

To further investigate the existence of STA under qCW photoexcitation, a temporal profile of the laser emission was investigated under 10 µs pulse width, as shown in Figure 2.13. During this pulse width, the emission profile above the lasing threshold was not decayed. This clearly confirms that STA is not involved in the BSFCz based laser devices due to the spectral separation of triplet absorption and laser emission spectra. This is one reason that the laser device even could operate up to 10 ms which is much longer than the triplet lifetime (0.13 µs) of BSFCz.

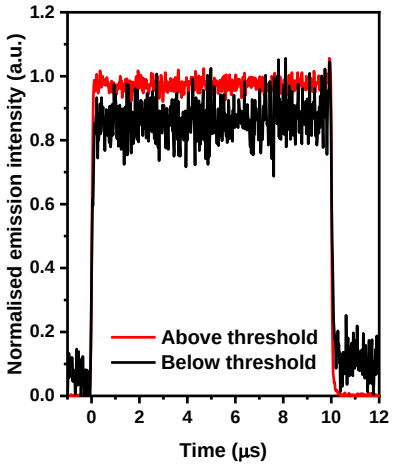

Figure 2.13. Temporal evolution of the lasing output intensity of BSFCz blend films (6 wt % in TCTA) at before and after lasing threshold under the photoexcitation of 10 μs pulse width.

2.3.7 Laser confirmation studies

Confirmation of the laser behaviours was further investigated by polarisation. Figure 2.14 shows the polarisation of the emitted laser beam under 10 ms pulsed photoexcitation, suggesting that the output laser beam is linearly polarised along the grooves of the DFB grating

.

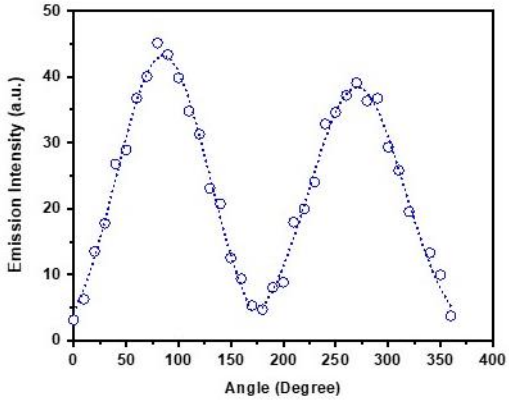

Figure 2.14. Emission intensity from a BSFCz based DFB device as a function of polarization angle. The photoexcitation width was 10 ms, and the excitation intensity was ≈ 550 W cm^{-2}.

The far-field interference pattern was obtained to claim the spatial coherence of the emitted laser beam. The resulting far-field interference cross-section obtained from the sample showed the rise in the first-order diffraction as the excitation power increased from the near-threshold to the above threshold, as shown in the green circle in Figure 2.15 (a). This gives evidence about the spatial coherence of the resulting laser beam which directly correlates with the laser beam quality.

(a)

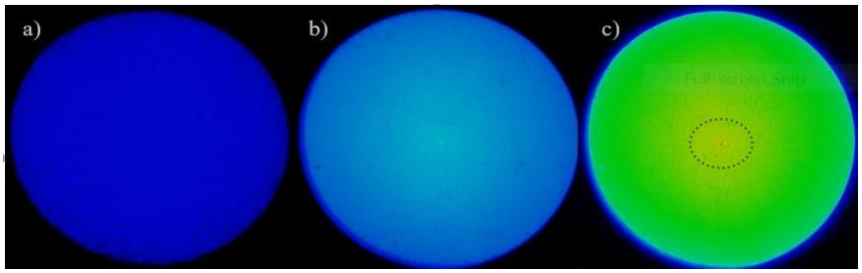

(b)

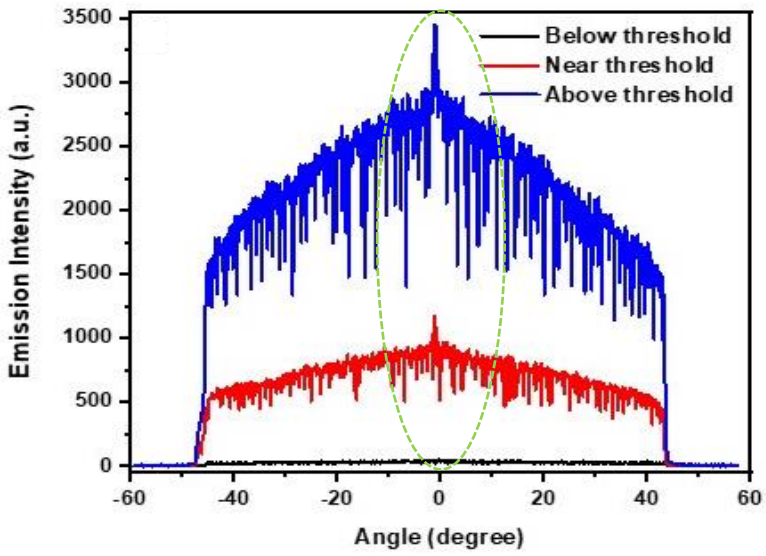

Figure 2.15. (a) Far-field beam images at excitation power intensities below, near, and above the lasing threshold for BSFCz blend films (6 wt % in TCTA), with the green dotted circle highlighting the amplified emission laser peak and (b) corresponding emission spectra of far-field images.

2.3.8 qCW Laser emission stability

Thermal instability of organic laser compounds under intense excitation intensities above lasing thresholds has been the biggest factor for the termination of lasing emission at longer excitation pulse widths. Here, I studied the stability of laser devices with a 6 wt % BSFCz blend film at a peak excitation intensity of 1.97 kW cm^{-2} and a pulse width of 10 ms. As shown in Figure 2.16, the half-life, which takes initial laser intensity to reach its half of laser intensity from the DFB device, was ~13 min. Despite the fact that the encapsulation of laser devices with a high-thermal conductive sapphire lid has led to much improved stability of laser output in qCW regime (in BSBCz:CBP laser operation time could enhance from 0.8 ms to 30 ms by introducing sapphire and CYTOP encapsulation)[8], further improvement is still needed in order to extend the scope to true CW lasing emission.

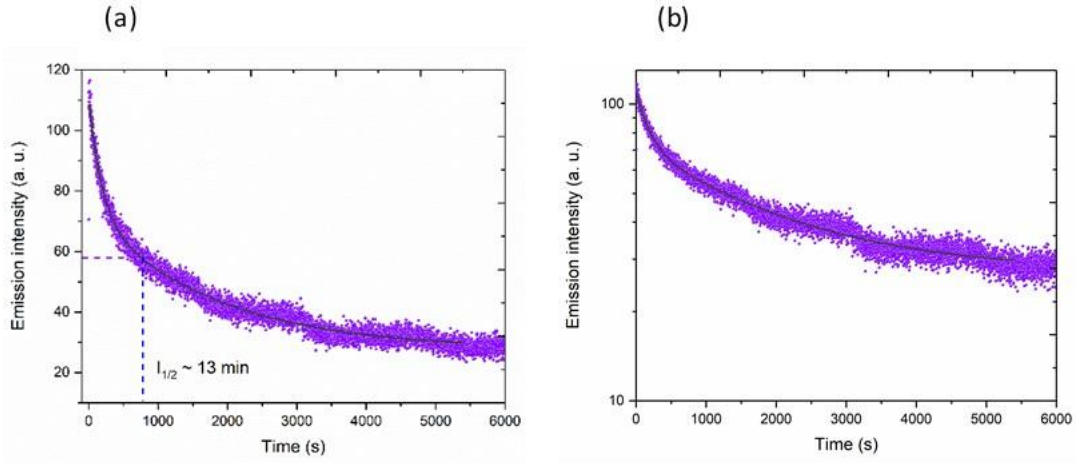

Figure 2.16. (a) Stability of qCW laser emission from laser devices based on a 6 wt % BSFCz blend film under 10 ms photoexcitation. The excitation intensity was 1.97 kW cm^{-2} and (b) stability measurement of BSFCz fitted with biexponential function.

To get an idea about the decay mechanism, single logarithmic plot was fitted using a biexponential function as shown in Figure 2.16 (b) above. As the graph could be fitted with biexponential decay function, there should be at least two definite decomposition paths. Calculated first decay lifetimes is 3 min and second decay lifetime is 30 min. That implies

one degradation path takes place very quickly from very unstable site of the molecule and then proceed to a second degradation path via stable fragment compared to the first. To get more insight of the degradation, here I depicted the change of lasing spectra with time measured at high resolution as shown in Figure 2.17 below.

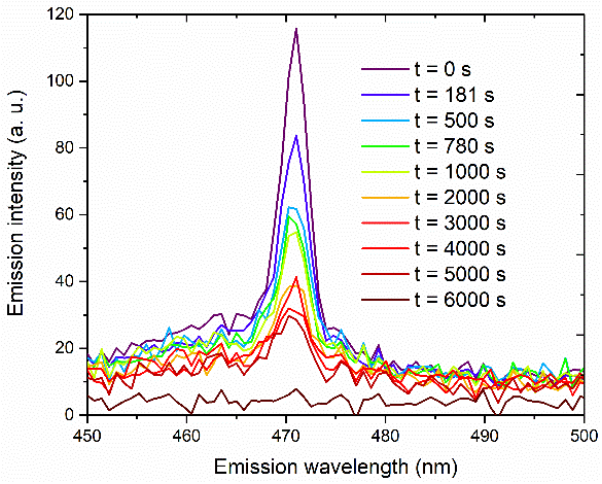

Figure 2.17. Lasing profiles with time at excitation intensity of 1.97 kW cm^{-2}.

From Figure 2.17, it can be clearly seen that within 181 s (~ 3 min), rapid degradation occurs. This can be attributed to the dissociation of the weak C-N bonds of the carbazole unit of BSFCz. This was confirmed by a degradation mechanism study conducted with BSBCz by Matsushima et al.[28]. However, the second degradation occurs slowly compared to the first degradation. This might proceed via the dissociation of the weak π bonds of the BSFCz[28].

Table 2. Comparison of CW laser stability

Laser system	CW performance	Stability
BN-PFO (Rabe *et al., Appl. Phys. Lett*., 2006, 89,081115)	5 MHz	Stability was not reported
Alq_3:DCM2:ADN (Y. Zhang *et al., Phys. Rev. B*, 2011, 84, 241301)	100 µs	Stability was not reported
Heptafluorene:EHCz (A. S. D. Sandanayaka *et al., Appl. Phys. Lett.,* 2016*,* 108*,* 223301*)*	4 MHz	10% reduction within 5 min (at 1 MHz, power 2.5 µJ cm^{-2})
BSBCz:CBP (A. S. D. Sandanayaka *et al., Sci. Adv.,* 2017**,** 3, e1602570)	30 ms	500 pulses at 2 kW cm^{-2}
DCNP:BSBCz (B. S. B Karunathilaka *et al., Adv. Funct. Mater*., 2020, 30, 2001078)	True CW	Half-life (LT_{50}) with in 3.15 min

When looking at these reported results, it is difficult to compare the results of BSFCz stability directly to literature values as the lasing conditions in reported works were measured and reported in many different ways. However, as can be seen in Figure 2.17, laser emission could be observed at least up to ~ 17 min even with reduced lasing intensity. Therefore, conclusion can be made as BSFCz shows a better qCW laser stability.

2.4 Conclusion

Lasing action under qCW photoexcitation with pulse widths of up to 10 ms from a new solution-processable organic semiconductor laser dye BSFCz was successfully demonstrated for the first time. The extended π-conjugation of BSFCz significantly enhances its molar extinction coefficient and radiative decay rate, coupled with shortened excited-state lifetimes to contribute to excellent solid-state ASE thresholds (1.1 µJ cm^{-2}) from spin-coated blend films (in TCTA host matrix). The low ASE threshold values are comparable to current state-of-the-art organic laser dyes reported to date. The surface-emitting second-order DFB lasers based on a BSFCz blend film also showed outstanding performance, with the lasing threshold of only 0.9 µJ cm^{-2} under nanosecond pulsed photoexcitation. TAS measurements showed

that BSFCz has a negligible triplet absorption overlapping with the ASE and lasing spectra. The temporal evolution of laser emission under 10 μs excitation pulse confirmed insignificant singlet quenching like STA, which further helps in achieving laser emission from DFB devices with photoexcitation pulse widths of 10 ms. The DFB lasing presented in this study was confirmed by polarisation, streak camera images, as well as far-field interference.

References

[1] R. Bornemann, U. Lemmer, E. Thiel, *Opt. Lett.* **2006**, *31*, 1669

[2] T. Rabe, K. Gerlach, T. Riedl, H. H. Johannes, W. Kowalsky, J. Niederhofer, W. Gries, J. Wang, T. Weimann, P. Hinze, F. Galbrecht, U. Scherf, *Appl. Phys. Lett.*, **2006**, *89*, 87–90.

[3] Z. Zhao, O. Mhibik, T. Leang, S. Forget, S. Chénais, *Opt. Express*, **2014**, *22*, 30092.

[4] Y. Zhang, S. R. Forrest, *Phys. Rev. B - Condens. Matter Mater. Phys.*, **2011**, *84*, 241301.

[5] A. S. D. Sandanayaka, K. Yoshida, M. Inoue, C. Qin, K. Goushi, J-C. Ribierre, T. Matsushima, C. Adachi, *Adv. Opt. Mater.*, **2016**, *4*, 834.

[6] M. Lehnhardt, T. Riedl, T. Weimann, W. Kowalsky, *Phys. Rev. B*, **2010**, *81*, 165206.

[7] T. G. Pavlopoulos, *Prog. Quantum Electron.* **2002**, *26*, 193.

[8] A. S. D. Sandanayaka, T. Matsushima, F. Bencheikh, K. Yoshida, M. Inoue, T. Fujihara, K. Goushi, J.-C. Ribierre, C. Adachi, *Sci. Adv.* **2017**, *3*, e1602570.

[9] O. Mhibik, S. Chénais, S. Forget, C. Defranoux, S. Sanaur, *J. Appl. Phys.*, **2016**, *119*, 173101.

[10] G. Heliotis, R. Xia, D. D. C. Bradley, G. A. Turnbull, I. D. W. Samuel, P. Andrew, W. L. Barnes, W. L. *Appl. Phys. Lett.*, **2003**, *83*, 2118.

[11] G. Heliotis, D. D. C. Bradley, G. A. Turnbull, I. D. W. Samuel, *Appl. Phys. Lett.*, **2002**, *81*, 415.

[12] R. D. Xia, G. Heliotis, D. D. C. Bradley, *Appl. Phys. Lett.*, **2003**, *82*, 3599.

[13] M. Theander, T. Granlund, D. M. Johanson, A. Ruseckas, V. Sundstrom, M. R. Andersson, O. Inganas, O. *Adv. Mater.*, **2001**, *13*, 323.

[14] M. N. Shkunov, R. Osterbacka, A. Fujii, K. Yoshino, Z. V. Vardeny, *Appl. Phys. Lett.*, **1999**, *74*, 1648.

[15] K. Kazlauskas, G. Kreiza, O. Bobrovas, O. Adomėnienė, P. Adomėnas, V. Jankauskas, S. Juršėnas, *Appl. Phys. Lett.*, **2015**, *107*, 043301.

[16] H. Nakanotani, S. Akiyama, D. Ohnishi, M. Moriwake, M. Yahiro, T. Yoshihara, S. Tobita, C. Adachi, *Adv. Funct. Mater.*, **2007**, *17*, 2328.

[17] M. Fang, J. Huang, S. J. Chang, Y. Jiang, W.-Y. Lai, W. Huang, *J. Mater. Chem. C*, **2017**, *5*, 5797.

[18] A.L. Kanibolotsky, N. Laurand, M. D. Dawson, G. A. Turnbull, I. D. W. Samuel, P. J. Skabara, *Acc. Chem. Res.*, **2019**, *52*, 1665.

[19] J. C. Ribierre, G. Tsiminis, S. Richardson, G. A. Turnbull, I. D. W. Samuel, *Appl. Phys. Lett.*, **2007**, *91*, 081108.

[20] J. Y. Li, F. Laquai, G. Wegner, *Chem. Phys. Lett.*, **2009**, *478*, 37.

[21] D. H. Kim, A. S. D. Sandanayaka, L. Zhao, D. Pitrat, J. C. Mulatier, T. Matsushima, C. Andraud, J.-C. Ribierre, C. Adachi, *Appl. Phys. Lett.*, **2017**, *110*, 023303.

[22] M. Mamada, T. Fukunaga, F. Bencheikh, A. S. D. Sandanayaka, C. Adachi, *Adv. Funct. Mater.*, **2018**, *28*, 1802130.

[23] V. T. N. Mai, A. Shukla, M. Mamada, S. Maedera, P. E. Shaw, J. Sobus, I. Allison, C. Adachi, E. B. Namdas, S.-C. Lo, *ACS Photonics*, **2018**, *5*, 4447.

[24] M. Inoue, T. Matsushima, C. Adachi, *Appl. Phys. Lett.*, **2016**, *108*, 133302.

[25] H. Kogelnik, C. V. Shank, *Appl. Phys. Lett*., **1971**, *18*, 152.

[26] C. Karnutsch, C. Pflumm, G. Heliotis, J. C. deMello, D. D. C. Bradley, J. Wang, T. Weimann, V. Haug, C. Gärtner, U. Lemmer, *Appl. Phys. Lett*., **2007**, *90*, 131104.

[27] F. Bencheikh, A. S. D. Sandanayaka, T. Matsushima, J. C. Ribierre, C. Adachi, *J. Appl. Phys.*, **2017**, *121*, 233107.

[28] T. Matsushima, S. Yoshida, K. Inada, Y. Esaki, T. Fukunaga, H. Mieno, N. Nakamura, F. Bencheikh, M. R. Leyden, R. Komatsu, C. Qin, A. S. D. Sandanayaka, C. Adachi, *Adv. Funct. Mater.*, **2019**, *29*, 1807148.

Chapter 3

Markedly improved performance of optically pumped organic lasers with two-dimensional distributed-feedback gratings

C. A. M. Senevirathne, A. S. D. Sandanayaka, B. S. B. Karunathilaka, T. Fujihara, F. Bencheikh, C. Qin, K. Goushi, T. Matsushima, C. Adachi, *ACS Photonics*, **2021**, *8*, 1324.

3.1 Introduction

One reason which makes CW lasing difficult in organics is the thermal degradation caused by intense photoexcitation[1–3]. If a laser material has a higher lasing threshold, the material should be photoexcited with high power to reach the threshold condition. That intense photoexcitation will eventually lead to thermal degradation of the molecules. A decrease in laser threshold suppresses the thermal degradation and, therefore, leads to long-lasting lasing from organic laser dyes. Even if a laser material has spectral separation of a triplet absorption from a laser spectrum, laser performance under CW photoexcitation can be limited because of the high lasing threshold, leading to degradation. Therefore, here I investigate the importance of lowering the lasing threshold in order to operate laser devices under CW photoexcitation.

Basically, laser emission characteristics were studied by employing four types of 2-D DFB resonators, which include second-order 2-D square lattice, second-order 2-D cross double, second-order circular, and mixed-order circular grating structures, as shown in Figure 3.1. These 2-D DFBs offer high photon confinement via increased feedback in more than one direction compared to 1-D DFB structures[4].

In second-order 2-D square lattice and cross double gratings, the light feedback takes place in two orthogonal directions, which are along the two grating axes as shown in Figure 3.1(a) and (b)[5–8]. In terms of uncoupling conditions, 2-D DFBs can be considered as the linear combination of 1-D DFB gratings. Therefore, these gratings provide light feedback *via* second-order Bragg diffraction and surface light outcoupling *via* first-order diffraction[9]. When that takes place in two orthogonal grating axes, the output laser beam grasps the characteristics of an azimuthally polarized low divergent beam[10, 11].

In the case of circular gratings, feedback takes place in all radial directions, as shown in Figure 3.1 (c) and (d). In these gratings, the light propagates back and forth in all radial directions, generating a highly directional, well-defined, low divergent, azimuthally polarized circular-shaped narrow laser beam. Moreover, these circular DFB gratings exhibit

high output power than other feedback structures because of their in-plane high gain surface areas[12−16].

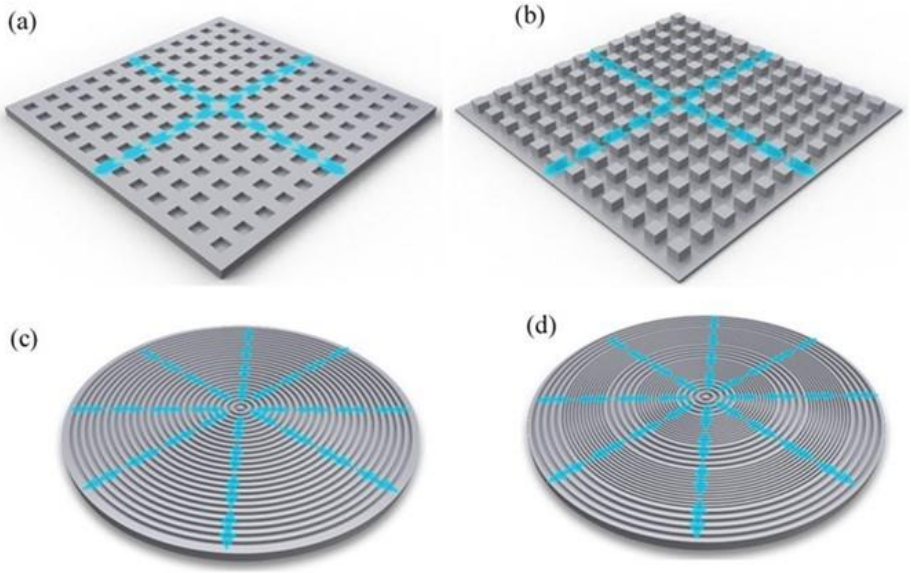

Figure 3.1. 2-D DFB resonator structures were designed to improve laser performance. (a) Second-order 2-D square lattice, (b) second-order 2-D cross double, (c) circular second-order, and (d) circular mixed-order grating structures.

In this study, I conducted a comprehensive study on laser characteristics of a 6 wt % BSBCz:CBP blend film with four types of 2-D DFB structures discussed earlier, which provide feedback in different ways and lower laser threshold from BSBCz, which has no spectral overlap between the laser emission and the excited-state triplet absorption[17]. Hence material itself satisfies the CW laser condition discussed in section 1.3.7.1 in chapter 1. Moreover, when increased the feedback via circular mixed-order, stimulated emission lifetime is getting shorter compared to 2-D cross double grating structures. If stimulation emission lifetime is lowered, the chance of populating T_1 state via ISC is less possible according to constant rate model discussed in section 1.3.7.1 in chapter 1. As a result, I could achieve extended CW lasing by implementing circular mixed-order DFB structures. Additionally, I investigated how much the laser durability can be improved with 2-D DFB resonators.

3.2 Experimental

DFB Fabrication

All 2-D DFBs were fabricated as described in chapter 2, section 2.2 under the title of *DFB Laser Device Fabrications.*

Organic Laser Device Fabrication

To complete the laser devices, a 200-nm-thick 6 wt % BSBCz:CBP blend film was prepared on the gratings by thermal evaporation under the pressure of ~2.0×10^{-4} Pa at a total evaporation rate of 0.1−0.2 nm s^{-1}. A 0.05 ml of CYTOP was directly spin-coated onto the laser devices at 1000 rpm for 30 s. After, a sapphire lid was placed on top of the CYTOP layer, and then the laser device samples were dried in vacuum overnight.

Laser Characterization under Short-Pulse Photoexcitation

For the characterization of the fabricated organic lasers, pulsed excitation light from a nitrogen laser was focused on a 5.2×10^{-3} cm^2 area of the devices through a lens and slit. Unless otherwise noted, these lasers were characterized under short-pulse photoexcitation exactly as described in chapter 2, section 2.2 under the title of *Laser Characterization under Short-Pulse Photoexcitation.*

Near-Field and Far-Field Laser Emission Characterization

For the near-field emission profile measurement, a C9164-01 Hamamatsu photonics CCD camera was used, with a distance between the sample and the camera being kept at 2 cm. For the far-field emission profile measurement, a C9664-01G02 Hamamatsu photonics CCD camera was used, with a distance between the sample and the camera being kept at 1 cm.

Laser Characterization at qCW and CW Photoexcitation

For qCW and CW photoexcitation, I used a CW laser diode (OBIS LG CW Ultraviolet Laser with a maximum power of 50 mW and an excitation wavelength of 355 nm) in

combination with an acousto-optic modulator (AOM, Gooch&Housego), which was triggered with a pulse generator (WF 1974, NF). The excitation light was focused on a 8.76 × 10^{-6} cm^2 area of the devices through a lens and a slit, and the emitted light was collected using a streak scope (C7700, Hamamatsu Photonics) with a time resolution of 100 ps and a digital camera (C9300, Hamamatsu Photonics). The size of the excitation area was carefully checked by using a dual scanning slit beam profiler (BP209-VIS).

3.3 Results and discussion

3.3.1 DFB fabrication

DFB pitches were calculated according to the Bragg equation which described in Chapter 1, section 1.4.1. The period values for the first-order (m = 1) and second-order (m = 2) DFB resonator structures used in this study were calculated to be 140 and 280 nm, respectively, with the previously reported λ_{Bragg} and n_{eff} values of BSBCz [3]. The duty cycle (hill width/period width) and height of the DFB structures were selected according to the optical simulation results discussed later.

3.3.1.1 Optical simulations

To calculate confinement factors (Γ) and quality factors (Q-factor) of 2-D DFB structures with different duty cycles and grating heights, Helmholtz equation was solved for every frequency, which was related to the eigenvalue of the resonator, using a finite element method (FEM) in a Radio Frequency module of COMSOL 5.3a software. The FEM is an attractive method used to analyze eigenvalue problems in two and three-dimensional structures with complicated geometries. The computation domain is limited to one period unit cell of the grating. Periodic boundary conditions were applied for lateral boundaries. Scattering boundary conditions were used for the top and bottom domains. Then, the eigenfrequency solver was used to find the eigenvalues of the eigenmodes of the resonant cavity. The input parameters used for the optical simulation were an organic film thickness (200 nm) and the refractive indices of the films. The CYTOP layer (n_{CYTOP} = 1.35) and the SiO_2 substrate (n_{SiO2} = 1.46) were considered to be semi-infinite layers. The refractive index of the BSBCz film was n_f = 1.89 [18].

3.3.1.2 Duty cycle of the fabricated DFBs

The duty cycle of the gratings was kept at 50% for all 2-D DFB structures. The choice of the duty cycle was selected by considering the optical simulation results shown in Table 3.1. Although the *Q*-factor increases with a small duty cycle of 25%, I chose the 50% duty cycle to fabricate all DFB structures, considering the practical limitations occurring when small pitch sizes were used. Period sizes and pitch sizes used in each DFB structure are shown in Figure 3.2.

In this study, the widths of both the hills and valleys were 140 nm for second-order 2-D square lattice, second-order 2-D cross double, and second-order circular grating structures. For a mixed-order circular grating structure, the hill and valley widths were 140 nm in the second-order region and were 70 nm in the first-order region, as shown in Figure 3.2 below. In this study, the widths of both the hills and valleys were 140 nm for second-order 2D square lattice, second-order 2D cross double, and second-order circular grating structures. For a mixed-order circular grating structure, the hill and valley widths were 140 nm in the second-order region and were 70 nm in the first-order region, as shown in Figure 3.2 below. In the circular mixed-order grating structure, twelve first-order pitches and four second-order pitches were incorporated.

Table 3.1. *Q*-factors and λ as a function of duty cycles.

Width of hill (nm)	Width of valley (nm)	Duty cycle (%)	*Q*-factor	λ (nm)
70	210	25	9859	479
140	140	50	8923	477
180	100	64	8103	473
210	70	75	No resonant mode	

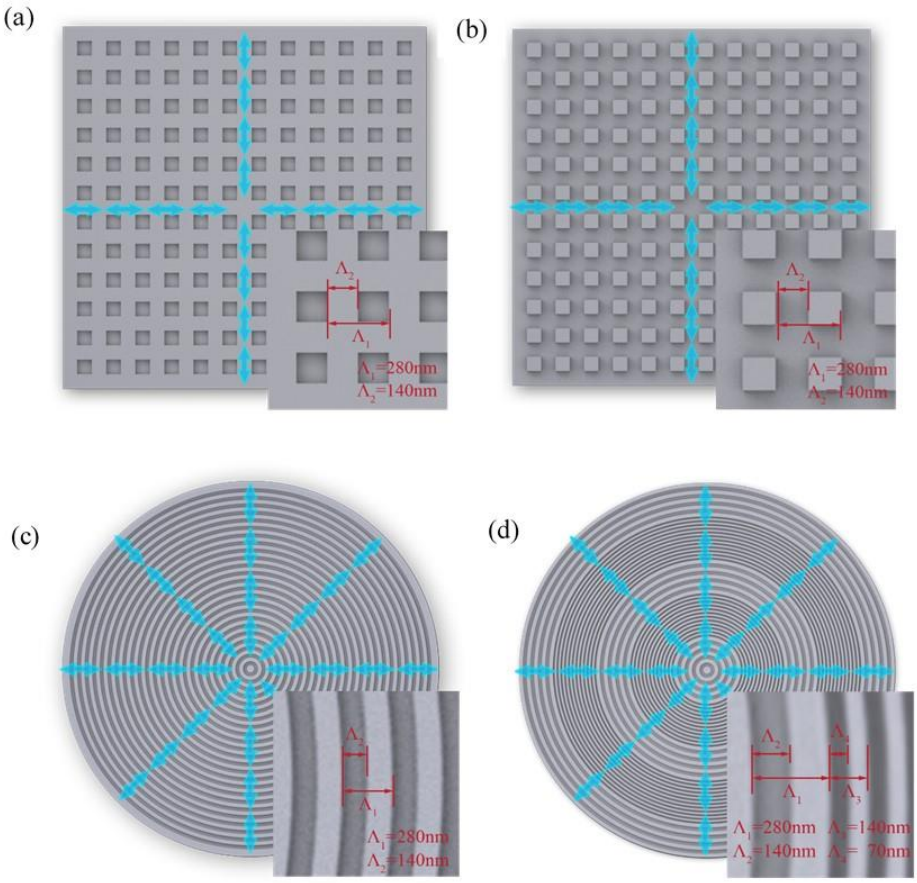

Figure 3.2. Duty cycles of 2D DFB resonator structures. (a) Second-order 2-D square lattice, (b) second-order 2-D cross double, (c) circular second-order, and (d) circular mixed-order grating structures. Λ_1 (280 nm) and Λ_2 (140 nm) are a period and pitch size of the second-order DFB regions. Λ_3 (140 nm) and Λ_4 (70 nm) are a period and pitch size of the first-order regions for a mixed-order circular grating structure.

3.3.1.3 Grating depths of fabricated DFBs

The grating depth of all the DFBs was kept around 65 nm. The choice of the grating depth was selected by considering the simulation results shown in Table 3.2. Although the shallower DFB grating looks much more promising according to the optical simulation results, I chose a mid-value of 65 nm in depth for fabricating all DFB structures when considering practical limitations and a small change of grating depths in grating patterns with

shallower depths being prone to affect the laser device performance significantly. Moreover, I compared all four different DFB structures with a single grating height for simplicity, although there is a room to further optimize each DFB structure.

Table 3.2. *Q*-factor and λ values simulated with various grating depths of second-order 2D cross-double gratings.

Grating depth (nm)	λ (nm)	*Q*-factor
30	477	9420
65	477	8923
80	477	8800

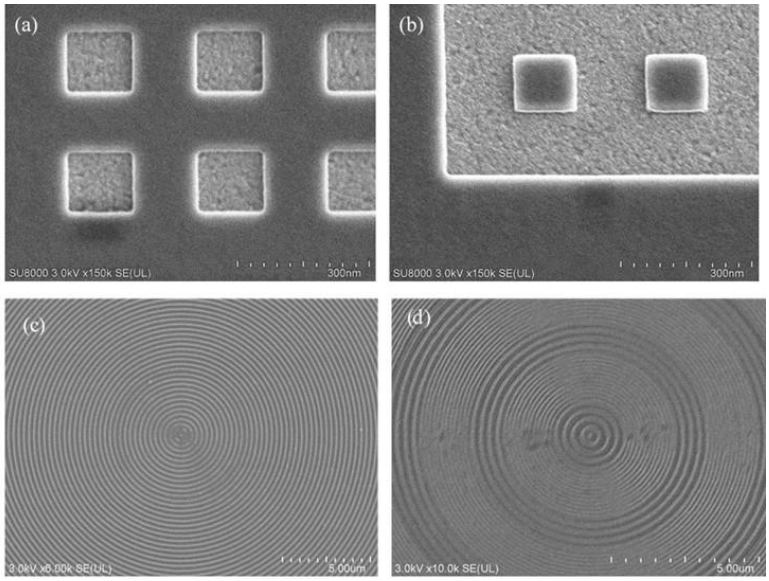

Figure 3.3. Well-defined 2-D DFB structures were obtained**.** SEM images of (a) second-order 2-D square lattice, (b) second-order 2-D cross double, (c) second-order circular, and (d) mixed-order circular grating structures, which were fabricated on SiO_2 substrates.

Figures 3.3 (a–d) show SEM images of the 2-D DFB structures. From these SEM images, the period values were estimated to be 140 ± 5 and 280 ± 5 nm in the first-order and second-order regions, respectively. These experimental periods agree with the calculated values obtained using the Bragg equation (equation no 1.23 in chapter 1). The total areas of both the

second-order 2-D lattice and second-order 2-D cross double DFB grating regions were 2 × 2 mm^2. The diameters of the circular second-order and mixed-order gratings were 2 mm.

3.3.2 Laser device fabrication

Because of the aforementioned promising photophysical characteristics of a 6 wt % BSBCz:CBP blend film (see section 1.3.7.3 in chapter 1), we used this film for the fabrication of laser devices. The chemical structures of BSBCz and CBP are shown in Figure 3.4 (a). A 6 wt % BSBCz:CBP blend film was vacuum-deposited on top of the DFB resonator structures. Then, these laser devices were encapsulated using a CYTOP film and a sapphire substrate, as illustrated in Figure 3.4 (b). The BSBCz:CBP blend film thickness was around 200 nm, providing a laser peak around a wavelength of spontaneous emission in the (transverse electric) TE_0 mode[19]. Otherwise, thinner or thicker BSBCz:CBP films led to higher laser thresholds because of weaker confinement of the waveguide modes for thinner films or competition of the fundamental mode with higher-order modes for thicker films.

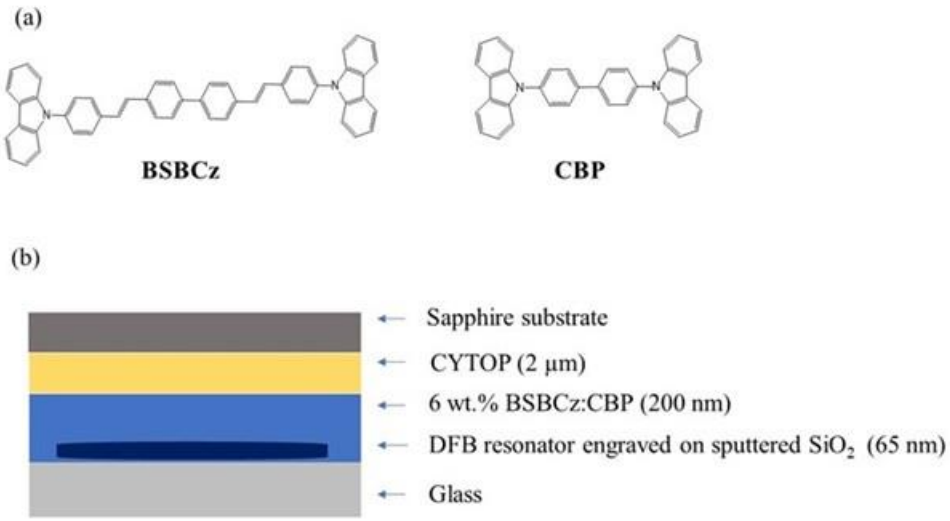

Figure 3.4. Laser devices containing an appropriate laser dye and grating structure with thermal management are key for high performance. (a) Molecular structures of BSBCz and CBP and (b) fabricated laser device architecture.

3.3.3 Laser under short-pulse photoexcitation

First, I investigated the surface-emitting laser characteristics of devices with the four 2-D DFB resonator structures under short-pulse photoexcitation from a nitrogen laser. The excitation wavelength was 337 nm, the repetition rate was 20 Hz, and the pulse width was 3.5 ns. The photoexcitation area was 5.2×10^{-3} cm^2, which is much smaller than the grating area.

This excitation wavelength is ideal for the blend films because CBP has a strong absorption at this wavelength. The excited-state energy generated in CBP by the absorption of the excitation light is immediately transferred to BSBCz *via* a Förster resonance energy transfer (FRET). This energy transfer is efficient because the emission spectrum of CBP largely overlaps with the absorption spectrum of BSBCz [20]. In fact, even at high excitation power, we obtained the emission from BSBCz only and not from CBP, indicating the efficient energy transfer.

Figures 3.5 show the emission profiles of the laser devices operating under the short-pulse photoexcitation. There is a Bragg dip in the emission profiles measured near the lasing threshold. This dip corresponds to the photonic stopband of the particular grating structure. The emission wavelengths were ~475, ~477, ~477, and ~478 nm for laser devices with second-order 2-D square lattice, second-order 2-D cross double, second-order circular, and mixed-order circular gratings, respectively. From all the devices, laser oscillation was seen near the edges of the photonic stopband, which is proof of photonic band-edge lasing.

However, the photonic band-edge lasing appears at a high-energy band-edge for laser devices with second-order 2-D square lattice and second-order 2-D cross double gratings [Figure 3.5 (a) and (b)]. In contrast, the photonic band-edge lasing was at a low-energy side for the other circular DFB devices [Figure 3.5 (c) and (d)]. At the photonic band edges, the group velocity of light becomes zero. As a result, this increases the photon–matter interaction at the photonic band edges. Hence, in the presence of an organic gain medium, lasing happens at either high- or low-energy photonic band-edge. The band-edge lasing position is determined by the overlap between the photonic band edge and the PL spectrum of the

organic gain medium[21]. In the case of second-order 2-D gratings, the high-energy photonic band edge overlaps more with the PL spectrum of the BSBCz:CBP blend film [Figure 3.6 (a)]. The low-energy band-edge lasing is facilitated in circular grating DFB devices as 0-1 transition is more favorable in lasing despite the smaller overlapped band-edge with the PL spectrum of the BSBCz:CBP blend film [Figure 3.6 (b)]. Further, all the devices exhibited a very sharp laser peak above the lasing threshold with FWHM values below 0.3 nm, suggesting good temporal coherence of our 2 D DFB laser devices.

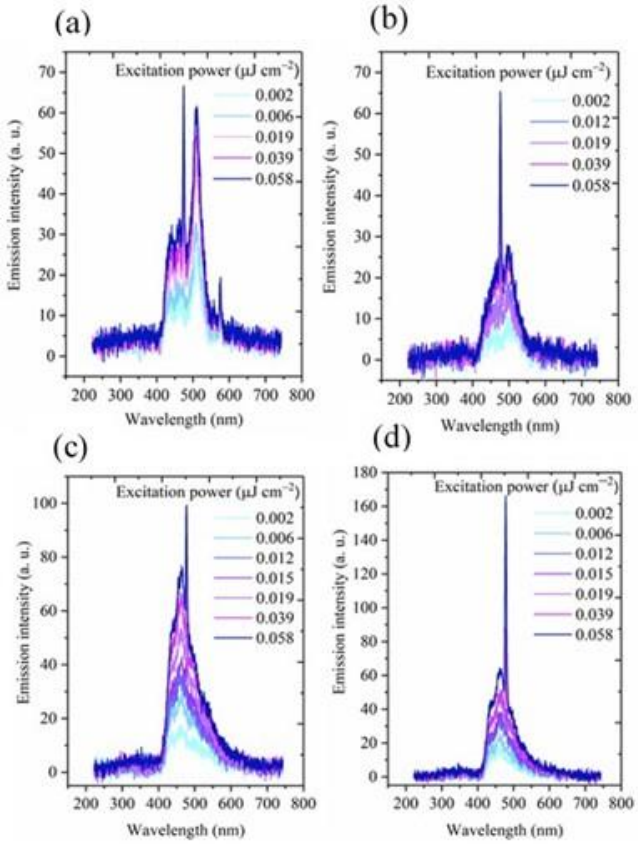

Figure 3.5. Sharp laser peaks were detected from 2-D DFB devices. Emission profiles near the laser thresholds for devices with (a) second-order 2-D square lattice, (b) second-order 2-D cross double, (c) second-order circular, and (d) mixed-order circular grating structures.

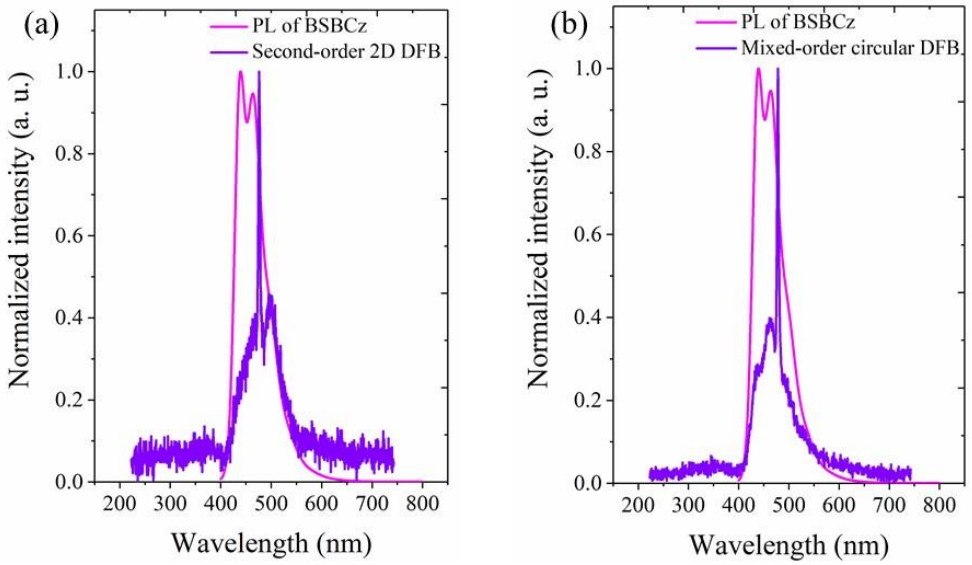

Figure 3.6. Laser emission happens near the photonic band edge. (a) High-energy photonic band-edge lasing from second-order 2-D grating laser devices and (b) low-energy photonic band-edge lasing from mixed-order circular grating laser devices.

As can be seen in Figure 3.7, the emission intensities increased linearly below the laser thresholds and began to be amplified when the stimulated emission overcame the spontaneous emission. The laser E_{th} in each laser device was calculated from the change in slope of the emission intensities. The calculated E_{th} values were 0.04 ± 0.05, 0.02 ± 0.05, 0.03 ± 0.05, and 0.015 ± 0.004 μJ cm^{-2} for laser devices with second-order 2-D square lattice, second-order 2-D cross double, second-order circular, and mixed-order circular grating structures, respectively. The small discrepancy observed in the threshold values of devices with the second-order 2-D cross double and second-order 2-D square lattice gratings (0.04 ± 0.05 and 0.02 ± 0.05 μJ cm^{-2}) may be due to the formation of structural defects in gratings. However, these threshold values are lower than that of a previously reported 1-D second-order DFB laser device with a similar BSBCz emitter (~0.22 μJ cm^{-2})[20]. The lower threshold values would be attributed to the enhanced feedback taking place in the two orthogonal directions of the 2-D DFB structures.

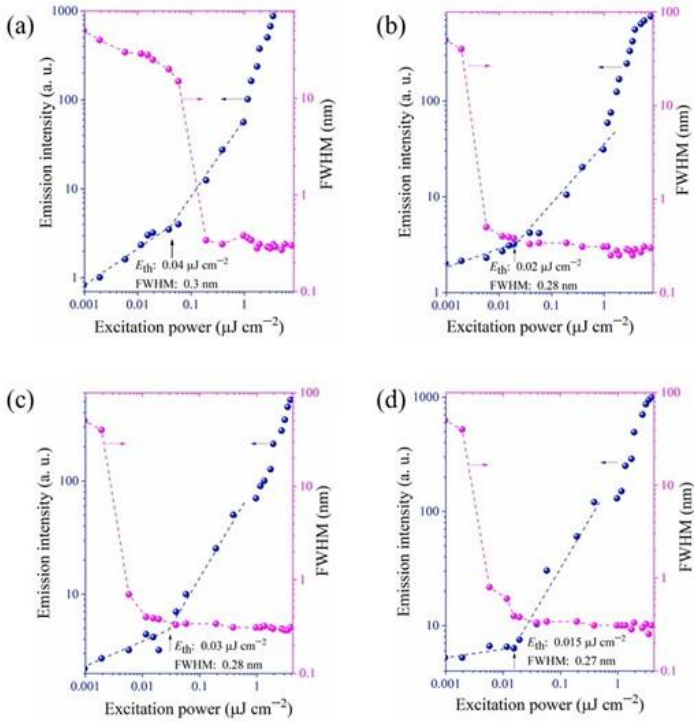

Figure 3.7. Reduced laser thresholds in 2-D DFB grating laser devices under short-pulse photoexcitation. Emission intensity vs. excitation intensity graphs of laser devices with (a) second-order 2-D square lattice, (b) second-order 2-D cross double, (c) second-order circular, and (d) mixed-order circular grating structures

Second-order circular gratings provided even lower thresholds than second-order 2-D square lattice gratings did because of the increased feedbacks in all the radial directions [8]. Moreover, mixed-order circular gratings, in which the first-order region is used to induce the feedback in the direction parallel to the substrate and the surface-emitting laser comes from the second-order region, were able to further reduce the thresholds when compared with the other gratings. In other words, out of the four DFB resonator structures, the mixed-order circular DFB structure gave the lowest lasing threshold of 0.015 ± 0.004 μJ cm^{-2}. It is worth mentioning here that this threshold is also lower than that of BSBCz-based laser devices with a 1-D mixed-order grating structure (~0.09 μJ cm^{-2}) [3]. We demonstrated a marked decrease in the laser threshold by using the circular grating structure.

3.3.4 Claim of laser emission under short-pulse photoexcitation

To check spatial and temporal coherence, I first measured near-field images of laser profiles of our devices operating above the thresholds. Figure 3.8 shows near-field images captured from devices having second-order 2-D square lattice, second-order 2-D cross double, and mixed-order circular grating structures, respectively. They clearly exhibited the increased surface light scattering on particular DFB areas than the outer area of the DFBs, giving bright fringes.

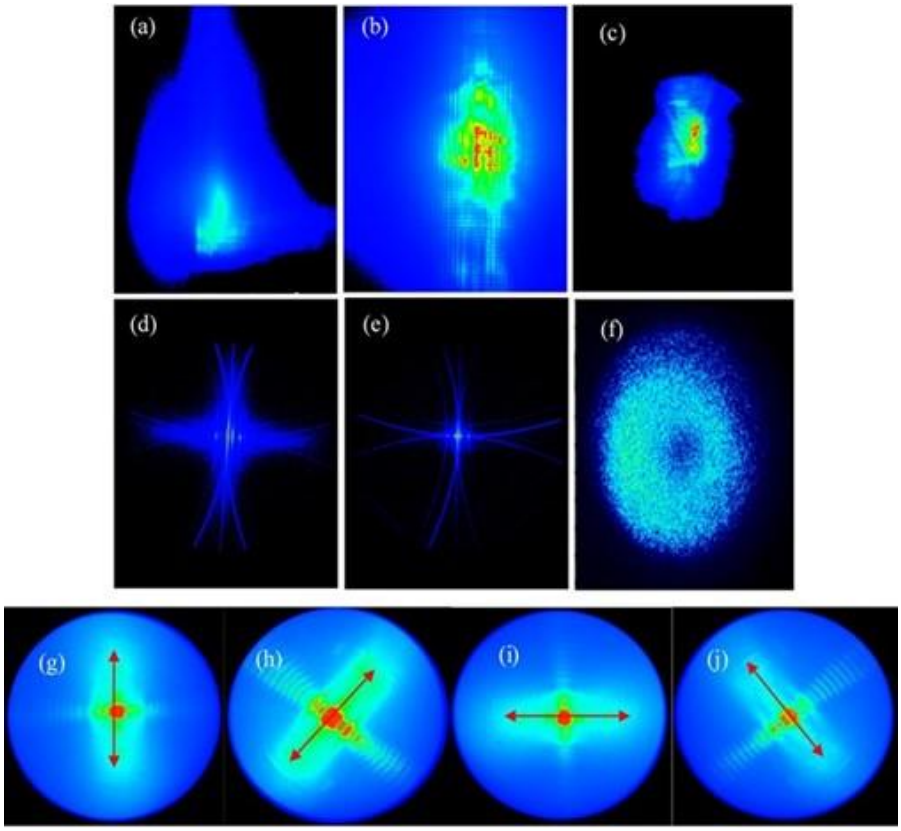

Figure 3.8. Near-field and far-field images were taken for claiming laser action. Near-field images of (a) second-order 2-D square lattice, (b) second-order 2-D cross double, and (c) mixed-order circular grating containing laser devices. Far-field images of (d) second-order 2-D square lattice, (e) second-order 2-D cross double, and (f) mixed-order circular grating containing laser devices**.** Azimuthal polarization from a mixed-order circular DFB laser device when polarizer axis angles were (g) 0º, (h) 45º, (i) 90º, and (j) 135º. The polarizer axes are shown in red double arrow. All images were obtained at an excitation power of 0.8 μJ cm^{-2}, which is above the lasing threshold.

Next, I measured far-field images of laser profiles of the same devices. Conventionally, an output beam profile from a 1D DFB laser inherits a characteristic fan shape pattern as it provides confinement in only one direction. This fan shape arises because of high light confinement perpendicular to the grating axis and a much larger divergence occurring parallel to the grating axis. Therefore, the output beam is linearly polarized along the grating axis and acquire TEM_{01} (transverse electric and magnetic) mode[14]. In the case of devices with second-order 2-D square lattice and cross double gratings, light is confined in a 2-D plane. In these devices, two linearly polarized TEM_{01} modes appear along the *x*- and *y*- axes of the gratings because of their 2-D nature. These two linearly polarized emission profiles sum up, resulting in azimuthally polarized laser beams[22]. Near the lasing threshold, the laser from these devices acquires an annular profile. However, when excitation intensity becomes high enough to induce lasing, far-field profiles begin to have a characteristic cross profile shape, with linear polarization perpendicular to each other, as shown in Figure 3.8 (d) and (e) [23].

Figure 3.8 (f) shows a far-field pattern obtained from mixed-order circular DFB laser devices. It shows the characteristic annular shape profile, which resulted from azimuthal polarization in mixed-order circular DFB gratings because of its operation in a circularly symmetric fashion. A dark spot at the centre was associated with zero electric field occurring because of azimuthal polarization[24]. To investigate this behaviour, we passed the laser output beam through a polarizer oriented in 0, 45, 90, and 135º angle, as shown in Figure 3.8 (g–j)**.** As the azimuthally polarized beam exists everywhere in *ø* direction (in polar-coordinates), the radiation field perpendicular to the polarizer axis blocks and passes the radiation field parallel to the polarizer axis in each orientation.

3.3.5 Laser studies under long-pule photoexcitation

Long-pulse laser studies were then carried out on devices having second-order 2-D cross double and mixed-order circular grating structures. Both laser devices were photoexcited with a long pulse width of 1 s and a repetition rate of 0.01 Hz at a wavelength

of 355 nm. Figure 3.9 (a) shows emission spectra obtained from laser devices with a mixed-order circular grating structure. Under long-pulse photoexcitation, a laser peak appeared at ~ 478 nm, with an average-power laser threshold of ~10 W cm^{-2} (a peak-power laser threshold of ~1 kW cm^{-2}) and an FWHM value of ~ 0.2 nm [Figure 3.9 (b)].

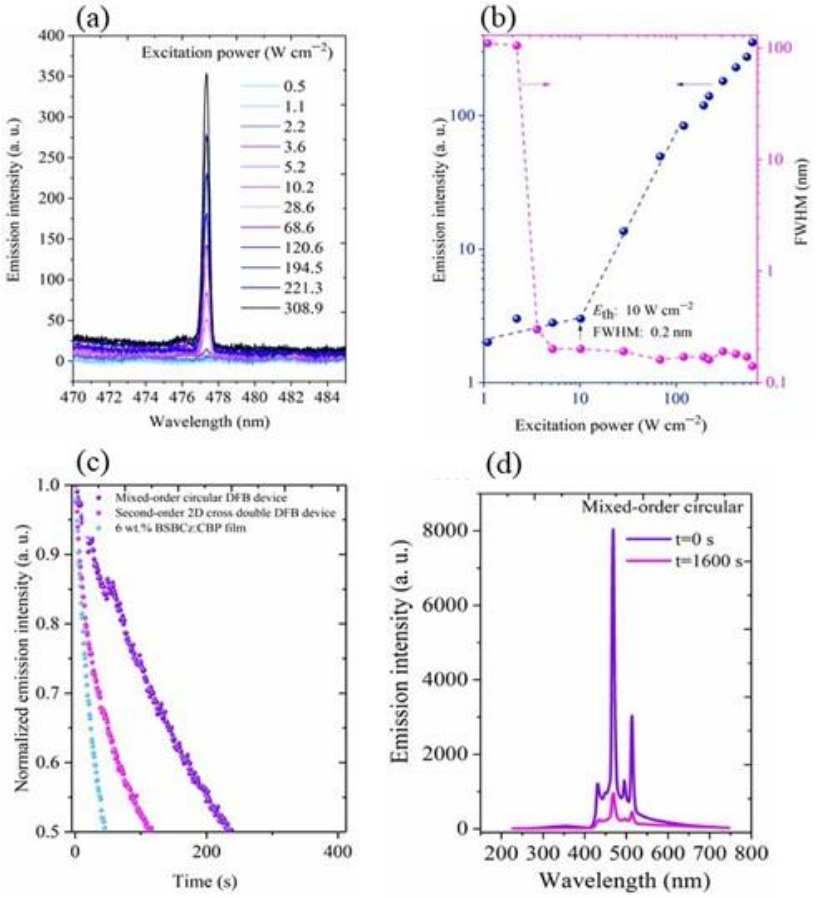

Figure 3.9. CW laser durability was improved. (a) Emission profiles and (b) emission intensity vs excitation intensity graphs of BSBCz-based laser devices with a mixed-order circular DFB resonator structure when these devices were photoexcited with 1 s of 355-nm photoexcitation. (c) Emission stability of mixed-order circular and second-order 2-D cross double grating DFB laser devices and BSBCz:CBP films under CW photoexcitation at a power of 43 W cm^{-2}. (d) Emission spectra measured from a mixed-order circular laser device with the same CW photoexcitation at t = 0 and t = 1,600 s.

Further, circular DFB laser devices were able to operate even at the true CW condition without ceasing the laser emission, as shown in streak camera images (Figure 3.10).

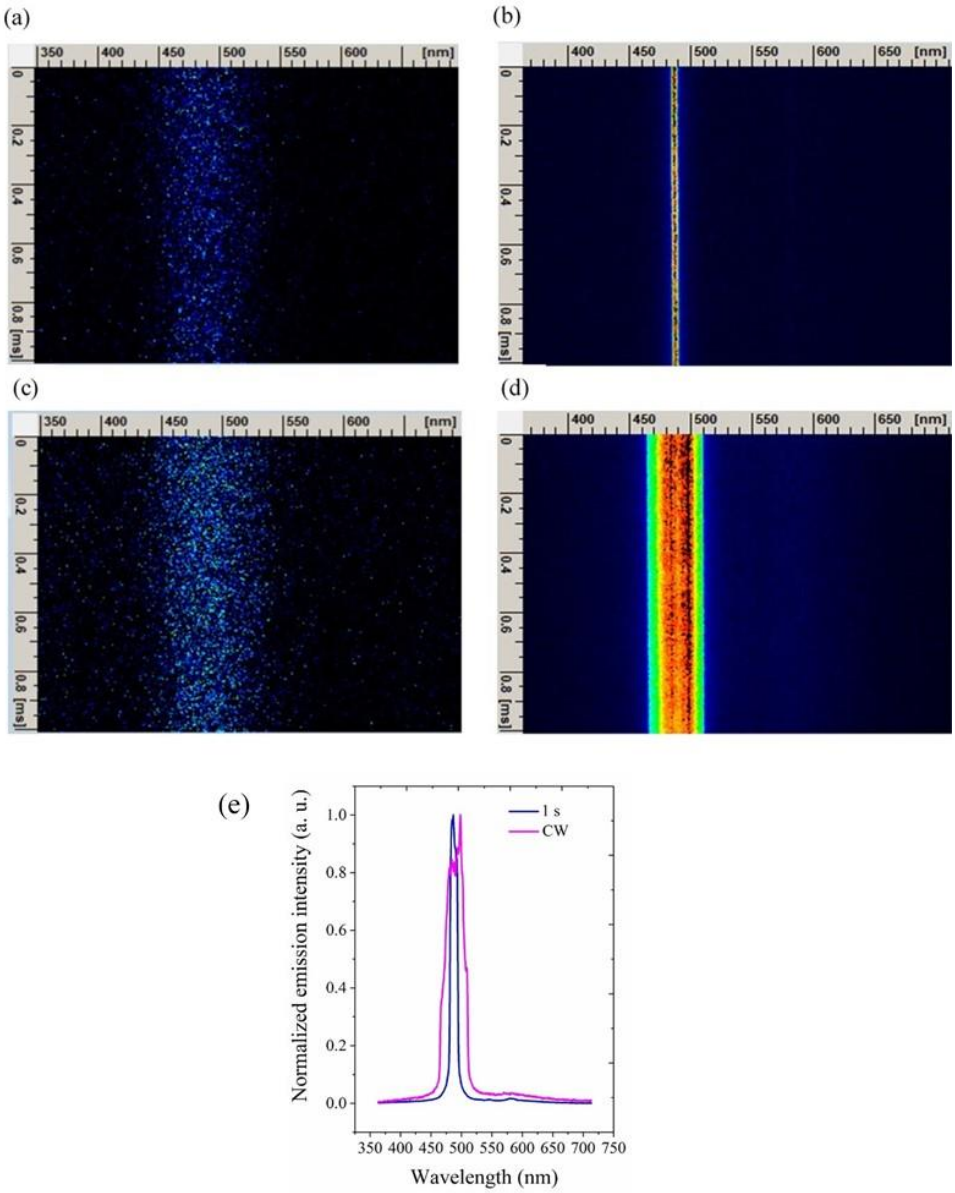

Figure 3.10. Streak camera images. Streak camera images integrated over 100 pulses of the laser emission from mixed-order circular DFB laser devices (a) below and (b) above the lasing threshold under 1 s photoexcitation and (c) below and (d) above lasing threshold under CW photoexcitation. (a) and (c) were obtained at an excitation power of 6 W cm^{-2}, and (b) and (d) were obtained at an excitation power of 1 kW cm^{-2}. (e) Comparison of laser spectra measured with 1 s and true CW photoexcitation above the lasing threshold.

Previously the same BSBCz laser device was obtained a laser duration of 30 ms at a photoexcitation power of 2 kW cm^{-2} with a 1-D mixed-order grating structure[3]. The present laser duration (1 s and CW photoexcitation) is much longer than the reported value (30 ms). This may be ascribed to the suppressed thermal degradation, which is associated with the lower laser thresholds from 2-D grating laser devices.

3.3.6 Laser stability under CW photoexcitation

The operational stabilities of mixed-order circular and second-order 2-D cross double grating DFB laser devices and 6 wt % BSBCz:CBP films (without DFB) were investigated directly under CW photoexcitation at an excitation intensity of 43 W cm^{-2} [Figure 3.9 (c)]. Under the CW photoexcitation, the emission intensity of all the samples decreased with time, which was irreversible and is assumed to be the laser-induced chemical and thermal degradation of BSBCz and CBP. As the CW photoexcitation continued, the stimulated emission decreased in intensity, and the normal spontaneous emission became dominant, as shown in Figure 3.9 (d) for mixed-order circular laser device.

For second-order 2D cross double grating DFB laser devices, the half-lifetime, at which the emission intensity decreases to half of the initial, was ~123 s, which is ~2.5 times that of BSBCz:CBP films (~50 s). With the circular mixed-order DFB laser device, the half-lifetime was ~245 s, which is ~5 times that of BSBCz:CBP films (~50 s) and ~2 times that of second-order 2D cross double grating DFB laser devices. However, BSBCz:CBP films show spontaneous emission, and DFB laser devices show stimulated emission. Then a question arises why the stability improvement was possible with an optical resonator, although the same excitation power for all the samples was used. This is because, those organic molecules showing stimulated emission may be more difficult to chemically decompose than those showing spontaneous emission even at the same photoexcitation power. This is because a shorter stimulated emission lifetime than a spontaneous emission lifetime leads to a lower chance of the triplet formation and the chemical decomposition via the triplets[25]. Byproducts

generated as the result of the chemical decomposition reportedly work as quenchers for excited states, which terminates lasing.

For a better understanding of the aforementioned behaviors, I measured time-resolved transient emission decays from circular mixed-order and second-order 2-D cross double DFB laser devices at a photoexcitation power of 7 μJ cm^{-2} [Figure 3.11(a) and (b)]. Transient emission decay profiles at the laser peak wavelengths were taken from the streak camera images [Figure 3.11(c)] and revealed that stimulated emission was present, along with cavity-induced ASE. When a laser device is photoexcited, several round trips (feedback) of light are required to build up the laser. Before reaching the laser build-up time, devices strongly show cavity-induced ASE[26]. This ASE component decreases as photoexcitation power is increased since devices can quickly reach the laser build-up time[27]. Moreover, when the feedback is enhanced by using a higher-quality optical resonator, the ASE component also decreases since enhanced feedback facilitates the laser build-up[28]. The stimulated emission lifetimes estimated with double-exponential fitting for second-order 2-D cross double and mixed-order circular DFB laser devices were ~0.08 and ~0.034 ns, respectively. The estimated ASE lifetimes of these devices were ~0.8 and ~0.7 ns. It is clear that the lifetimes of the stimulated emission and ASE are shorter in circular mixed-order DFB laser devices because of their enhanced feedback compared to second-order 2-D cross double DFB laser devices. Additionally, the stimulated emission is more included in mixed-order circular DFB laser devices than in second-order 2D cross-double DFB laser devices [Figure 3.11 (c)]. These results infer that shorter excited-state lifetimes caused by using a higher-quality optical resonator, such as circular mixed-order gratings used in this study, can suppress a possibility of the chemical decomposition and, therefore, improve the laser stability.

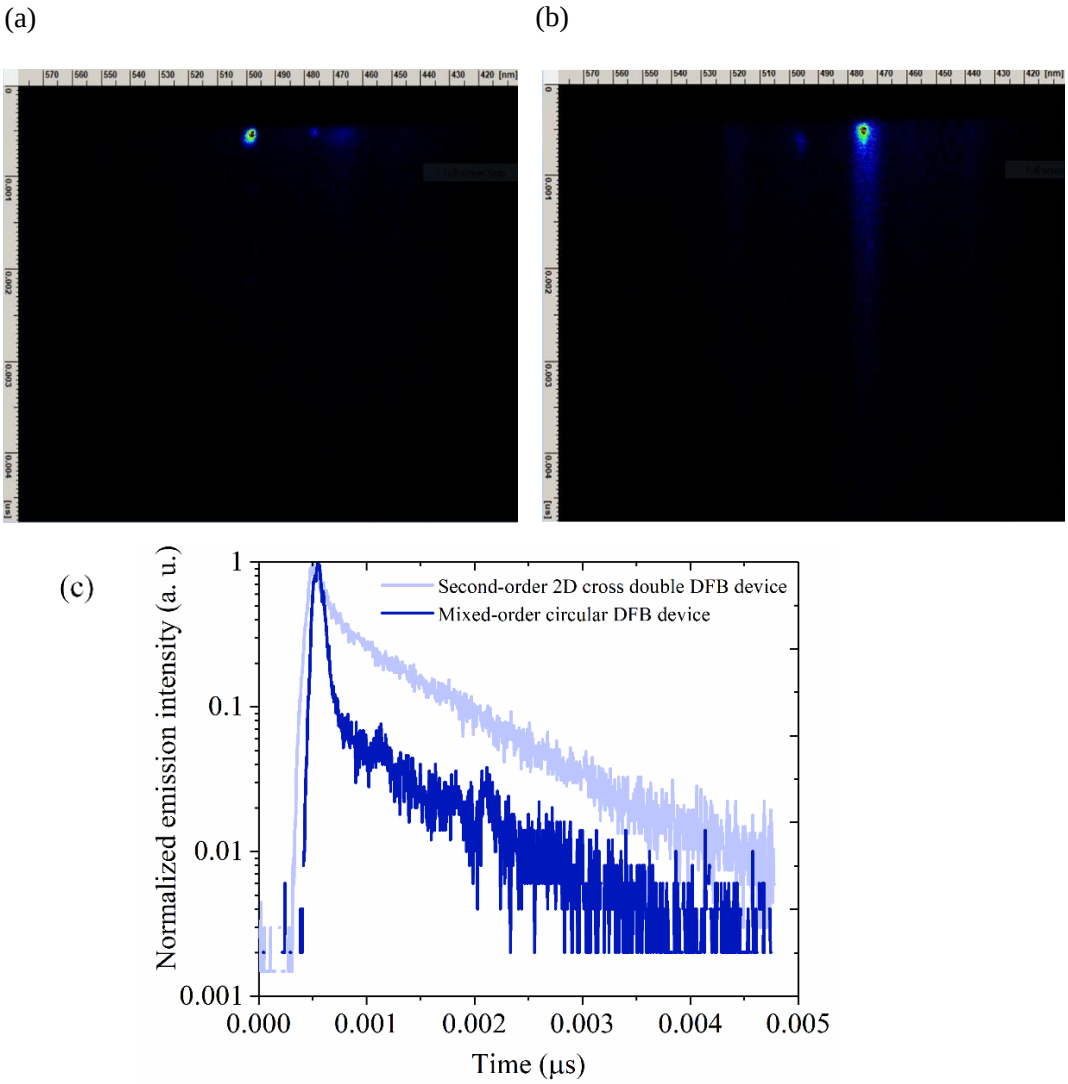

Figure 3.11. Using mixed-order circular gratings makes stimulated emission and ASE lifetimes shorter**.** Streak camera images of transient emission from (a) mixed-order circular DFB laser devices and (b) second-order 2-D cross double grating DFB devices. (c) Transient emission profiles taken from (a) and (b). The excitation source was Nd:YAG laser providing an excitation power of 7 μJ cm^{-2}, excitation wavelength of 355 nm, pulse width of 30 ps, and repetition rate of 10 Hz. This excitation power was higher than the laser thresholds. The first decay component is the stimulated emission, and the second decay component is the cavity-induced ASE.

In addition, heat generation on laser devices with different DFB structures will give more in-depth information of the stability I observed with these laser devices. However, conducting thermal simulations on two types of 2-D DFB structures find difficult at the moment. Moreover, no works have been reported on heat generation effect on 2-D DFBs under CW regime. However, Sandanayaka et al.[3] reported that when increasing pulse width, thermal generation increased in BSBCz. However, after around 30 ms this heat generation saturates in this encapsulated 1- D DFB laser structures and no longer effect in more longer pulses for BSBCz. However, this study was conducted neglecting the effect of grating. Therefore, heat generation effect of 2-D DFB lasers under CW regime is not clear at the moment.

3.4 Conclusion

I investigated how laser performance is affected when using four different 2-D resonator structures. For this purpose, a BSBCz:CBP blend film was combined as the gain medium with second-order 2D square lattice, second-order 2D cross double, second-order circular, and mixed-order circular gratings. Out of four resonators, a mixed-order circular grating structure offered the lowest lasing threshold of ~0.015 μJ cm^{-2}, which is also the lowest ever reported in any BSBCz-based laser device. In mixed-order circular devices, I also realized lasing can occur even under 1 s of photoexcitation, with a low average-power laser threshold of ~10 W cm^{-2} (a peak-power laser threshold of ~1 kW cm^{-2})**.** I found that mixed-order circular devices became more stable under CW photoexcitation because of the shorter excited-state lifetime suppressing the chemical decomposition. In CW lasing literature, no work has been reported CW lasing using 2-D DFB structures. All of the reported works have been used, second-order, mixed-order, or first-order 1-D DFB structures. In all these works DFBs were introduced for the sake of getting lasing. No works have been pointed the importance of a selection of a proper DFB structure. Thereby, I could introduce the importance of using high quality DFB structures to get CW lasing. Up to now, only intrinsic properties such as TA and STA effects were prioritized in obtaining CW lasing rather than external factors such as DFBs. Therefore, this method of reducing laser thresholds by

employing 2D DFB structures with increased feedback would make it possible to fabricate CW-operating OSLDs in the future.

References

[1] Z. Zhao, O. Mhibik, T. Leang, S. Forget, S. Chénais, *Optics Express*, **2014**, *22*, 30092.

[2] Y. Zhang, S. R. Forrest, *Phys. Rev. B - Condens. Matter Mater. Phys.*, **2011**, *84*, 241301.

[3] A. S. D. Sandanayaka, T. Matsushima, F. Bencheikh, K. Yoshida, M. Inoue, T. Fujihara, K. Goushi, J.-C. Ribierre, C. Adachi, *Sci. Adv.* **2017**, *3*, e1602570.

[4] Y. Fu, T. Zhai, *Front. Optoelectron.*, **2020**, *13*, 18.

[5] W. L. Barnes, I. D. W. Samuel, G. A. Turnbull, P. Andrew, P. *Phys. Rev. B*, **2003**, *67*, 165107.

[6] N. Moll, R. F. Mahrt, C. Bauer, H. Giessen, B. Schnabel, E. B. Kley, U. Scherf, *Appl. Phys. Lett.*, **2002**, *80*, 734.

[7] G. Heliotis, R. Xia, G. A. Turnbull, P. Andrew, W. L. Barnes, I. D. W. Samuel, D. D. C. Bradley, *Adv. Funct. Mater.*, **2004**, *14*, 91.

[8] G. A. Turnbull, P. Andrew, W. L. Barnes, I. D. W. Samuel, *Appl. Phys. Lett.*, **2003**, *82*, 313.

[9] P. Zhou, L. Niu, A. Hayat, F. Cao, T. Zhai, X. Zhang, *Polymers (Basel)*, **2019**, *11*, 258.

[10] G. A. Turnbull, P. Andrew, W. L. Barnes, I. D. W. Samuel, *Appl. Phys. Lett.*, **2003**, *82*, 313.

[11] G. Heliotis, R. Xia, D. D. C. Bradley, G. A. Turnbull, I. D. W. Samuel, P. Andrew, W. L. Barnes, *J. Appl. Phys.*, **2004**, *96*, 6959.

[12] N. Moll, R. F. Mahrt, C. Bauer, H. Giessen, B. Schnabel, E. B. Kley, U. Scherf, *Appl. Phys. Lett.*, **2002**, *80*, 734.

[13] A. Jebali, R. F. Mahrt, N. Moll, D. Erni, C. Bauer, G. L. Bona, W. Bächtold, *J. Appl. Phys.*, **2004**, *96*, 3043.

[14] G. Heliotis, R. Xia, G. A. Turnbull, P. Andrew, W. L. Barnes, I. D. W. Samuel, D. D. C. Bradley, *Adv. Funct. Mater.*, **2004**, *14*, 91.

[15] T. Erdogan, O. King, G. W. Wicks, D. G. Hall, C. L. Dennis, M. J. Rooks, *Appl. Phys. Lett.*, **1992**, *60*, 1773.

[16] T. Erdogan, D. G. Hall, *Quantum Electron.*, **1992**, *28*, 612.

[17] H. Nakanotani, C. Adachi, S. Watanabe, R. Katoh, *Appl. Phys. Lett.*, **2007**, *90*, 4.

[18] D. Yokoyama, A. Sakaguchi, M. Suzuki, C. Adachi, *Org. Electron.*, **2009**, *10*, 127.

[19] F. Bencheikh, A. S. D. Sandanayaka, T. Matsushima, J. C. Ribierre, C. Adachi, *J. Appl. Phys.*, **2017**, *121*, 233107.

[20] A. S. D. Sandanayaka, K. Yoshida, M. Inoue, C. Qin, K. Goushi, J-C. Ribierre, T. Matsushima, C. Adachi, *Adv. Opt. Mater.*, **2016**, *4*, 834.

[21] C. T. Wang, C. W. Chen, T. H. Yang, I. Nys, C. C. Li, T. H. Lin, K. Neyts, J. Beeckman, *Appl. Phys. Lett.*, **2018**, *112*, 043301.

[22] R. Oron, S. Blit, N. Davidson, A. A. Friesem, Z. Bomzon, E. Hasman, E. *Appl. Phys. Lett.*, **2000**, *77*, 3322.

[23] S. Riechel, C. Kallinger, U. Lemmer, J. Feldmann, A. Gombert, V. Wittwer, U. A. Scherf, *Appl. Phys. Lett.*, **2000**, *77*, 2310.

[24] Y. Gao, L. Y. M. Tobing, A. Kiffer, D. H. Zhang, C. Dang, H. V. Demir, *ACS Photon.*, **2016**, *3*, 2255.

[25] T. Matsushima, S. Yoshida, K. Inada, Y. Esaki, T. Fukunaga, H. Mieno, N. Nakamura, F. Bencheikh, M. R. Leyden, R. Komatsu, C. Qin, A. S. D. Sandanayaka, C. Adachi, *Adv. Funct. Mater.*, **2019**, *29*, 1807148.

[26] I. A. Mcintyre, M. H. Dunn, M. H. *Opt. Commun.*, **1984**, *50*, 169.

[27] M. Goossens, A. Ruseckas, G. A.Turnbull, I. D. W.Samuel, *Appl. Phys. Lett.*, **2004**, *85*, 31.

[28] Z. Bor, *Opt. Commun.*, **1981**, *39*, 383.

Chapter 4

Recycling of triplets into singlets for high-performance organic lasers

C. A. M. Senevirathne, S. Yoshida, M. Yahiro, M. Auffray, B. S. B. Karunathilaka, F. Bencheikh, K. Goushi, A. S. D. Sandanayaka, T. Matsushima, C. Adachi, Recycling of Triplets into Singlets for High-Performance Organic Lasers. *(C. A. M. Senevirathne and S. Yoshida equally contributed) (submitted)*

4.1 Introduction

A TTA process is well-known for harvesting the non-emissive triplet excitons for the light-emissive process in fluorescent OLEDs. It has been reported that exceeding the theoretical EQE limit of 5% is possible even in fluorescent OLEDs by increasing 25% internal quantum efficiency further with the aid of a TTA process[1]. When the TTA processes repeat for a certain period of time, as discussed in section 1.3.5.4 of chapter 1, the number of the emissive singlet excitons will be eventually increased. Thus, the internal quantum efficiency of fluorescent OLEDs can be enhanced from 25% to 62.5% (25+75/2), resulting in higher EQE[2].

As described earlier in organic CW lasers (chapter 1, section 1.3.7.2), the triplet recycling via a TTA mechanism has not been reported to extend the operation period of the CW lasing. Instead, a spectral separation of the triplet absorption from the PL spectrum, triplet quenching, or scavenging to overcome the losses coming from the long-lived triplets have been used. With these techniques, triplet excitons are wasted without being properly used. In this study, I find that the triplet recycling to singlets *via* the TTA mechanism used in fluorescent OLEDs can be applicable for organic lasers to utilize detrimental triplets for efficient lasing without being wasted.

To induce both triplet scavenging and successive TTA process in laser systems, the host and guest molecules should possess certain conditions.

- First, the host molecules should possess a deeper T_1 state and a higher S_1 state compared to the guest.
- The guest molecules should possess a higher T_1 state and a lower S_1 state compared to the host molecules. Thus, all the singlets are concentrated on the guest and all the triplets are concentrated on the host.
- Upon collision of two T_1 excitons of the host material, the energy acquired by the intermediate state should be slightly higher than the S_1 energy of the host material ($2E(T_1) > E(S_1)$).

- The large difference between the T_1 energy levels of the host and the guest makes the triplet exciton transfer from the guest to the host very efficiently.
- The host molecules should have a relatively longer triplet lifetime to cause the triplet excitons to diffuse and collide with each other for a TTA process. As TTA is governed by short-range Dexter energy transfer, the longer triplet lifetime of the host is pretty important[3].
- Host should not aggregate at high concentrations.

In most reported blue fluorescent OLEDs, 9,10-di(naphtha-2-yl)anthracene (ADN) and their derivatives have been widely used since this is well-known to induce the TTA process in fluorescent OLEDs[4]. Recently, Matsushima et al.[5] showed that ADN could be used to scavenge triplets from BSBCz, and, as a result, the stability of BSBCz was remarkably enhanced. As ADN has a deep T_1, it can scavenge triplets formed in BSBCz more efficiently than other host materials. However, ADN cannot be used solely as a TTA host as it introduces a morphology problem; aggregation easily happens [6, 7]. Hence, the PLQY of the laser system degrades significantly at higher ADN concentrations, resulting in inferior laser performance[5]. That is one reason that ADN cannot be used both as a triplet scavenger and a TTA in our laser system.

Therefore, in this study, a well-known OLED blue host material of 9-(1-naphthalenyl)-10-(4-(2-naphthalenyl)phenyl)anthracene (NaNaP-A) was selected as the host in our laser devices, which can form a stable amorphous film[8, 9]. The importance of the choice of NaNaP-A in the laser devices is that it can act as a host, a scavenger, and a triplet annihilator at the same time compared to other reported host materials in qCW(ADN:Alq_3:DCM2)[6] and CW (DCNP:BSBCz)[10] regime. As the guest, a well-known sky-blue emitting organic laser dye molecule of 4,4'-bis[4-(diphenylamino)styryl]biphenyl (BDAVBi) was used[11].

4.2 Experimental

DFB Fabrication

Mixed-order DFBs were fabricated as described in chapter 2, section 2.2 under the title of *DFB Laser Device Fabrications.*

Organic Laser Device Fabrication

To complete the laser devices, a 200-nm-thick 3 wt % BDAVBi:NaNaP-A blend film was prepared on the gratings by thermal evaporation under the pressure of ~2.0×10^{-4} Pa, with a total evaporation rate of 0.1−0.2 nm s^{-1}. 0.05 ml of CYTOP (Asahi Glass) was directly spin-coated onto the laser devices at 1000 rpm for 30 s. After a sapphire lid was placed on top of the CYTOP layer, the laser device samples were dried in vacuum overnight.

Laser Characterization at qCW and CW Photoexcitation:

For long-pulse and true-CW photoexcitation, a CW laser diode (OBIS LG CW Ultraviolet Laser with a maximum power of 50 mW and an excitation wavelength of 355 nm) in combination with an acousto-optic modulator (AOM, Gooch&Housego), which was triggered with a pulse generator (WF 1974, NF) was used. The excitation light was focused on a 4.837×10^{-7} cm^2 area of the devices through a lens and slit. The excitation light was incident upon the devices at around 20° with respect to the normal to the device plane. Excitation power was controlled using a set of neutral density filters. The emitted light from the devices was collected normal to the device surface with an optical fiber connected to a multichannel spectrometer (PMA-50, Hamamatsu Photonics) and placed 3 cm away from the device. The size of the excitation area was carefully checked by using a beam profiler (WimCamD-LCM, DataRay).

Then, emission intensity was recorded using a photomultiplier tube (PMT) (C9525-02, Hamamatsu Photonics) for the measurement of the temporal emission profile. Both the PMT response and the driving square wave signal were monitored on a multichannel

oscilloscope (MSO6104A, Agilent Technologies). The same irradiation and detection angles were used for this measurement, as previously described.

OLED Fabrication and Characterization:

OLEDs were fabricated according to the device architecture of glass substrate/indium tin oxide (ITO) anode (100 nm)/α-NPD hole-transporting layer (35 nm)/3 wt % BDAVBi:NaNaP-A emitting layer (15 nm)/TPBi electron-transporting layer (65 nm)/LiF electron-injecting layer (0.5 nm)/Al cathode (80 nm). α-NPD and TPBi stand for 2,2'-dimethyl- *N*,N'-di-[(1-naphthyl) -*N*,N'-diphenyl]-1,1'-biphenyl-4,4'-diamine and 2,2',2''-(1,3,5-benzinetriyl)-tris(1-phenyl-1- *H* -benzimidazole), respectively**.** For comparison, OLEDs with a conventional host material of 4,4-bis(*N*-carbazolyl)-1,1-biphenyl (CBP) were also fabricated. Current density–voltage (*J–V*), and external quantum efficiency (EQE)–current density curves (EQE-J) were measured using an external quantum efficiency measurement system (C9920-12, Hamamatsu Photonics).

Transient electroluminescence (EL) at Long-Pulsed Voltage

20 μs long-pulsed voltages with a repetition rate of 1 kHz were generated using a voltage pulse generator and it was fed to an amplifier, as shown in Figure 4.1. The EL intensity from OLEDs operating under the pulsed voltages was recorded using a photomultiplier tube (PMT) (C9525-02, Hamamatsu Photonics) for the measurement of temporal emission profile. PMT response (CH1), driving square-wave voltage signal coming from an amplifier, which was reduced by a factor of 100 (CH2), and the voltage across the resistor (10.1 Ω) (CH3) were monitored on a multichannel oscilloscope (MSO6104A, Agilent Technologies).

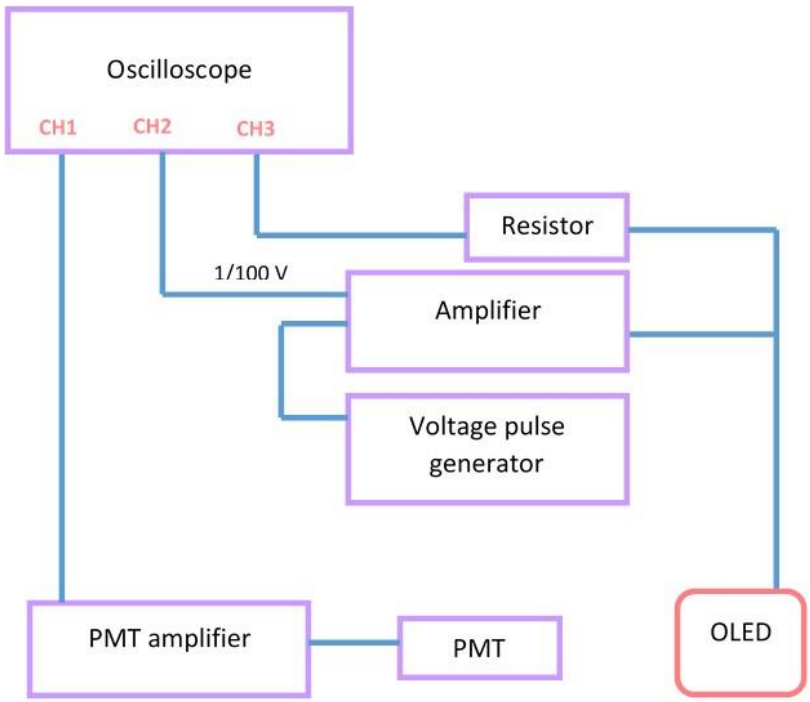

Figure 4.1. Transient EL measurement setup.

4.3 Results and discussion

4.3.1 Photophysical studies of BDAVBi and NaNaP-A

Molecular structures of BDAVBi and NaNaP-A are shown in Figure 4.2 (A). Figure 4.2 (B) depicts the absorption and PL spectra of the neat films of BDAVBi and NaNaP-A. The absorption spectrum of BDAVBi overlaps with the emission of NaNaP-A, inducing efficient FRET of the singlets from NaNaP-A to BDAVBi. To reduce concentration quenching of PL which occurs in the BDAVBi neat films, 3 wt % BDAVBi:NaNaP-A blend films were fabricated. The PL spectrum of the blend film is shown in Figure 4.2 (C) and reveals the PL coming from only BDAVBi, which again resulting from the efficient FRET from NaNaP-A to BDAVBi. For this blend film, the PLQY, prompt PL lifetime (τ), and radiative decay constant (k_r) were ~79.1%, ~1.2 ns, and ~ 6.58×10^8 s^{-1}, respectively.

Further, the triplet absorption and the kinetics of BDAVBi and NaNaP-A are essential to understand their influence on both STA and TTA mechanisms. In order to understand these behaviors, phosphorescence and triplet absorption spectra were measured in films and solution of both BDAVBi and NaNaP-A. However, we could not observe any phosphorescence or triplet absorption in films and solution. To observe phosphorescence, an ISC rate (k_{ISC}) should outcompete radiative (k_r) and nonradiative (k_{nr}) fluorescence decay rates. Moreover, a phosphorescence radiative decay rate should be larger than a nonradiative decay rate of phosphorescence. Therefore, no phosphorescence observation is probably due to a small ISC rate and/or a low phosphorescence quantum yield.

To address this problem, we used a triplet-sensitizing method using benzophenone (BP)[12]. BP has an ISC efficiency of 100% at room temperature and a very high triplet energy of 2.96 eV, which is suitable for most organic materials with triplet energies visible to the near-infrared area[12]. When BP is introduced as an additive, the absorption of light by BP yields singlets that are immediately converted into its triplets *via* ISC at nearly 100%. Then, these triplet excitons are transferred to the T_1 of the material of interest. In the solution state, benzene was used as the solvent as it helps to increase the triplet-state lifetime of the material which is eventually helpful to observe phosphorescence[13]. Because triplet lifetimes strongly depend on the solvent purity, it should be noted that triplet lifetimes should be considered as an experimentally measured quantity rather than intrinsic properties of materials[13]. With this triplet-sensitizing method, only a possible major loss channel is the direct FRET from the BP's S_1 to the S_1 of another material. However, the fast k_{ISC} ~10^{11} s^{-1} of BP suggests that an ISC rate can be competitive to FRET.

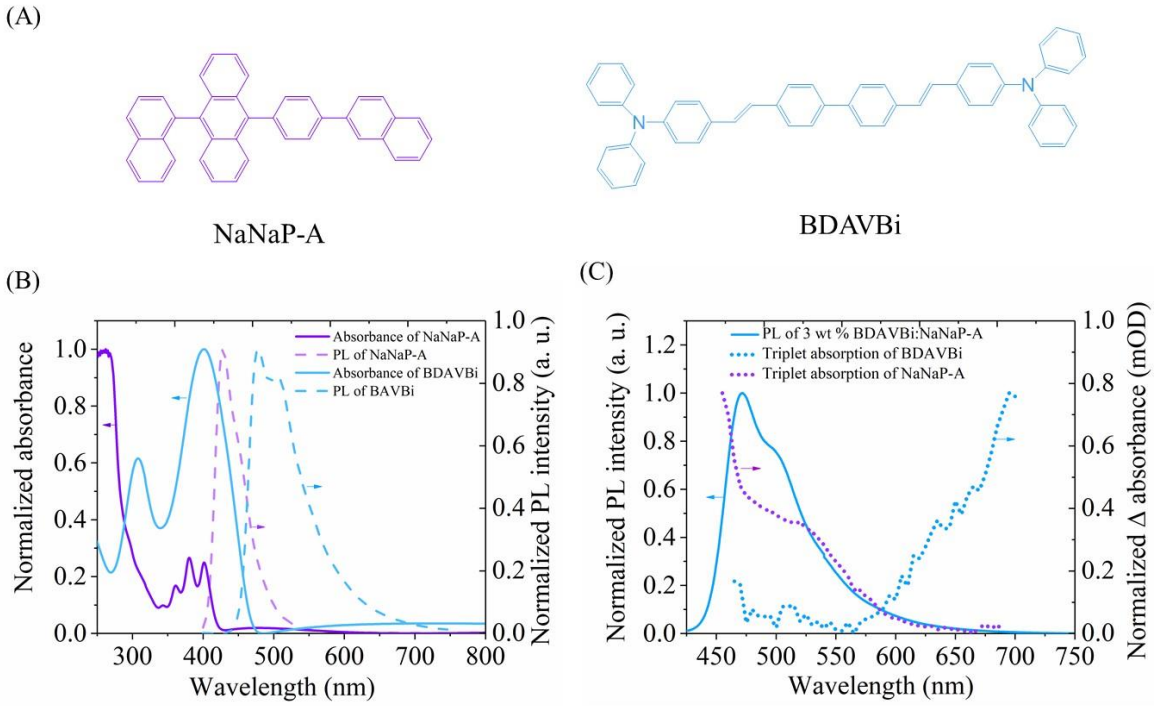

Figure 4.2. Photophysical characteristics of NaNaP-A and BDAVBi. (A) Chemical structures of NaNaP-A and BDAVBi, (B) absorption and PL spectra of neat films of NaNaP-A and BDAVBi, (C) PL spectrum of 3 wt % BDAVBi:NaNaP-A blend films and triplet absorption spectra of BDAVBi and NaNaP-A in benzene solution with the BP sensitization.

Using this method, we were able to measure the triplet absorption of BDAVBi and NaNaP-A, as shown in Fig. 4.2 (C). According to the triplet absorption spectra, the BDAVBi's PL spectrum has a large overlap with the NaNaP-A's triplet absorption spectrum. These results indicate that strong STA in BDAVBi with NaNaP-A may happen in this system when long-pulse excitation or CW excitation was used for the operation of organic lasers. On the other hand, BDAVBi has a very small overlap of its triplet absorption at its emission wavelengths, as shown in Fig. 4.2 (C), which may induce very weak STA. However, STA which occurs between BDAVBi and NaNaP-A can be suppressed by NaNaP-A molecules by scavenging and then recycling these long-lived triplets *via* its deep T_1 state.

4.3.2 Fabrication DFB lasers

A mixed-order DFB structure was introduced in the laser devices by incorporating both first-order (12 periods) and second-order (four periods) periods to reduce radiation loss. In this structure, lasing occurs *via* second-order DFB structures, as explained in chapter 1, section 1.4.1. The period values for the first-order (m = 1) and the second-order (m = 2) gratings used in our mixed-order DFB structure were calculated using the Bragg equation, and the values were 128 and 256 nm, respectively. λ_{Bragg} and n_{eff} values used for the calculation were 487 nm and 1.9047, which were estimated from an amplified spontaneous emission (ASE) wavelength and an ellipsometry measurement, respectively. The grating depth of the DFBs was around 65 nm, and the area of the grating was 1.3×1.3 mm^2. A 200-nm-thick layer of 3 wt % BDAVBi:NaNaP-A was vacuum-deposited on top of the DFBs. The fabricated laser devices were encapsulated with a CYTOP layer and a sapphire substrate under a nitrogen environment to suppress molecular degradation associated with a temperature rise inside devices under long-pulse photoexcitation[14].

4.3.3 Laser studies under long-pulse photoexcitation

Long pulses of 10 µs, 100 µs, 1000 µs, and 10 ms were used to excite the laser devices using 355 nm CW laser diode. Figure 4.3 (A) shows the laser emission profile when increasing the excitation intensity under 10-ms long-pulse photoexcitation, with the inset showing the laser emission obtained at high resolution. When laser devices were excited with a long pulse of 10 ms, we could observe a characteristic dip appearing in the PL spectrum below a lasing threshold, as shown in Figure 4.3 (B). This dip corresponds to the photonic bandgap of the fabricated DFB structure, which indicates that the PL emission outcouples *via* the DFB resonator. The inset of Figure 4.3 (B) shows a photograph of the laser emission from a laser device. The FWHM of the laser emission under long-pulse photoexcitation was ~ 2.5 nm, which points to the temporal coherence of the emitted laser beam. Laser E_{th} was calculated from the change in slope of the emission intensities in Figure 4.3 (C).

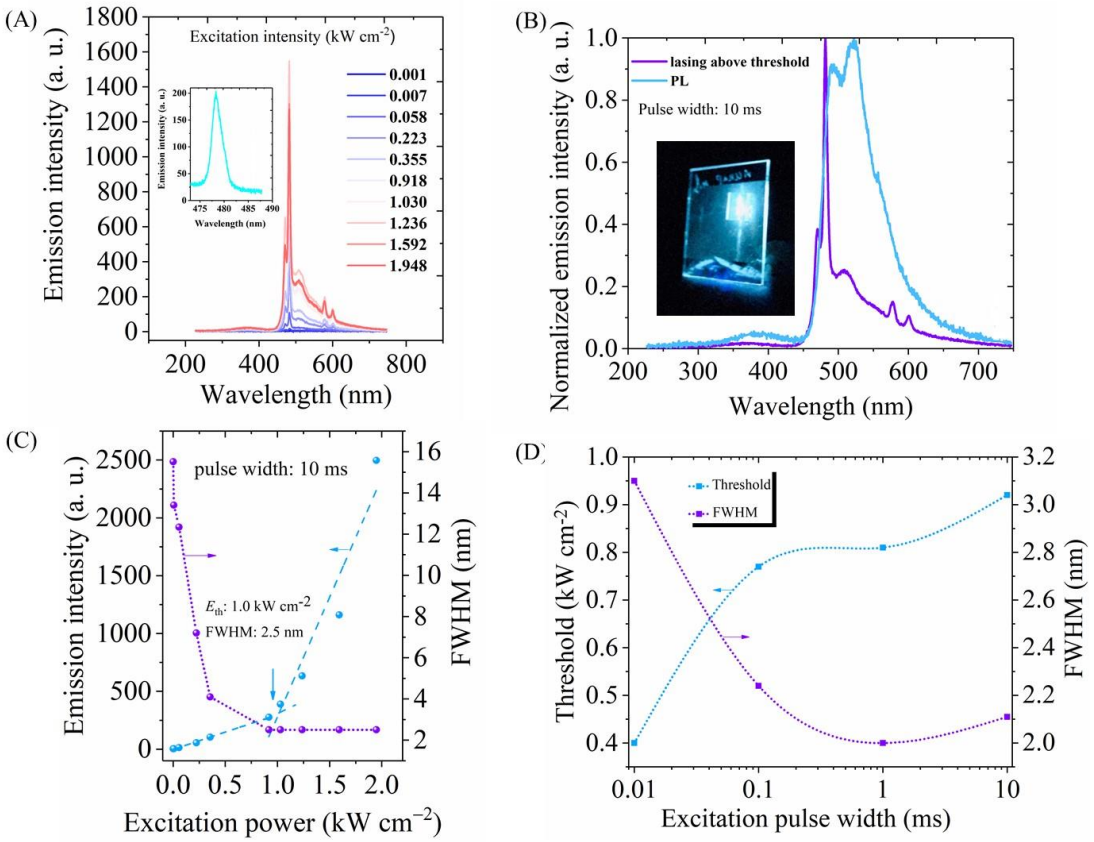

Figure 4.3. Lasing under long-pulse photoexcitation from 3 wt % BDAVBi:NaNaP-A films. (A) PL spectra of BDAVBi:NaNaP-A laser devices, which were measured under 10 ms long-pulse photoexcitation. The inset shows the laser emission spectrum at high resolution. (B) PL spectra measured below and above the laser threshold under 10 ms long-pulse photoexcitation, and the inset shows a photograph taken above the laser threshold. (C) Plots of emission intensity or FHWM as a function of excitation power. (D) Plots of laser emission thresholds and FWHM values as a function of excitation pulse width.

When going from the 10 µs pulse width to the 10 ms pulse width, a slight increase in lasing threshold was observed, as shown in Figure 4.3 (D). Although we expect a threshold decrement under longer pulses as triplet contribution becomes high, we did not observe such a decrement. Under photoexcitation, the triplet contribution is not significant to alter the threshold values in the laser devices. Therefore, we can attribute this behavior to material degradation when using longer excitation pulse widths compared to shorter excitation pulse

widths. Because longer the pulse, prolonged intense excitation tends to degrade the organic molecules. Further, there is a slight decrease of FWHM when going from shorter-pulse (0.01 ms) to longer-pulse (1 ms) photoexcitation, the reason for which is not still clear. However, a slight increase in FWHM was observed when pulse widths get longer than 10 ms, possibly because of the material degradation.

Moreover, we were able to obtain lasing under long-pulse photoexcitation with pulse widths of up to 10 ms, which is much longer than the triplet lifetimes of BDAVBi (1.1 µs) and NaNaP-A (144 µs) (see Figure 4.4). It should be noted that these triplet lifetimes measured in solution may be different from those measured in films. These results indicate that the STA is suppressed in our laser system because the detrimental triplets are scavenged and recycled by NaNaP-A. This long-pulse photoexcitation is difficult for normal organic laser devices, in which STA happens.

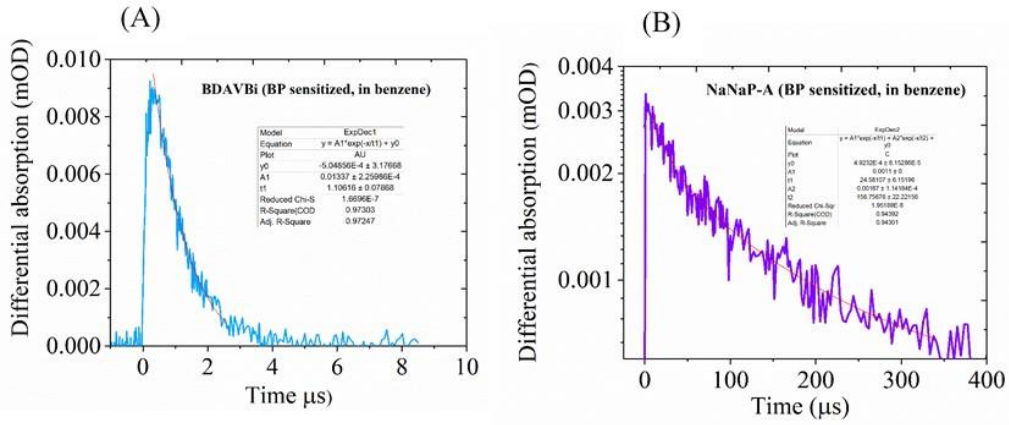

Figure 4.4. Triplet lifetimes obtained from transient absorption spectra carried out by sensitizing with BP in benzene solution**.** (a) Average triplet lifetime of BDAVBi at 690 nm (~ 1.1 µs) and (b) average triplet lifetime of NaNaP-A at 460 nm (~ 144 µs). The solid lines are the fitting results used to estimate the triplet lifetimes

Figure 4.5 shows the excited-state energy diagram of NaNaP-A and BDAVBi system which explains the mechanism of the triplet scavenging and the triplet recycling for efficient qCW lasing.

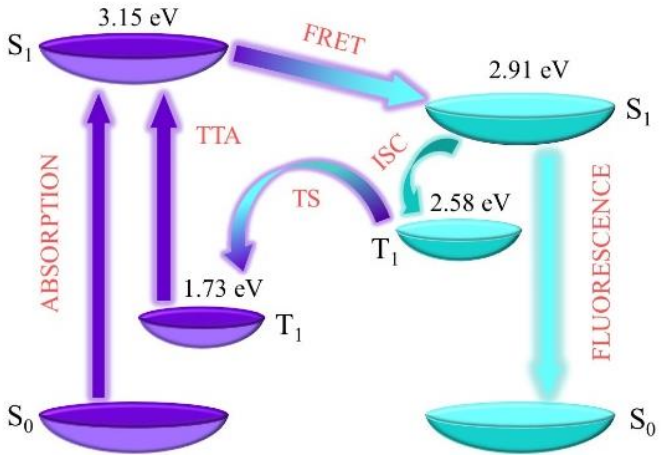

Figure 4.5. Triplet scavenging and triplet recycling in BDAVBi:NaNaP-A films. Energy-level diagram of NaNaP-A and BDAVBi (TTA = triplet-triplet annihilation, TS = triplet scavenging, ISC = intersystem crossing, and FRET = Förster energy transfer).

The respective S_1 energies of BDAVBi and NaNaP-A were obtained from the fluorescence spectra of Figure 4.2 (B). The T_1 energy of BDAVBi was estimated from the phosphorescence spectrum shown in Figure 4.6. For the phosphorescence measurement, BP was incorporated as the triplet sensitizer as explained before. To investigate the T_1 position of NaNaP-A, phosphorescence measurement was carried out. Unfortunately, it was not successful. Therefore, T_1 state of NaNaP-A was calculated. For the calculations, the geometry of the S_0 state of NaNaP-A in the gas phase was optimized using Becke's three-parameter hybrid functional employing the LYP (Lee–Yang–Parr) correlation functional (B3LYP) with 6-31G(d) basis set. According to the calculated results, the T_1 energy of the NaNaP-A is 1.73 eV. Moreover, this calculated value matches most of the reported anthracene derivatives' triplet energy state [15, 16]. The calculated S_1 energy of the NaNaP-A was 3.15 eV. The experimentally determined S_1 energy of the NaNaP-A using the fluorescence spectra given in Figure 4.2 (B) is 3.12 eV which is well aligned with the calculated results. Now the energy of the two triplets is 3.46 eV (1.73 × 2 eV) which is slightly above the S_1 state of NaNaP-A as shown in **Figure 4.5**. This satisfies the condition to occur TTA in this laser system. As shown in Figure 4.5, NaNaP-A was first photoexcited

and the formed excited singlets were transferred to the BDAVBi's S_1 *via* FRET, which is caused by the overlap of the fluorescence spectrum of NaNaP-A and the absorption spectrum of BDAVBi. The transferred singlet excitons on BDAVBi follow two paths. A fraction of the singlets is converted into the triplets *via* ISC, while the other fraction relaxes to the ground state *via* the radiative process by emitting fluorescence. The triplets formed on BDAVBi are scavenged by NaNaP-A because of their deep T_1 energy (~1.73 eV). The triplet scavenging by NaNaP-A is more efficient in the system as the gap between the T_1 energy (~2.58 eV) of BDAVBi and the T_1 energy (~1.73 eV) of NaNaP-A is large. The triplet excitons of NaNaP-A diffuse through the layer and collide relative to each other, probably inducing TTA via Dexter energy transfer. With this TTA process, the high-energy singlet excitons are formed on NaNaP-A by colliding two low-energy triplets. Eventually, these singlets are transferred to the low-lying S_1 state of BDAVBi.

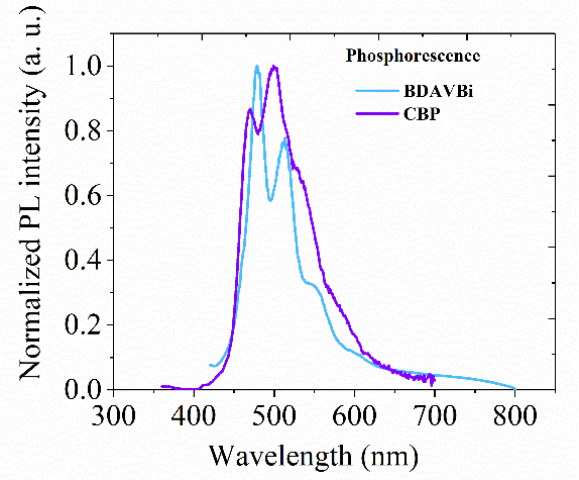

Figure 4.6. Phosphorescence spectra of BDAVBi and CBP taken in BP sensitized benzene solution.

To confirm the TTA process in the NaNaP-A:BDAVBi films, the transient photoluminescence (PL) spectra using a streak camera was obtained. In 50 μs time window a delayed emission coming from the 3 wt % BDAVBi:NaNaP-A film could be observed as shown in Figure 4.7 which evidences the existence of the TTA process in this laser system.

The PL decay curve was well fitted with the TTA model given in equation 1, claiming that the delayed emission is merely coming from TTA[17].

$$I(t) = \left[\frac{A\,exp(-\frac{t}{\tau_T})}{1+B\,[1-\exp(\frac{-t}{\tau_T})]}\right]^2 \qquad (1)$$

where, A is the proportionality constant, B is the bimolecular annihilation rate, τ_T is the monomolecular decay rate, and t is the time.

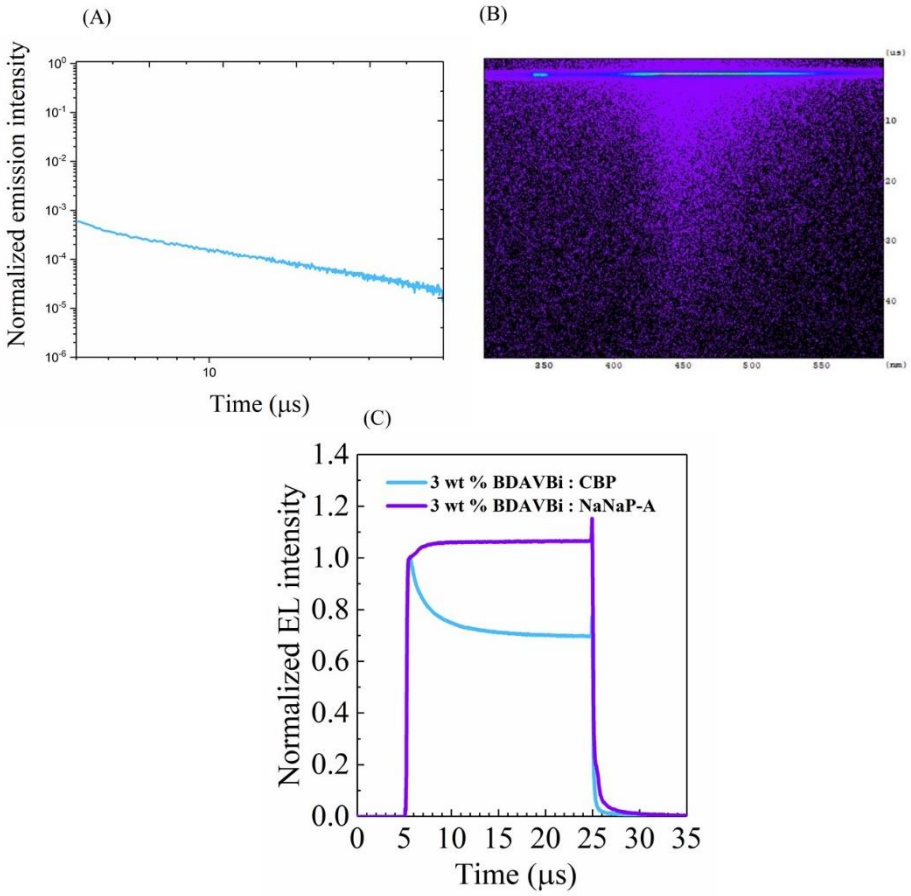

Figure 4.7. Evidence of TTA mechanism of BDAVBi:NaNaP-A films**.** (A) Transient PL decay curve, (B) corresponding streak camera image of the delayed emission taken in the time window of 50 μs and integrated over 10,000 pulses, and (C) EL responses of OLEDs based on BDAVBi:NaNaP-A and BDAVBi:CBP emitter under 20 μs pulse width electrical excitation.

To clarify the aforementioned triplet recycling process occurring in the laser devices, OLEDs were fabricated to measure transient EL. According to spin statistics, the number of triplets formed under electrical excitation in OLEDs is three times compared to photoexcitation. Therefore, if triplets are recycled efficiently in BDAVBi:NaNaP-A films, delayed EL after the device is turned off can be observed.

A blend film of 3 wt % BDAVBi:CBP has a PLQY of 79.5%, which is similar to that of a 3 wt % BDAVBi:NaNaP-A film as discussed earlier. However, unlike in 3 wt % BDAVBi:NaNaP-A films, a 3 wt % BDAVBi:CBP film undergoes severe STA as BDAVBi has an overlap of its emission spectrum with a triplet absorption spectrum of CBP as shown in Figure 4.8 (A) and does not include the triplet recycling process (see Figure 4.8 (B) for the excited-state energy diagram of CBP and BDAVBi). When CBP is excited, the singlet excitons generated on CBP are transferred to the S_1 state of BDAVBi *via* the FRET mechanism. Then, a fraction of singlet excitons on BDAVBi decays to the ground state by emitting light, while some fraction of singlet excitons is converted into the T_1 state of BDAVBi *via* ISC. However, the T_1 (2.60 eV, obtained from phosphorescence spectrum shown in Figure 4.6) state of CBP is not deep enough to scavenge long-lived triplets of BDAVBi (T_1 = 2.58 eV) like in NaNaP-A (T_1=1.50 eV).

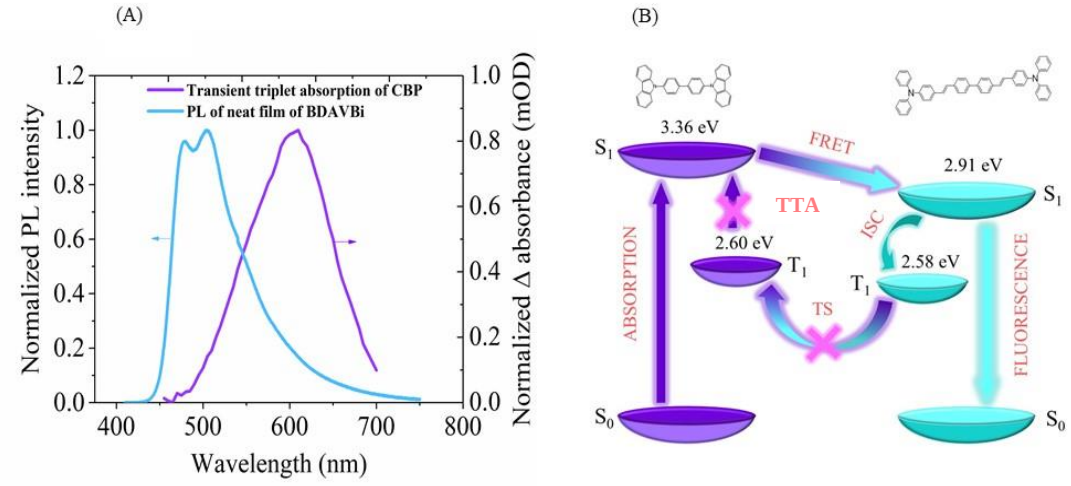

Figure 4.8. Photophysical characteristics of BDAVBi and CBP and energy transfer mechanism of BDAVBi:CBP films. (A) PL spectrum of BDAVBi neat film and transient triplet absorption of CBP in BP sensitized benzene solution and (B) energy-level diagram of CBP and BDAVBi (TTA = triplet-triplet annihilation, TS = triplet scavenging, ISC = intersystem crossing, and FRET = Förster energy transfer).

The measured transient EL properties of both devices under 20 µs pulse width are shown in Figure 4.7 (C). The BDAVBi:CBP-based OLED showed a quick decay of EL after the device was turned on because of strong STA. However, BDAVBi:NaNaP-A-based OLED did not show such an EL decay profile under 20 µs pulse width when the device is turned on. Instead, the TTA increased the EL intensity. This proved that STA is well mitigated by the proposed triplet scavenging mechanism in our BDAVBi:NaNaP-A-based OLED. Later, when both devices were turned off, delayed emission was observed only in BDAVBi:NaNaP-A-based OLED. This is one proof of the triplet recycling induced by NaNaP-A. Similar behavior was not observed in BDAVBi:CBP-based OLEDs, proving that only STA is governed in this device. Moreover, as CBP does not have a deep T_1 (2.60 eV) state to scavenge the long-lived triplets, CBP-based OLED is prone to induce STA[10, 18].

The other OLED properties are shown in Figure 4.9. EQE vs. current density characteristics of CBP-based OLED revealed a severe EQE rolloff at high current densities, which would be induced by STA. However, NaNaP-A-based OLED did not show such

behavior at a high current density region, since triplets are efficiently scavenged and successively upconverted into singlets. At low current densities, EQEs were lower in NaNaP-A-based OLED than in CBP-based OLED. This may be due to a lower carrier injection balance factor in NaNaP-A-based OLED. Further optimization of NaNaP-A-based OLED architectures will increase the carrier balance and, therefore, provide higher EQE in the future.

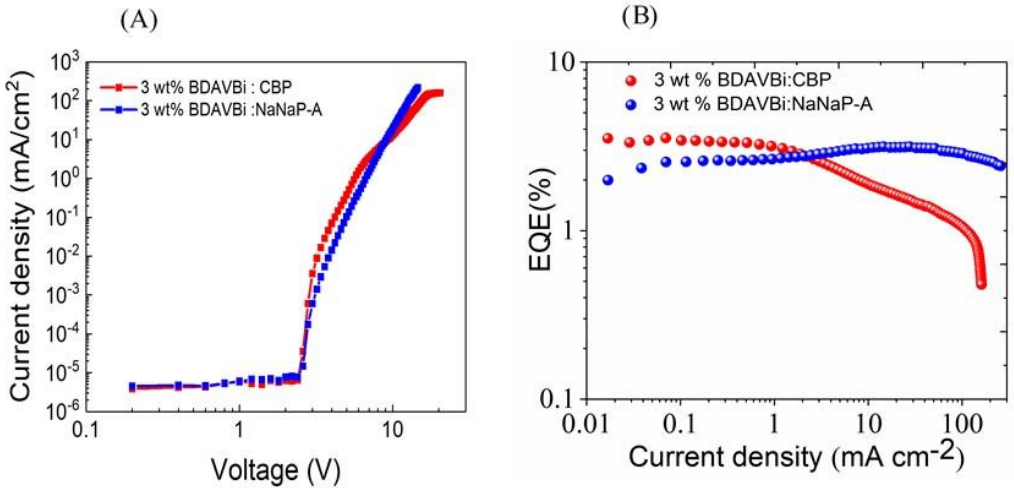

Figure 4.9. OLED device performance**.** (A) Current density vs. voltage graphs of OLEDs based on BDAVBi:NaNaP-A and BDAVBi:CBP emitter and (B) EQE vs current density graphs.

In addition, simulations were carried out to investigate the possibility of the lasing in the BDAVBi:NaNaP based devices. Following four rate equations were written for each step considering the processes involves in each level shown in Figure 4.10**.**

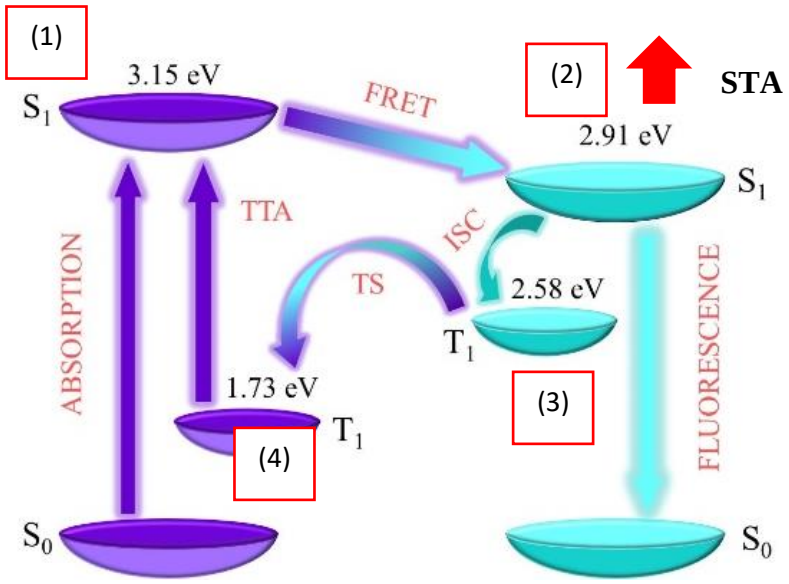

Figure 4.10. BDAVBi:NaNaP-A laser mechanism with four main states considered for the simulations.

State1: HOST- Singlet exciton rate equation

$$\frac{\partial n_{s1H}(x,t)}{\partial t} = G - n_{s1H}k_{FRET} + 0.25k_{TTA}n_{T1H}^2 \qquad (2)$$

where G is the rate of generation of singlet excitons, n_{s1H} is the singlet exciton density of the host, k_{FRET} is the Förster energy rate constant, k_{TTA} is the TTA rate constant, and n_{T1H} is the host triplet exciton density.

1st term = Generation of triplets

2nd term = Host singlet exciton density loss via FRET

3rd term = Generated singlet exciton density via TTA on host

State 2: GUEST- Singlet exciton rate equation

$$\frac{\partial n_{s1G}\,(x,t)}{\partial t} = n_{s1H}K_{FRET} - \frac{\partial\, n_{s1G}(x,t)}{\partial t}|stim - k_{STA}n_{s1G}n_{T1H} - k_{ISC}n_{s1G} \quad (3)$$

where, n_{s1G} is the guest singlet density, k_{STA} is the rate constant of STA, and k_{ISC} is the rate constant of ISC

1st term = Transferred singlet exciton density from host to guest via FRET

2nd term = Singlet exciton density loss via stimulated emission

3rd term = Singlet exciton density loss via STA with host triplet exciton density

4th term = Singlet exciton loss due to ISC

Sate 3: GUEST- triplet exciton rate equation

$$\frac{\partial n_{T1G}\,(x,t)}{\partial t} = k_{ISC}n_{s1G} - k_{ET}n_{T1G} \quad (4)$$

where, n_{T1G} is the triplet density of the guest, and k_{ET} is the rate constant of the energy transfer from the T1 state of the guest to the T1 state of the host

1st term = Generation of triplet excitons density via ISC from S1 state of the guest

2nd term = Loss of guest triplet excitons via energy transfer to the host triplet state

State 4: HOST- triplet exciton rate equation

$$\frac{\partial n_{T1H}\,(x,t)}{\partial t} = k_{ET}n_{T1G} - (0.25)k_{TT}n_{T1H}^2 \quad (5)$$

1st term = Filling up of host triplet exciton density via scavenging guest triplet excitons

2nd term = Loss of triplet density of the host via TTA

Then the simulations were carried out under four conditions as follows.

1. When there is no both STA and TTA mechanisms involved in the system
2. When there is STA and no TTA mechanisms involved in the system
3. When there is no STA and there is TTA mechanisms involved in the system
4. When there are both STA and TTA mechanisms involved in the system and $k_{STA} < k_{TTA}$

1. When there is no both STA and TTA mechanisms involved in the system

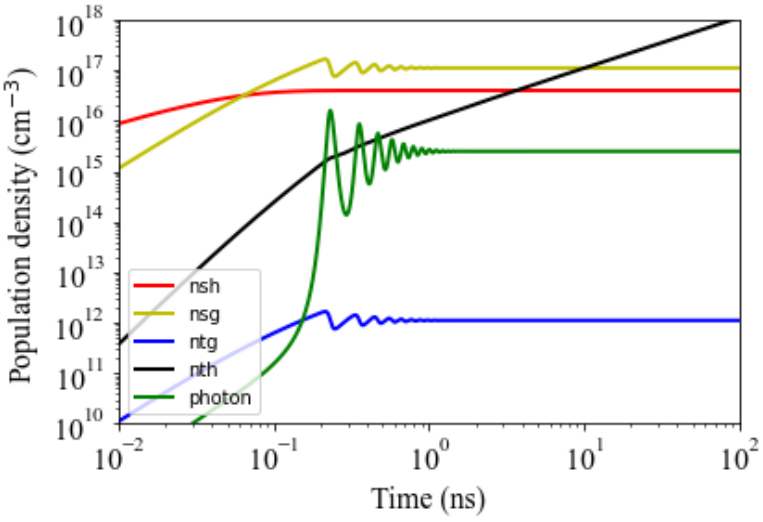

Figure 4.11. Population density vs. time graph

In this graph n_{sh} is the singlet density of host, n_{sg} is the singlet density of guest, and n_{tg} is the triplet density of guest, n_{th} is the triplet density of host. As can be seen in this Figure 4.11, host triplet density (black) increases with time due to scavenging triplets formed on Guest. Guest triplet density (blue) stays constant as it is constantly filled with guest singlets and constantly removed via host triplet state. But it does not affect the system as there is no STA and TTA in the system. Singlet densities of host and guest (red and yellow) stayed constant due to constant generation and transfer via FRET. Then system achieves laser oscillation (green) condition due to constant generation of singlets exciton density on the guest.

2. When there is STA and no TTA mechanisms involved in the system

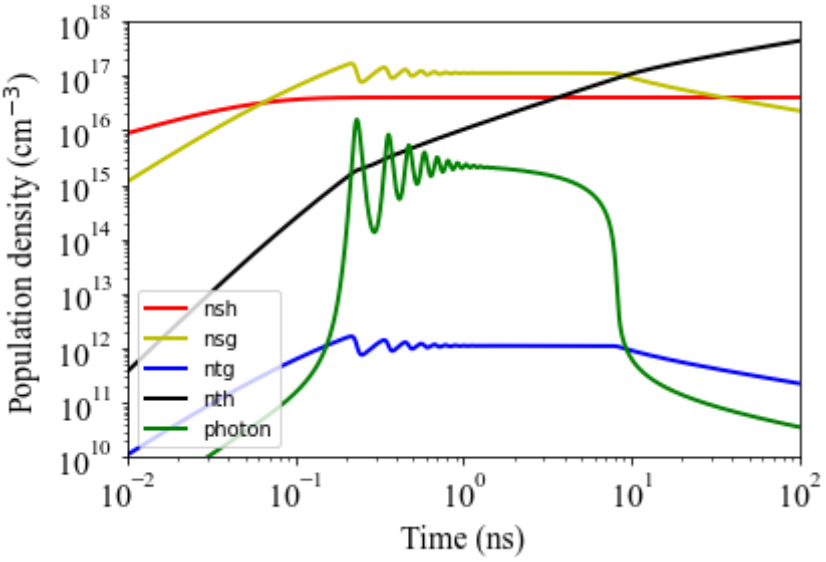

Figure 4.12. Population density vs. time graph

When there is STA, and no TTA component in the system, lasing (green) stops after some time when triplet density of host (black) increases and singlet density of guest decreases (yellow) due to STA (due to host triplet density and guest singlet density). Triplet density of guest (blue) goes down when singlet density goes down due to STA as it is the only filling mechanism of the guest triplet state via ICS. Host singlet density (red) stays constant due to the constant generation of singlet excitons.

3. When there is no STA and there is TTA mechanisms involve in the system

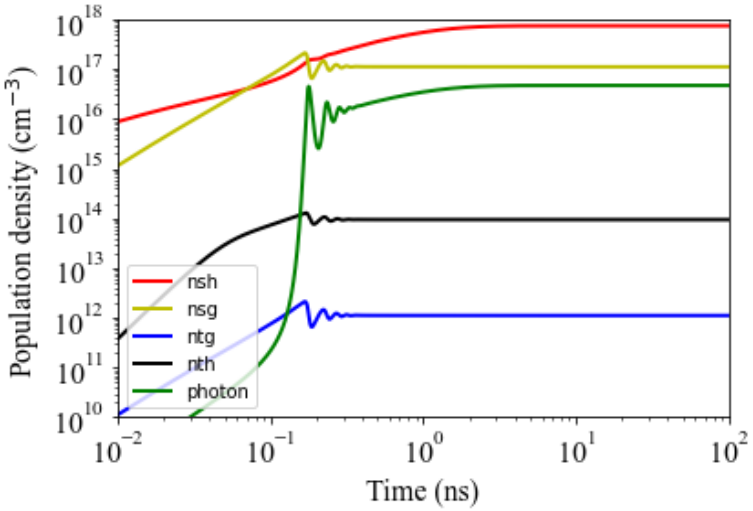

Figure 4.13. Population density vs. time graph.

When the absence of STA and the presence of TTA in the system, the triplets of the host (black) do not accumulate as in the previous cases. Because these triplets will lose from the host via TTA. As a result, singlets of the host will eventually increase (red), as shown in Figure 4.13. The guest triplets appear constant as constant scavenging and TTA take place in the system. Moreover, after some time, photon density increases in the system due to the TTA process.

4. When there are both STA and TTA mechanisms involved in the system and $k_{STA} < k_{TTA}$

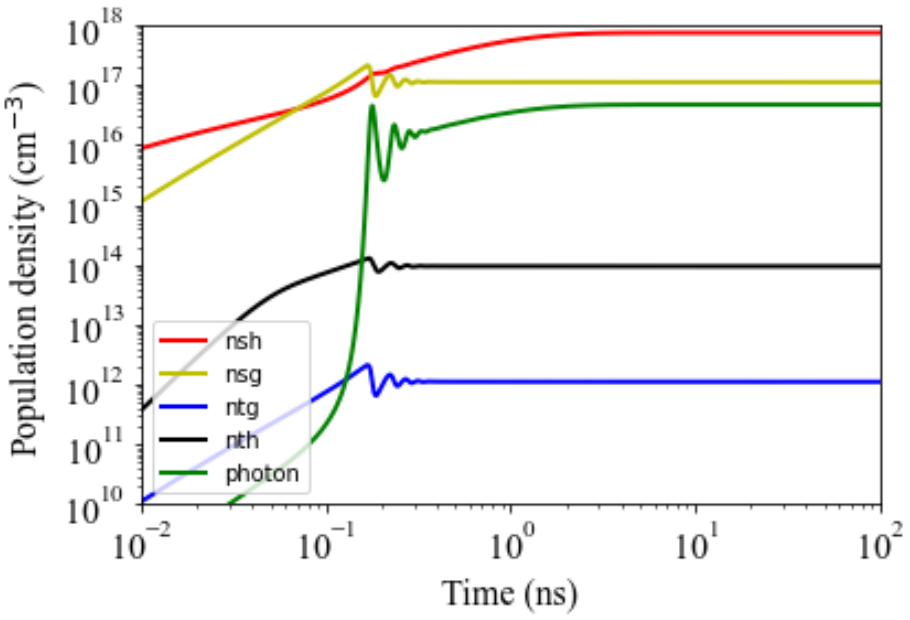

Figure 4.14. Population density vs. time graph.

In the presence of both STA and TTA, the system works similarly to the previous condition. However, k_{STA} should be smaller than the k_{TTA} to work the system properly. There is a slight decrease of the photon density in the system than in the previous case as this system includes STA.

Hence from these results, conclusion can be made even in the presence of STA, fast k_{TTA} contributes to efficient lasing in this laser system.

Further, a reference laser device with CBP as the host which has strong STA due to the overlap of TA of CBP with the PL of BDAVBi was fabricated. However, CBP does not meet the TTA condition to recycle triplet excitons to singlet excitons. The BDAVBi:NaNaP-A system has both STA with TTA. Then, both of these laser devices were excited with the same excitation power under 10 ms pulse width. Then, the BDAVBi:NaNaP-A system showed

laser amplification. Thus, STA must have compensated by TTA for these devices. But BDAVBi:CBP device barely showed lasing due to strong STA, as shown in Figure 4.15 below.

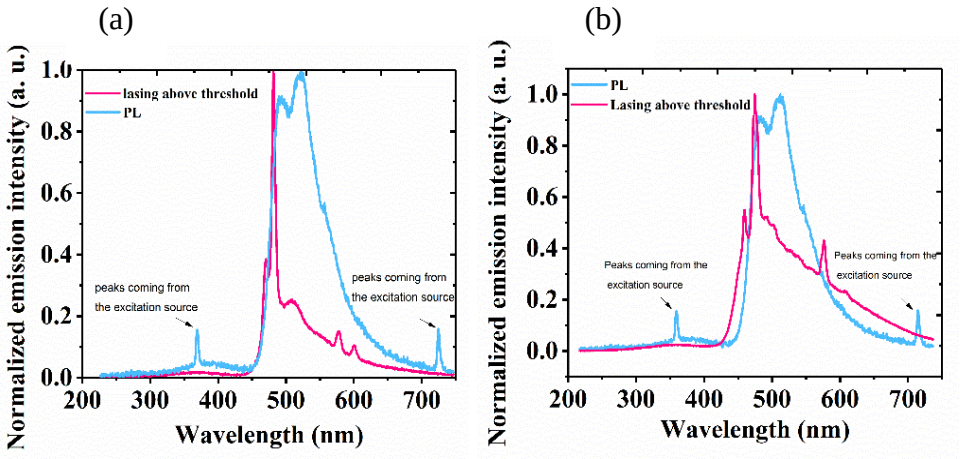

Figure 4.15. Laser emission profile of (a) BDAVBi:NaNaP-A and (b) BDAVBi:CBP laser devices at 10 ms qCW photoexcitation at 1.6 kW cm^{-2}.

4.4 Conclusions

In summary, I investigated the possibility of using detrimental triplets efficiently for long-pulse lasing, instead of scavenging them from the laser medium. To achieve this, triplet scavenging and then triplet recycling *via* TTA were used to regenerate radiative singlets in the laser medium using an amorphous anthracene derivative of NaNaP-A as the host and the laser dye BDAVBi as the guest. The deep triplet state of NaNaP-A facilitates triplet scavenging from BDAVBi and then triplet recycling *via* a TTA mechanism. Although these films do have a spectral overlap of the triplet absorption of NaNaP-A with the emission of BDAVBi, STA is not significant in these films as the triplet scavenging and triplet recycling compensate the STA-induced exciton losses. As a result, our laser device could operate at 10 ms of long-pulse photoexcitation. Finally, the triplet recycling mechanism was successfully claimed from the observation of the delayed PL and EL, the increased EL intensity during

the excitation and simulation results. Since the number of triplets generated under electrical excitation is much larger compared to optical excitation, the triplet recycling concept can be used to realize future electrical lasing from organics as well.

References

[1] K. Okumoto, H. Kanno, Y. Hamada, H. Takahashi, K. Shibata, *Appl. Phys. Lett*., **2006**, *89*, 063504.

[2] R. Ieuji, K. Goushi, C. Adachi, *Nat. Commun*., **2019**, *10*, 5283.

[3] T. N. S. Rachford, F. N. Castellano, *Coord. Chem. Rev*., **2010**, *254***,** 2560.

[4] J. Huang, J.-H. Su, H. Tian, *J. Mater. Chem.,* **2012***, 22,* 10977.

[5] T. Matsushima, S. Yoshida, K. Inada, Y. Esaki, T. Fukunaga, H. Mieno, N. Nakamura, F. Bencheikh, M. R. Leyden, R. Komatsu, C. Qin, A. S. D. Sandanayaka, C. Adachi, *Adv. Funct. Mater.,* **2019***, 29*, 1807148.

[6] Y. Zhang, S. R. Forrest, *Phys. Rev. B - Condens. Matter Mater. Phys.,* **2011***, 84*, 241301.

[7] J. Y. Song, S. B. Lee, S. J. Lee, Y. K. Kim, S. S. Yoon, *Thin Solid Films,* **2015**, *577*, 42.

[8] J. H. Jeon, S. Ji. Cha, Y. M. Jeon, Ji. H. Lee, M. C. Suh, *Org. Electron.,* **2014***, 15*, 2802.

[9] T. Sato, T. Miyamae, H. Ohata, T. Tsutsui, *Org. Electron.,* **2019**, *74*, 118.

[10] B. S. B. Karunathilaka, U. Balijapalli, C. A. M. Senevirathne, Y. Esaki, K. Goushi, T. Matsushima, A. S. D. Sandanayaka, C. Adachi, *Adv. Funct. Mater.,* **2020***, 30*, 2001078.

[11] M. Inoue, T. Matsushima, C. Adachi, *Appl. Phys. Lett.,* **2016**, *108*, 133302.

[12] S. Reineke, M. A. Baldo, *Sci. Rep.*, **2014**, *4*, 3797.

[13] W. D. K. Clark, A. D. Litt, C. Steel, *J. Am. Chem. Soc.*, **1969**, *91*, 5413.

[14] A. S. D. Sandanayaka, T. Matsushima, F. Bencheikh, K. Yoshida, M. Inoue, T. Fujihara, K. Goushi, J-C. Ribierre, C. Adachi, *Sci. Adv.*, **2017**, *3*, e1602570.

[15] X. He, S. Ren, H. Liu, S. Zhao, F. Liu, C. Du, J. Min, H. Zhang, P. Lu, *Chem. Asian J.*, **2020,** *15*, 163.

[16] N. Sharma, M. Y. Wong, D. Hall, E. Spuling, F. T. Carmona, A. Privitera, G. Copley, D. B. Cordes, A. M. Z. Slawin, C. Murawski, M. C. Gather, D. Beljonne, Y. Olivier, I. D. W. Samuel, E. Z.-Colman, *J. Mater. Chem. C*, **2020**, *8*, 3773.

[17] B. H. Wallikewitz, D. Kabra, S. G´elinas, R. H. Friend, *Phys. Rev. B*, **2012**, *85*, 045209.

[18] D. H. Kim, A. D'Aléo, X. -K. Chen, A. D. S. Sandanayaka, D. Yao, L. Zhao, T. Komino, E. Zaborova, G. Canard, Y. Tsuchiya, E. Choi, J. W. Wu, F. Fages, J. L. Brédas, J. C. Ribierre, C. Adachi, *Nature Photon.*, **2018**, *12*, 98.

Chapter 5

Conclusions and Perspective

5.1 Conclusions

My work presented in this thesis mainly focuses on achieving low-threshold and high-stability optically pumped qCW/ CW lasing from organic semiconductor laser materials by suppressing the STA and thermal degradation. In this regard, I obtained the following findings:

In **Chapter 2**, I reported the first lasing from a solution-processed small-molecule BSFCz organic semiconductor in a long pulse photoexcitation regime (up to 10 ms in pulse width), with a low threshold of 420 W cm^{-2}. I attributed the existence of laser emission under long-pulse photoexcitation in the new BSFCz laser dye to the negligible spectral overlap between the triplet absorption and the laser emission. This was further confirmed by temporal emission profiles below and above the lasing threshold, which indicates negligible STA. Moreover, I showed that the qCW laser emission was more stable compared to most of the reported laser materials operating in the qCW/CW laser regime.

In **Chapter 3**, I was able to show that high-quality 2D resonator structures can be implemented to obtain CW lasers by reducing the laser oscillation threshold. A decrease in laser threshold suppresses the thermal degradation and, therefore, leads to long-lasting lasing from organic laser dyes. Here, I showed that it is possible to decrease the laser thresholds by combining an organic laser dye of BSBCz, which has no spectral overlap between the laser emission and the excited-state triplet absorption, with 2D DFB gratings. I used second-order 2D cross double and square lattice DFB gratings, which offer the light feedback in two orthogonal directions, and second-order and mixed-order circular DFB gratings, which offer the light feedback in radial directions. Among these grating structures, the mixed-order circular DFB grating structure led to the lowest lasing threshold of ~0.015 μJ cm^{-2} under short-pulse photoexcitation because of the excellent optical feedback. Moreover, a very low laser threshold of ~10 W cm^{-2} was obtained when laser devices with this grating structure were operated with 1 s of long-pulse photoexcitation. Additionally, the mixed-order circular DFB grating structure improved the laser stability under CW photoexcitation since shorter exciton lifetimes in the optical resonator suppress the chemical decomposition. These results

demonstrate the importance of choosing an optical resonator structure for improving organic laser performance.

In **Chapter 4,** I investigated the possibility of using detrimental triplet excitons for CW lasing *via* the TTA-induced TU. Using this method, triplet excitons can be provided back to the emissive singlet state without diminishing laser action. An anthracene derivative of NaNaP-A and a laser dye of BDAVBi were used as the triplet recycling host and laser dye, respectively, in our laser system. In this laser system, since the triplet absorption spectrum of NaNaP-A overlaps with the singlet emission spectrum of BDAVBi, normally strong STA happens. However, we found that NaNaP-A can efficiently scavenge the triplets formed on BDAVBi because of the deeper triplet level than that of BDAVBi, and successively recycle them into the BDAVBi's singlet state *via* TU. This TU by NaNaP-A compensates the possible STA in this laser system. As a result, I was able to operate our laser devices with long pulse widths of up to 10 ms or CW photoexcitation.

In summary, I was able to show three new strategies to obtain CW lasing. One strategy has not been studied before and is the first-ever demonstration of qCW laser emission from solution-processed small molecule organic semiconductor films with the negligible spectral overlap of the triplet absorption and the emission spectrum. Second, I could show the important role played by the resonator structures in CW laser performance, particularly in reducing laser threshold via increased feedback and high photon confinement provided by 2D grating structure. Third, I showed long-lived triplet excitons could be recycled via a TTA mechanism to use them in CW lasing.

5.2 Perspective

As I discussed in this thesis, there are several strategies that can be implemented to obtain CW lasing. However, there are plenty of other aspects in CW regime that can still be improved such as stability. In this regard, I am proposing a concept of using a biluminescent material as a donor molecule in combination with a proper acceptor molecule with spectral overlap to occur energy transfer to use in CW lasing. In a proper biluminescent host-guest system, FRET from the host's singlet state to the guest's singlet state and from the host's triplet state to the guest's singlet state occurs as depicted in Figure 5.1 below[1]. For example, [*N*,*N*′-di(naphtha-1-yl)-*N*,*N*′-diphenylbenzidine] (NPB), which is embedded in a rigid polymer matrix of polymethylmethacrylate (PMMA) to suppress nonradiative depopulation of triplets, is combined with a red-emitting laser dye molecule of [4-(dicyanomethylene)-2-tert-butyl-6-(1,1,7,7-tetramethyljulolidyl-9-enyl)-4H-pyran] (DCJTB)[1].

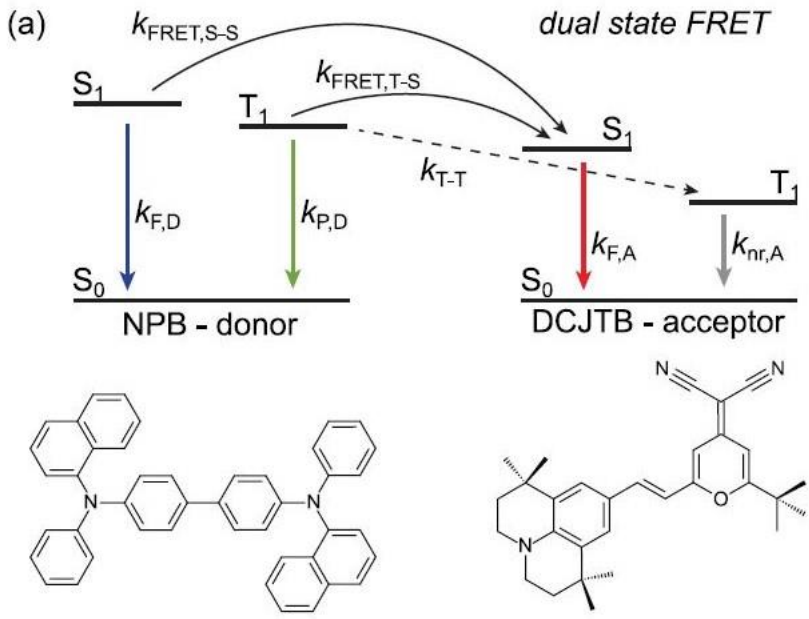

Figure 5.1. Dual state FRET mechanism with NPB and DCJTB[1].

This will reduce concentration quenching as well as it enhances the molecular distance. DCJTB has a spectral overlap of its absorption spectrum with fluorescence and phosphorescence spectra of NPB which facilitate efficient energy transfer, as shown in Figure

5.2. However, in CW regime, the selection of an acceptor molecule with spectral separation of triplet absorption and fluorescence is beneficial to avoid STA. Although this concept is promising for CW lasers, the choice of emitter molecule is not very appropriate as it has a moderate spectral overlap of triplet absorption and emission spectra[2].

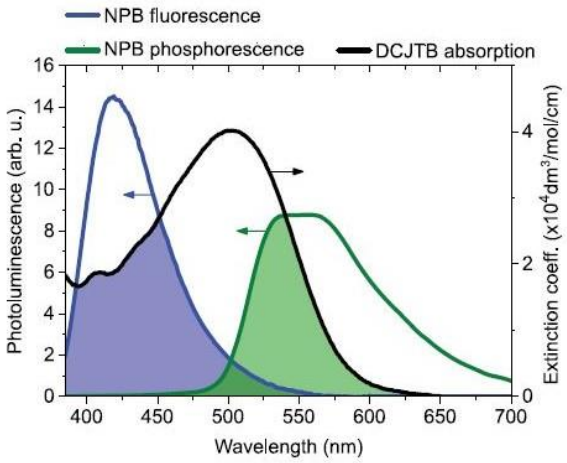

Figure 5.2. Spectral overlap of absorption of DCJTB with fluorescence and phosphorescence of NPB.

As can be seen in Figure 5.3 when DCJTB concentration increases, emission comes purely from DCJTB. This emission persists even after switching off the photoexcitation, which is direct proof of efficient energy transfer from the triplet state of NPB. Implementing this method, CW emission can be obtained via qCW photoexcitation which is another way round that we discussed earlier. As the film is no longer excited continuously, film degradation can also be suppressed compared to CW photoexcitation.

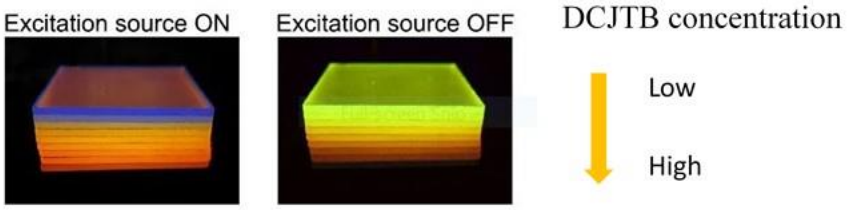

Figure 5.3. Claim of energy transfer from NPB S_1 to DCJTB S_1 and NPB T_1 to DCJTB S_1 when excitation on and off.

DFB structures should be designed according to the particular guest emitter's parameters as the emission comes from the emitter molecule in this host:guest system. Therefore, implementing a bioluminescence material as a host with a proper guest is a promising method to obtain CW laser emission with good stability.

Design of the DFB resonator structure plays a vital role in lasing. It helps to reduce the lasing threshold with high mode selection accompanied with enhanced spectral and temporal coherence. In this regard, I propose a hybrid DFB structure incorporating both 1-D and 2-D structures. The proposed DFB structure can be seen in Figure 5.4 below.

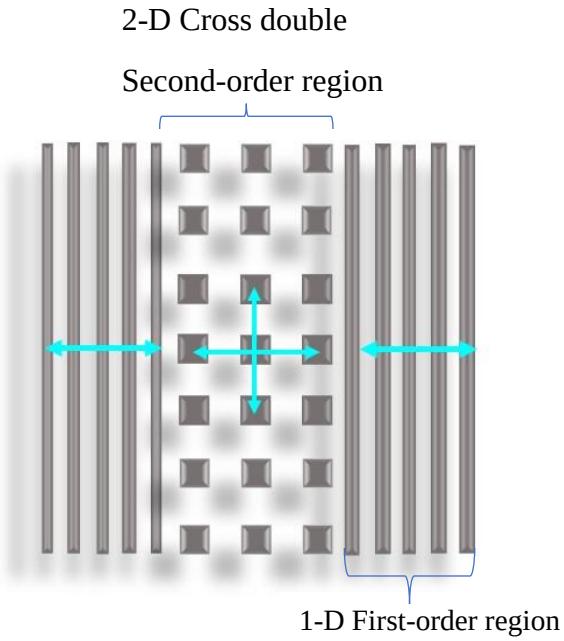

Figure 5.4. 1-D and 2-D hybrid DFB structure.

In this new design, energy loss occurs in 2-D cross double region which the periods are in second-order. This can be reduced by replacing it with the 1-D first-order region. Because energy loss in the first-order region is much less compared to the second-order region as the pitches are small. Then, in the 1-D first-order region, the feedback happens back and forth in horizontal direction and is coupled it to 2-D cross double region with reduced

energy loss as first-orders are intrinsically edge emitters. Then this light is further feedback in two orthogonal directions in the 2-D cross double region and light surface out couples with high input-output energy. Generally, first-order gratings have a higher Q-factor comparable to 2-D grating structures. The problem is, it is difficult to implement in devices as it is an edge emitter, as discussed in chapter 1. The Laser performance can be improved with this new design rather than using a pure 2-D cross double DFB structure.

At the current stage, reported OSLD[3] has shown stability issues that have to be addressed via stable laser material and proper device architectures. This will open up routes to replace normal OLEDs with high spectral purity and defined energies offered via coherent light emission of OSLDs.

In this regard, I am planning to investigate stable BSFCz material on electrical lasing with a possible device architecture using a solution-processable technique. First, solution-processable hole transporting materials and electron-transporting materials will be investigated for efficient OLEDs. As film quality is a crucial factor in solution-processable OSLDs, films will be optimized by using different solutions, different thicknesses, and spin-coating conditions to obtain high external quantum efficiencies (EQE) and low roll-off devices. Moreover, as the stability of BSFCz is higher compared to other reported materials, 2D resonators will be incorporated in the OSLDs for possible enhanced electrical laser performance. In regard to resonators, one-dimensional and two-dimensional (1D-2D) hybrid resonator structures will be studied to reduce the loss that occurs via second-order pitches to enhance the laser performance.

In addition, I also plan to use NaNaP-A:BDAVBi system in an OSLD inscribing a 1D-2D hybrid laser resonator. This system is promising as it can harvest 75% of triplet excitons generated in electrical excitations via TTA mechanism, which is generally wasted in fluorescent OLEDs. As the system works under the qCW regime, STA will also be suppressed, reducing EQE roll-off in OLEDs. Therefore, I think this NaNaP-A:BDAVBi system is a promising candidate for future OSLD.

References

[1] A. Kirch, M. Gmelch, S. Reineke, *J. Phys. Chem. Lett*., **2019**, *10*, 310.

[2] M. Inoue, T. Matsushima, C. Adachi, *Appl. Phys. Lett.,* **2016**, *108*, 133302.

[3] A. S. D. Sandanayaka, T. Matsushima, F. Bencheikh, S. Terakawa, W. J. Potscavage, C. Qin, T. Fujihara, K. Goushi, J. -C. Ribierre, C. Adachi, *Appl. Phys. Express*, **2019**, *12*, 061010.

List of publications and conferences

Original papers

[1] V. T. N. Mai, A. Shukla, **A. M. C. Senevirathne**, I. Allison, H. Lim, R. J. Lepage, S. K. M. McGregor, M. Wood, T. Matsushima, E. G. Moore, E. H. Krenske, A. S. D. Sandanayaka, C. Adachi, E. B. Namdas, S. C. Lo, *Adv. Opt. Mater*. **2020**, 8, 2001234. *(Equally contributed with V. T. N. Mai and A. Shukla).*

[2] A. Shukla, V. T. N. Mai, **A. M. C. Senevirathne**, I. Allison, S. K. M. McGregor, R. J. Lepage, M. Wood, T. Matsushima, E. G. Moore, E. H. Krenske, A. S. D. Sandanayaka, C. Adachi, E. B. Namdas, S-C Lo, *Adv. Opt. Mater*. **2020**, 8, 2000784. *(Equally contributed with A. Shukla and V. T. N. Mai).*

[3] **C. A. M. Senevirathne**, A. S. D. Sandanayaka, B. S. B. Karunathilaka, T. Fujihara, F. Bencheikh, C. Qin, K. Goushi, T. Matsushima, C. Adachi, *ACS Photonics***, 2021**, 8, 1324.

[4] **C. A. M. Senevirathne**, S. Yoshida, M. Yahiro, M Auffray, B. S. B. Karunathilaka, F. Bencheikh, K. Goushi, A. S. D. Sandanayaka,T. Matsushima, C. Adachi, Recycling of Triplets into Singlets for High Performance Organic Lasers. *(C. A. M. Senevirathne and S. Yoshida equally contributed) (submitted)*

Joint papers

[4] B. S. B. Karunathilaka, U. Balijapalli, **A. M. C. Senevirathne**, S. Yoshida, Y. Esaki, K. Goushi, T. Matsushima, A. S. D. Sandanayaka, C. Adachi, *Adv. Funct. Mater*. **2020**, 30, 2001078.

[5] B. S. B. Karunathilaka, U. Balijapalli, **C. A. M. Senevirathne**, S. Yoshida, Y. Esaki, K. Goushi, T. Matsushima, A. S. D. Sandanayaka, C. Adachi, *Nature Comm.* **2020**, 11, 4926

Conference presentations/posters

[1] **C. A. M. Senevirathne**, V. T. N. Mai, A. Shukla, I. Allison, H. Lim, R. Lepage, S. K. McGregor, M. Wood, E. G. Moore, E. H. Krenske, E. B. Namdas, S. -C. Lo, T. Matsushima, A. S. D. Sandanayaka, and C. Adachi, *Japan Society of Applied Physics (JSAP Autumn meeting-2019)*, Sapparo, Japan (September 18TH, 2019). (Oral presentation).

[2] **C. A. M. Senevirathne,** A. S. D. Sandanayaka, B. S. B. Karunathilaka, C. Qin, K. Goushi, T. Matsushima, C. Adachi, *Japan Society of Applied Physics (JSAP Autumn meeting-2020)*, online, Japan (September 8TH, 2020). (Oral presentation).

[3] **C. A. M. Senevirathne,** S. Yoshida, M. Auffray, B. S. B. Karunathilaka, K. Goushi, A. S. D. Sandanayaka, T. Matsushima, C. Adachi, *Japan Society of Applied Physics (JSAP Spring meeting-2021)*, online, Japan (March 16TH, 2021). (Oral presentation).

[4] **A.M. C. Senevirathne**, V. T. N. Mai, A. Shukla, B. S. B. Karunathilaka, T. Matsushima, A. S. D. Sandanayaka, S.-C. Lo, E. B. Namdas, C. Adachi, *Society of Photo-Optical Instrumentation Engineers (SPIE). The international society for optics and photonics-2020*, online, USA (August 24TH, 2020). (Poster presentation).

[5] **C. A. M. Senevirathne**, V. T. N. Mai, A. Shukla, S. -C. Lo, E. B. Namdas, T. Matsushima, A. S. D. Sandanayaka, Chihaya Adachi, *International conference on solid-state device and materials (SSDM)-2020*, online, Japan (September 27TH, 2020). (Oral presentation).

[6] **C. A. M. Senevirathne**, A. S. D. Sandanayaka, B. S. B. Karunathilaka, C. Qin, K. Goushi, T. Matsushima, C. Adachi, *A-COE 2020*, online, South Korea (November 8TH, 2020). (Poster presentation)

List of abbreviation

Materials

ADN	9,10-di(naphtha-2-yl)anthracene
Alq_3	Tris(8-hydroxyquinoline) Al
BDAVBi	4,4'-bis[4-(diphenylamino)styryl]biphenyl
BN-PFO	Poly 9,9-dioctylfluorene derivative containing 12% of statistical intrachain 6,6-2,2-octyloxy-1,1-binaphthalene binaphthyl
BP	Benzophenone
BSBCz	4-4′-bis[(*N*-carbazole)styryl]biphenyl
BSFCz	Bis(*N*- carbazolylstyryl)-9,9-dihexylfluorene
CBP	4,4′-bis(*N*-carbazolyl)-1,1′-biphenyl
DCJTB	4-(dicyanomethylene)-2-tert-butyl-6-(1,1,7,7-tetramethyljulolidyl-9-enyl)
DCM	Dichloromethane
DCM2	4-(dicyanomethylene)-2-methyl-6-julolidyl-9-enyl-4H-pyran
DCNP	2,6-dicyano-1,1-diphenyl-$\lambda^5\sigma^4$-phosphinine
DMF	*N, N*-dimethylformamide
DPAVB	1,4-bis(2-(4-(N,N-di(p-tolyl)amino)phenyl)vinylbenzene
HMDS	Hexamethyldisilazane
ITO	Indium tin oxide
LiF	Lithium Fluoride
NaNaP-A	9-(1-naphthalenyl)-10-(4-(2-naphthalenyl)phenyl)anthracene
Nd:YAG	Neodymium yttrium aluminum garnet
NPB	*N*,*N*′-di(naphtha-1-yl)-*N*,*N*′-diphenylbenzidine
PFO	Poly 9,9-dioctylfluorene
PMMA	Polymethylmethacrylate
TCTA	4,4',4"-Tris(carbazol-9-yl)-triphenylamine
THF	Tetrahydrofuran
TiS	Titanium sapphire
TPBi	2,2',2"-(1,3,5-benzinetriyl)-tris(1-phenyl-1- *H* -benzimidazole)

α-NPD	2,2'-dimethyl- *N,* N'-di-[(1-naphthyl) -*N,* N'-diphenyl]-1,1'-biphenyl-4,4'-diamine
***β*-DBDCS**	(2Z,2’Z)-3,3’-(1,4-phenylene)bis(2-(4-butoxyphenyl)acrylonitrile 4H-pyran

Keywords

AOM	Acousto optical modulator
ASE	Amplified spontaneous emission
CCD	Charge coupled device
CW	Continuous-wave
DBR	Distributed Bragg reflector
DFB	Distributed feedback
DSC	Differential scanning calorimetry
EQE	External quantum efficiency
FEM	Finite element method
FRET	Förster resonance energy transfer
FWHM	Fullwidth at half maximum
HOMO	Highest occupied molecular orbital
ISC	Intersystem crossing
LASER	Light amplification of stimulated emission of radiation
LiDAR	Light detection and ranging
LUMO	Lowest unoccupied molecular orbital
OLED	Organic light emitting diode
OSLD	Organic semiconductor laser diode
P	Polaron
PL	Photoluminescence
PLQY	Photoluminescence quantum yield
PMT	Photomultiplier tube

qCW	Quasi continuous-wave
SEM	Scanning electron microscopy
SPA	Singlet-polaron annihilation
SSA	Singlet-singlet annihilation
STA	Singlet-triplet annihilation
STED	Stimulated emission depletion
TA	Triplet absorption
TADF	Thermally activated delayed fluorescence
TAS	Transient absorption spectroscopy
TCSPC	Time-correlated single-photon counting
TE	Transient electric
TGA	Thermo gravimetric analysis
TM	Transient magnetic
TPA	Triplet-polaron annihilation
TTA	Triplet-triplet annihilation

Acknowledgment

The studies in this thesis were carried out at Adachi laboratory, Department of Applied Chemistry, Graduate School of Engineering, Kyushu University from 2018 to 2021.

First, I deeply grateful to Prof. Chihaya Adachi for supervising this thesis. Also, I sincerely thank him for providing me a friendly experimental environment and for supporting me in my research in every possible way. I also grateful for his helpful discussions, kind guidance, and encouragement throughout my studies in Japan.

I also very much thankful to Prof. Hiroyuki Furuta and Prof. Yuji Oki for taking the time to evaluate this thesis and for their valuable suggestions and comments.

Moreover, my sincere thank goes to Prof. Atula Sandanayaka for introducing me for lasers and training me with many instruments, for teaching me subject matter which was needed for my research. Also, I am very much thankful for his continuous encouragement, support, and guidance given for my studies. I would also thank Prof. Toshinori Matushima for his great support and guidance, helpful discussions, insightful comments which led me to think deeply about the subject matter, correcting my manuscripts many times and for the encouragement given every step of my research carrier.

Also, I am very much thankful to Prof. Ebinazar Namdas and Prof. Shi Shun Lo of the University of Queensland, Australia and their research teams for providing me excellent molecules and for their helpful discussions and kind support.

I must also thank Prof. Hajime Nakanotani for preparing me for department examinations, insightful comments, and his kind support in my research. Also, I am thankful to Prof. Kenichi Goushi for his helpful discussions and his kind support in my experiments. Moreover, I am thankful to Prof. Masashi Mamada and Prof. Youichi Tsuchiya for their kind support and helpful discussions which helped me to understand the subject matter.

Also, I am thankful to Ms. Shinobu Terakawa for teaching me of preparing DFBs and many more things in a clean room and for being such a nice friend. I am also very much thankful to Dr. Takashi Fujihara for teaching me to align the CW laser setup many times, even in his busy schedule. Moreover, I am thankful to Dr. Hao Ye, Dr. Morgan Auffray, Dr. Buddhika Karunathilaka, Dr. Fatima Bencheikh, Dr. Ryotaro Komatsu, Dr. Yu Esaki, Dr. Masaki Tanaka, Mr. R. Fukunaga, Dr. Ryo Nagata, Mr. Seiya Yoshida, Mr. Shinichi Tan, Mr. Nguyen Ba Thanh, Dr. Ganbaatar, Dr. Thai Chen, Mr. Takeishi, Dr. Yiting Lee, Dr. Chin-Yiu Chan, Prof. Anthony D Aleo, Dr. Virginie Placid, Prof. Fabrice Mathevet, Mr. Nishimura, Mr. Watanabe, Ms. Sahar Alsvand, Mr. Xun Tang, Mr. Tomohiro Ishii, Mr. Jaehyun Bae, Dr. Kim Jonguk, Ms. Abe Ayano, and all OPERA members for their all the kind support in experiments and day to day life in the laboratory.

I would also be thankful to Ms. Sachiko Higashikawa, Ms. Hiroko Kuratomi, Ms. Yuko Kawahara, Ms. Rei Sasagawa, Ms. Hino Nakanotani, Ms. Haruna Kato for all their friendliness and kind support during my stay in OPERA.

At last, but not least, I am very grateful to my parents, my sister, and my friends for being there for me all the time and for their constant kind support and encouragement.

A. M. Chathuranganie Senevirathne

2021.06.22